Theoretical and Experimental Study on High Spectral Efficiency Coherent Optical OFDM Systems

by

Xi Chen

Submitted in total fulfilment of

the requirements for the degree of

Doctor of Philosophy

Department of Electrical & Electronic Engineering

The University of Melbourne

Australia

August 2012

Abstract

Theoretical and Experimental Study on High Spectral Efficiency Coherent Optical OFDM Systems

By **Xi Chen**

Coherent optical OFDM (CO-OFDM) has attracted significant attention from the optical communications community as a potential candidate for long-haul 100-Gb/s to 1-Tb/s Ethernet transport, for its high spectral efficiency and robustness against chromatic dispersion. In this thesis, we conduct theoretical and experimental study on high spectral efficiency CO-OFDM systems.

We first present theoretical analysis of nonlinearity impact on high spectral efficiency CO-OFDM systems. In particular, we derive closed-form analytical expressions for nonlinear system performance for densely spaced CO-OFDM systems via single mode fibre (SMF) transmission. The closed-form solutions include the results for the achievable Q factor, optimum launch power density, nonlinear threshold of launch power density, and information spectral efficiency limit. The closed-form solution is further substantiated by numerical simulations using distributed nonlinear Schrödinger equation. We also show some preliminary study on information capacity of densely spaced CO-OFDM transmission via two-mode fibre (TMF).

As shown in our theoretical study, the capacity of optical fibre is ultimately limited by fibre nonlinearity. Subsequently, fibre nonlinearity mitigation has become a critical research topic in optical communications community. In this thesis, we demonstrate two approaches for fibre nonlinearity mitigation in high spectral efficiency OFDM systems: DFT-spread (DFT-S) OFDM and mid-link digital phase conjugation. For DFT-S OFDM, we show experimental verification of nonlinear

performance advantage of DFT-S OFDM systems over conventional OFDM systems. Densely spaced 8×55.1-Gb/s DFT-S OFDM channels are successfully received after 1120-km transmission with a spectral efficiency of 3.5 b/s/Hz. It is shown that DFT-S OFDM has advantage of about 1 dB in Q factor and 1 dB in launch power over conventional OFDM. For mid-link digital phase conjugation, we demonstrate single-channel 40-Gb/s polarization-division multiplexed (PDM) CO-OFDM-16QAM transmission over 10,400-km ultra-larger area fibre (ULAF) by mid-link digital phase conjugation, showing a power-tolerance improvement of 4-dB and a reach extension of over 50% for this high-level modulation format.

We then present several novel digital signal processing approaches to monitor, receive, and route high spectral efficiency OFDM signals: we develop a method of laser linewidth characterization and monitoring which is robust against additive white noise for the spectrally efficient CO-OFDM systems; we also demonstrate three channel equalization methods for TMF based CO-OFDM systems. The results show that our 4x6 MIMO receiver can improve the receiver sensitivity by 1.8 dB, 2.9 dB, and 4.9 dB for zero forcing (ZF), minimum mean square error (MMSE), and succussive interference cancellation (SIC) respectively; At last, we design a mode-compatible optical add/drop multiplexer (OADM) for mode-division multiplexed CO-OFDM systems. We demonstrate add, drop and through functionalities for 3x318 Gb/s OFDM signals, and find that the OSNR penalties for add, drop and through ports are 2.6, 2.4, 0.7 dB, respectively.

This is to certify that

(i) the thesis comprises only my original work,

(ii) due acknowledgement has been made in the text to all other material used,

(iii) the thesis is less than 100,000 words in length, exclusive of table, maps, bibliographies, appendices and footnotes.

Signature

Date

Declaration

I hereby declare that this thesis comprises only my original work. No material in this thesis has been previously published and written by another person, except where due reference is made in the text of the thesis. I further declare that this thesis contains no material which has been submitted for a degree or diploma or other qualifications at any other university. Finally, I declare that the thesis is less than 100,000 words in length, exclusive of tables, figures, bibliographies, appendices and footnotes.

Acknowledgments

This thesis is conducted under the help and support from many people to whom I would like to express my thanks.

First, I would like to express my deepest appreciation of the consistent help and support from my supervisor Prof. William Shieh. I would like to thank the high-quality advices and guidance that Prof. Shieh has offered throughout my PhD candidature. I would like to thank my PhD committee members, A/Prof. Christina Min Ee Lim and A/Prof. Marcus Nathan Brazil for their guidance. I also would like to express my greatest gratitude to Dr. Xiang Liu and Dr. Chandrasekhar Sethumadhavan for their academic advices and generous help during my internship in Bell Labs, Alcatel-Lucent.

I would like to thank the University of Melbourne for offering my PhD scholarships. Many thanks to all the colleagues around me in the Department of Electrical and Electronics Engineering for providing a friendly and entertaining work environment.

A special thanks of mine goes to all the team members from the research group of Prof. Shieh. We had insightful discussions and exchanged interesting thoughts. I appreciate the cooperation and collaboration with Dr. An Li. I am also grateful to Dr. Abdullah Al Amin for his invaluable guidance.

On a personal level, I wish to thank my parents for their undivided support. It is their love and encouragement that fulfil my personality and lead me to the accomplishment of my PhD study.

Contents

List of Figures

Chapter 1 Introduction

1.1 Overview

Optical fibres became a transmission media for high-speed communication since early1980s. After the introduction of single mode fibre (SMF) in the late 1980s and the invention of C-band optical amplifiers in the early1990s, fibre-optic communication gradually replaced conventional copper wire communications and has played a major role in telecommunication. Moreover, the advent of wavelength-division multiplexing (WDM) enables capacity multiplying by utilizing parallel wavelength channels, opening the door to the era of high-capacity optical communication. Nowadays, 40-Gbit/s WDM networks are being launched by most of the major vendors. Meanwhile, systems operating at 100-Gbit/s or beyond have been experimentally demonstrated in research labs and is actively developed in industry.

The WDM channel wavelength allocation has been regulated according to International Telecommunication Union (ITU) channel grid [1, 2] where the channel spacing is specified as 50 GHz. As a result, to increase channel capacity and spectral efficiency under the given channel spacing, advanced modulation formats such as coherent optical single carrier and multicarrier modulation have been explored in modern fibre-optic communication. Among various multi-carrier techniques, coherent optical OFDM (CO-OFDM) has attracted significant attention from the optical communications community as a potential candidate for long-haul 100-Gb/s to 1-Tb/s Ethernet transport, for its high spectral efficiency and robustness against chromatic dispersion.

With the fast progress in academic research, the Shannon information capacity limit for SMF transmission has been rapidly approached within practical engineering margin. It is then impossible to enjoy the same dramatic capacity growth in the future as in the past two decades, if we continue to stay with the SMF platform. Space-division multiplexing (SDM) has been recently explored to overcome the capacity barrier using few-mode fibre (FMF) or multi-core fibre (MCF). This leads to an intense ongoing

research works that focusing on developing optical communication systems using SDM.

1.2 Motivation

CO-OFDM is advantages in spectral efficiency and its resilience to channel dispersion. However, CO-OFDM is known to be susceptible to fibre nonlinearity due to its high peak-to-average power ratio (PAPR). Thus, it is imperative to study information capacity limits for CO-OFDM transmission in presence of fibre nonlinearity. Furthermore, it is of public interest to develop algorithms or methods to (i) mitigate nonlinear noise and (ii) implement high spectral efficiency CO-OFDM transmission systems. Therefore, this thesis focuses on topics in relation to high spectral efficiency CO-OFDM transmission as follows:

- The ultimate information capacity limit for densely spaced CO-OFDM systems in presence of fibre nonlinearity
- Fibre nonlinearity mitigation for CO-OFDM transmission
- Enhancing information capacity of CO-OFDM systems by using novel few-mode fibres

1.3 Organization of the Thesis

The organization of this thesis is laid out as follows:

Chapter 1 Introduction. This chapter presents an overview and the introduction of the thesis.

Chapter 2 Information capacity limit of CO-OFDM systems due to fibre nonlinearity. This chapter shows a theoretical study of information capacity limit for densely spaced CO-OFDM systems. The theoretical study includes derivation of closed-form expressions for nonlinear CO-OFDM transmission via both single mode fibre (SMF) and few-mode fibre (FMF). The theory is further verified by numerical

simulation or some preliminary experiments.

Chapter 3 Fibre nonlinearity mitigation for CO-OFDM. In this chapter, two approaches of nonlinearity mitigation will be discussed including (i) DFT-spread OFDM, and (ii) mid-link digital phase conjugation. Principle of each mitigation algorithm is presented, and the algorithm is substantiated by experiments.

Chapter 4 Phase Noise Monitoring for High Spectral Efficiency CO-OFDM Transmission. In this chapter, a method for laser linewidth characterization and monitoring is proposed. The proposed method is robust against additive white noise and is applicable to both single-carrier and multi-carrier systems. Using the proposed method, laser linewidth can be extracted via embedded signal processing.

Chapter 5 Enabling Spectrum-efficient Transmission by Using Two-mode Fibre (TMF) Fibres. This chapter develops some designs for high spectral efficiency optical fibre transport using TMF. In particular, we propose channel equalisation algorithm for mode-division multiplexed (MDM) CO-OFDM superchannel, and we design and demonstrate a mode-compatible optical add/drop multiplexer (OADM) for future high spectral efficiency MDM network.

Chapter 6 Conclusions. This chapter summarizes the outcomes of the thesis.

1.4 Contribution of the Thesis

The contributions of this thesis are listed as follows:

Chapter 2

- We derive closed-form analytical expressions for nonlinear system performance for densely spaced CO-OFDM systems via SMF transmission. The closed-form solutions include the achievable Q factor, optimum launch power density, nonlinear threshold of launch power density, and information spectral efficiency limit. These analytical results identify the system performance dependence on system parameters including fibre dispersion, number of transmission spans,

dispersion compensation ratio, and overall bandwidth. The closed-form solutions are further substantiated by numerical simulations using distributed nonlinear Schrödinger equations.

Chapter 3

- We show the first experimental verification of nonlinear performance advantage of DFT-S OFDM systems over conventional OFDM systems. Densely spaced 8×55.1-Gb/s DFT-S OFDM channels are successfully received after 1120-km transmission with a spectral efficiency of 3.5 b/s/Hz. We adopt a novel approach of consecutive transmission of DFT-S OFDM and conventional OFDM enabling stable and repeatable measurements. It is shown that DFT-S OFDM has advantage of about 1 dB in Q factor and 1 dB in launch power over conventional OFDM. Additionally, unique word (UW) aided phase estimation algorithm is proposed and demonstrated enabling extremely long OFDM symbol transmission.
- We demonstrate single-channel 40-Gb/s polarization-division multiplexed (PDM) CO-OFDM-16QAM transmission over 10,400-km ultra-large area fibre (ULAF) by mid-link digital phase conjugation. The results show a power-tolerance improvement of 4 dB and a reach extension of over 50% for this high-level modulation format. Together with its high DSP efficiency, mid-link digital phase conjugation could be a promising candidate for future ultra-long-haul point-to-point transmission systems.

Chapter 4

- We derive a closed-form expression for differential phase-error variance. The phase noise is averaged over a finite time window, cancelling the effects of additive white noise. A method for laser linewidth characterization and monitoring is proposed in presence of additive white noise. This method is applicable to both single-carrier and multi-carrier systems. Using the proposed method, laser linewidth can be extracted via embedded signal processing. Therefore the monitoring can be done in-service without interruption of data transmission. The algorithm is further

substantiated by experiments in a 107-Gb/s coherent optical OFDM system with 960-km transmission over standard single mode fibre (SSMF) fibre. A novel method of digitally adjusting laser linewidth is proposed and demonstrated which may be useful to systematically study the laser phase noise impact.

Chapter 5

- We demonstrate three channel equalization methods for FMF-based CO-OFDM systems. The results show that the 4x6 MIMO receiver can improve the receiver sensitivity by 1.8 dB, 2.9 dB, and 4.9 dB for zero-forcing (ZF), minimum mean square error (MMSE), and successive interference cancellation (SIC) respectively.
- We design an optical add drop multiplexer (OADM) that supports two orthogonal LP_{11} modes of a FMF. We demonstrate add, drop and through functionalities for 3x318 Gb/s OFDM signals, and found that the OSNR penalties for add, drop and through ports are 2.6, 2.4, 0.7 dB, respectively. Additionally, a heterodyne coherent detection which supports multi-band signal with high spectral efficiency is proposed and investigated.

1.5 Publications

[1] X. Chen, and W. Shieh, "Closed-form expressions for nonlinear transmission performance of densely spaced coherent optical OFDM systems," Opt. Express 18, pp.19039-19054, 2010.

[2] X. Chen, A. Al Amin, and W. Shieh, “Characterization and Monitoring of Laser Linewidths in Coherent Systems” J. Lightwave Technol. 17, pp.2533-2537, 2011.

[3] X. Chen, A. Li, G. Gao, and W. Shieh, "Experimental demonstration of improved fiber nonlinearity tolerance for unique-word DFT-spread OFDM systems," Opt. Express 19, pp.26198-26207, 2011.

[4] X. Chen, A. Li, G. Gao, A. A. Amin, and W. Shieh , “Characterization of Fiber Nonlinearity and Analysis of its Impact on Link Capacity Limit of Coherent

Optical OFDM Systems for Two-mode Fibers," IEEE Photon. Journal 4, pp.455-460, 2012.

[5] X. Chen, A. Li, G. Gao, A. Al Amin, and W. Shieh, "Reception of Mode-division Multiplexed Superchannel via Few-mode Compatible Optical Add/Drop Multiplexer", Opt. Express 20, 14302-14307, 2012.

[6] X. Chen, J. Ye, Y. Xiao, A. Li, J. He, Q. Hu, and W. Shieh, "Equalization of Two-mode Fiber Based MIMO Signals with Larger Receiver Sets," accepted by Opt. Express, scheduled to be published in Nov. 2012.

[7] X. Chen, A. Li, J. Ye, A. Al Amin, and W. Shieh, "Demonstration of few-mode compatible optical add/drop multiplexer for mode-division multiplexed superchannel," J. Lightwave Technol., accepted, scheduled to be published in Jan. 2013.

[8] X. Chen, A. Al Amin, and W. Shieh, "Characterization and Monitoring of Laser Linewidths in Coherent Optical OFDM Systems," Optical Fiber Communication Conference (OFC), 2011, Los Angeles, USA, pp.OWN4.

[9] (Best student paper) X. Chen, A. Al Amin, and W. Shieh, "Closed-form Expression for Differential Phase Error Variance in Coherent Optical Systems, Asia Communications and Photonics Conference (ACP), 2011, Shanghai, China, pp.8309-09.

[10] (Best student paper) X. Chen, A. Li, J. Ye, A. Al Amin, and W. Shieh, "Joint-mode RF-pilot Aided Phase Estimation for Mode-division Multiplexed CO-OFDM Superchannel," Asia Communications and Photonics Conference (ACP), 2012, Guangzhou, China, pp. ATh2C.3.

[11] X. Chen, X. Liu, S. Chandrasekhar, B. Zhu, and R. W. Tkach, "Experimental Demonstration of Fiber Nonlinearity Mitigation Using Digital Phase Conjugation", Optical Fiber Communication Conference (OFC), 2012, Los Angeles, USA, pp.OTh3C.1.

[12] X. Chen, A. Li, J. Ye, A. Al Amin and W. Shieh, “Reception of Dual-LP11-Mode CO-OFDM Signals through Few-mode Compatible Optical Add/Drop Multiplexer”, Optical Fiber Communication Conference (OFC), 2012, Los Angeles, USA , pp.PDP5B.4.

[13] (Invited) X. Chen, A. Li, G. Gao, A. Al Amin, and W. Shieh, “Unique-word DFT-Spread OFDM for Ultra-high Speed Optical Transmission,” OptoElectronics and Communications Conference (OECC), 2012, Busan, Korea, pp. 4B2-3.

[14] (Invited) X. Chen, A. Li, J. Ye, A. Al Amin and W. Shieh, “Few-mode compatible Optical Add/Drop Multiplexer (OADM)”, Asia Communications and Photonics Conference (ACP), 2012, Guangzhou, China.

[15] X. Chen, A. Li, G. Gao, A. Al Amin, and W. Shieh, “Study of Fiber Nonlinearity Impact on the System Capacity of Two-Mode Fibers,” Optical Fiber Communication Conference (OFC), 2012, Los Angeles, USA, pp.JW2A.40.

[16] X. Chen, J. Ye, Y. Xiao, A. Li, J. He, Q. Hu, and W. Shieh, “Equalization of Two-mode Fiber Based MIMO Signals with Larger Receiver Sets” European Conference on Optical Communication (ECOC), 2012, Amsterdam, The Netherlands, pp. Th.2.D.2.

[17] (Invited) W. Shieh and X. Chen, “Information Spectral Efficiency and Launch Power Density Limits Due to Fiber Nonlinearity for Coherent Optical OFDM Systems,” IEEE Photon. Journal 3, pp.158 – 173, 2011.

[18] A. Li, A. Al Amin, X. Chen, and W. Shieh, “Reception of Mode and Polarization Multiplexed 107-Gb/s CO-OFDM Signal over a Two-Mode Fiber,” Optical Fiber Communication Conference (OFC), 2011, Los Angeles, USA , pp.PDPB8.

[19] A. Li, A. Al Amin, X. Chen, and W. Shieh, "Transmission of 107-Gb/s mode and polarization multiplexed CO-OFDM signal over a two-mode fiber," Opt.

Express 19, pp.8808-8814, 2011.

[20] A. Al Amin, A. Li, S. Chen, X. Chen, G. Gao, and W. Shieh, "Dual-LP11 mode 4x4 MIMO-OFDM transmission over a two-mode fiber," Opt. Express 19, pp.16672-16679, 2011.

[21] (Invited) A. Al Amin, A. Li, X. Chen, and W. Shieh, “Spatial Mode Division Multiplexing for Overcoming Capacity Barrier of Optical Fibers,” OptoElectronics and Communications Conference (OECC), 2011, Kaohsiung, Taiwan, pp. 7B1-2

[22] Q. Yang, A. Al Amin, X. Chen, Y. Ma, S. Chen, and W. Shieh, "428-Gb/s single-channel coherent optical OFDM transmission over960-km SSMF with constellation expansion and LDPC coding," Opt. Express 18, pp.16883-16889, 2010.

[23] (Invited) S. Chen, Y. Ma, Q. Yang, X. Chen, A. Al Amin, and W. Shieh, “Ultra-broadband OFDM signal generation for 1-Tb/s super-channel,” Optics Communications 28, Special Issue, pp.3718-3722, 2011.

[24] X. Liu, S. Chandrasekhar, X. Chen, P. J. Winzer, Y. Pan, T. F. Taunay, B. Zhu, M. Fishteyn, M. F. Yan, J. M. Fini, E.M. Monberg, and F.V. Dimarcello, “1.12-Tb/s 32-QAM-OFDM superchannel with 8.6-b/s/Hz intrachannel spectral efficiency and space-division multiplexed transmission with 60-b/s/Hz aggregate spectral efficiency”, European Conference On Optical Communication (ECOC), 2011, Geneva, Switzerland, pp.Th.13.B.1.

[25] X. Liu, S. Chandrasekhar, X. Chen, P. J. Winzer, Y. Pan, T. F. Taunay, B. Zhu, M. Fishteyn, M. F. Yan, J. M. Fini, E.M. Monberg, and F.V. Dimarcello, “1.12-Tb/s 32-QAM-OFDM superchannel with 8.6-b/s/Hz intrachannel spectral efficiency and space-division multiplexed transmission with 60-b/s/Hz aggregate spectral efficiency”, Opt. Express 19, pp.B958-B964, 2011.

[26] G. Gao, X. Chen and W. Shieh, “Limitation of Fiber Nonlinearity Compensation Using Digital Back Propagation in the Presence of PMD,”

Optical Fiber Communication Conference (OFC), 2012, Los Angeles, USA, pp.OM3A.5.

[27] (Corning Outstanding Student Paper Competition Honorable Mention Winner) A. Li, X. Chen, G. Gao, A. Al Amin, W. Shieh, and B. S. Krongold, “Transmission of 1.63-Tb/s PDM-16QAM Unique-word DFT-Spread OFDM Signal over 1,010-km SSMF,” Optical Fiber Communication Conference (OFC), 2012, Los Angeles, USA , pp.OW4C.1.

[28] (Invited) W. Shieh, X. Chen, A. Li, G. Gao, and A. Al Amin, “What is the Optimal Symbol Rate for Long-haul Transmission?” Asia Communications and Photonics Conference (ACP), 2011, Shanghai, China, pp.83090L.

[29] G. Gao, X. Chen, and W. Shieh, “Application of Closed-form Expressions for Nonlinear Transmission Performance of Coherent Optical OFDM Systems,” Asia Communications and Photonics Conference (ACP), 2011, Shanghai, China, pp.8309-51.

[30] A. Li, X. Chen. G. Gao, and W. Shieh, “Transmission of 1-Tb/s Unique-word DFT-Spread OFDM Superchannel over 8,000-km SSMF,” Asia Communications and Photonics Conference (ACP), 2011, Shanghai, China, pp.8309-120.

[31] A. Li, A. Al Amin, X. Chen, S. Chen, G. Gao, and W. Shieh, “Reception of Dual-Spatial-Mode CO-OFDM Signal over a Two-Mode Fiber,” J. Lightwave Technol. 4, pp.634-640, 2012.

[32] A. Al Amin, A. Li, X. Chen, and W. Shieh, “LP01/LP11 dual-mode and dual-polarisation CO-OFDM transmission on two-mode fibre,” Electron. Lett. 47, pp.606–607, 2011.

[33] A. Al Amin, G. Gao, X. Chen, A. Li, and W. Shieh, “Performance of Adaptive Optical Transmission by Orthogonal Frequency-Shift Keying” Photon. Technol. Lett. 24, pp.1079-1081, 2012.

[34] (Invited) A. Al Amin, A. Li, X. Chen and W. Shieh, “Mode Division Multiplexing MIMO-OFDM Optical Transmission”, OptoElectronics and Communications Conference (OECC), 2012, Busan, Korea, pp. 5E2-3.

[35] (Invited) A. Li, X. Chen, A. Al Amin, and W. Shieh, “Mode Converters and Couplers for Few-Mode Transmission”, IEEE Summer Topicals, 2012, Seattle, USA.

[36] G. Gao, X. Chen, and W. Shieh, “Influence of PMD on fiber nonlinearity compensation using digital back propagation”, Opt. Express 20, 14406-14418, 2012.

[37] A. Li, X. Chen, A. Al Amin, J. Ye and W. Shieh, “Space-Division Multiplexed High-Speed Superchannel Transmission over Few-Mode Fiber”, J. Lightwave Technol., DOI: 10.1109/JLT.2012.2206797 (2012).

[38] G. Gao, X. Chen, and W. Shieh, “Analytical Expressions for Nonlinear Transmission Performance of Coherent Optical OFDM Systems with Frequency Guard Band”, J. Lightwave Technol 30, pp. 2447-2454, 2012.

[39] A. Li, X. Chen, G. Gao and W. Shieh, "Transmission of 1-Tb/s Unique-Word DFT-Spread OFDM Superchannel over 8000-km EDFA-only SSMF link," J. Lightwave Technol. DOI: 10.1109/JLT.2012.2206369, (2012).

[40] A. Li, X. Chen, A. Al Amin, and W. Shieh, “Fused Fiber Mode Couplers for Few-Mode Transmission,” Photonics Technol. Lett. 24, pp. 1953-1956, 2012.

Chapter 2 Information Capacity Limit of CO-OFDM Systems due to Fibre Nonlinearity

During the past few years, high capacity and long haul CO-OFDM transmission has been demonstrated [3-6]. With the expansion of signal bandwidth and the adoption of higher-order constellation, fibre nonlinearity has become one of the important degradations of CO-OFDM transmission. It is therefore necessary to study the information capacity limit of CO-OFDM systems in presence of fibre nonlinearity. In this chapter, we present theoretical study of information capacity limit for densely spaced CO-OFDM systems. The theoretical study includes derivation of closed-form expressions for transmission via both single mode fibre (SMF) and few-mode fibre (FMF). The theory is further verified by numerical simulation or some preliminary experiments.

2.1 Information Capacity of CO-OFDM via SMF Transmission

As shown in [7], high spectral efficiency transmission can be readily achieved with the concept of CO-OFDM. In such systems, the CO-OFDM wavelength channels can be either continuously spaced without frequency guard band [8-10], or densely spaced with extremely small frequency guard band [11, 12]. These densely spaced systems present the ultimate limit of achieving high spectral efficiency by allowing very little or no frequency guard band. Most recently, nonlinear transmission performance of CO-OFDM systems has attracted much attention [7, 13-16]. In particular, analytical results are shown in [13] for single-channel transmission without consideration of chromatic dispersion; complete analytical expressions are presented in [14] involving summation of a large number of terms for practical OFDM systems; system performances via numerical simulation are reported in [7, 17]. It would be of great interests to derive concise closed-form solutions that capture the dependence of the nonlinear performance on some major system parameters such as chromatic dispersion and dispersion compensation ratio. Similar analytical work was pioneered in [18]

where nonlinear launch power and information capacity is derived in closed-form. However, there are two limitations for the report: (i) it only includes the cross phase modulation (XPM) as the dominant effect ignoring four-wave-mixing (FWM) and self-phase-modulation (SPM). This only applies to sparsely spaced WDM systems and would not apply to the densely CO-OFDM systems where XPM, FWM, and SPM are all important, and very often indistinguishable [7, 13-15]; (ii) it assumes that nonlinear phase noise is generated independently in different spans, ignoring an important phase array effect of the FWM products that accounts for the interference between multiple spans [14]. In this section, we derive closed-form analytical expressions for nonlinear system performance of densely spaced CO-OFDM systems via single mode fibre (SMF) transmission [19, 20]. The closed-form solution entails the results for achievable Q factor, optimum launch power density, nonlinear threshold of launch power density, and information spectral efficiency limit. These analytical results clearly identify the nonlinear performance dependence on system parameters including fibre dispersion, number of spans, dispersion compensation ratio, and overall bandwidth [19, 20]. The closed-form solutions are further substantiated by numerical simulations using distributed nonlinear Schrödinger equation [19, 20].

2.1.1 Theoretical Derivation and Analysis

The class of transmission systems, namely, densely spaced OFDM (DS-OFDM) systems that is treated in this chapter is depicted in Figure 2.1(a) where each wavelength channel is OFDM modulated with subcarrier frequency spacing of Δf and bandwidth of *W*, separated with neighbouring channel by a frequency guard band of ΔB. We define the term of 'densely spaced' as the condition of $\Delta B << W$. As such, the frequency guard band can be omitted in the remainder of the investigation. With such an assumption, we study the continuous 'single-band' like multi-carrier systems with Δf subcarrier spacing and total bandwidth of *B* as shown in Figure 2.1(b). In such DS-OFDM systems, all the nonlinear effects such as XPM, FWM, and SPM can be considered as FWM between all the subcarriers if we treat multiple densely spaced

wavelength channels as an effective big 'single-band' OFDM channel that encompasses all the subcarriers.

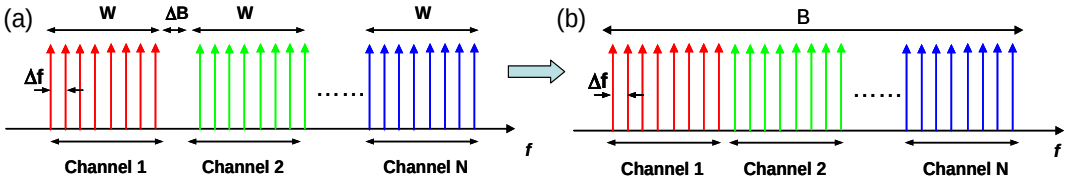

Figure 2.1. Conceptual diagram of densely spaced OFDM (DS-OFDM) systems: (a) with a frequency guard band ΔB that is much smaller than the wavelength channel bandwidth W, and (b) continuous without any frequency guard band.

FWM is the third-order nonlinearity effect and its impact on optical fibre communications has been extensively studied [17, 21]. Due to the FWM, the interaction of subcarriers at the frequencies of f_i, f_j, and f_k produces a mixing product at the frequency of $f_g = f_i + f_j - f_k$. The magnitude of the FWM product for N_s spans of the fibre link is given by [17, 21]

$$P_g' = \frac{D_x^{\ 2}}{9}\gamma^2 P_i P_j P_k e^{-\alpha L}\eta' \tag{2.1}$$

where D_x is the degeneration factor which equals 6 for non-degenerate FWM, and 3 for degenerate FWM. $P_{i,j,k}$ is the input power at the frequency of $f_{i,j,k}$, α and L are respectively the loss coefficient and length of the fibre per span, γ is the third-order nonlinearity coefficient of the fibre, η' is the FWM coefficient which has a strong dependence on the relative frequency spacing between the FWM components given by

$$\eta' = \eta_1'\eta_2' \tag{2.2}$$

$$\eta_1' = \left|\frac{1-e^{-\alpha L}e^{-j\Delta\beta_{ijk}L}}{j\Delta\beta_{ijk}+\alpha}\right|^2 \approx \frac{1}{\left(\Delta\beta_{ijk}\right)^2+\alpha^2} \tag{2.3}$$

$$\eta_2' = \frac{\sin^2\left\{N_s\Delta\tilde{\beta}_{ijk}/2\right\}}{\sin^2\Delta\tilde{\beta}_{ijk}/2}, \qquad \Delta\tilde{\beta}_{ijk} = \Delta\tilde{\beta}_{ijk}L + \Delta\beta_{ijk,1}L_1 \tag{2.4}$$

In (2.2) the overall FWM efficiency is decomposed into two separate contributions: (i) η_1', the FWM efficiency coefficient for single span (for simplicity, the contribution from dispersion compensation fibre is omitted), and (ii) η_2', the interference effect between N_s spans of FWM products, also known as phase array effect [14]. $\Delta\beta_{ijk} \equiv \beta_i + \beta_j - \beta_k - \beta_g$ is the phase mismatch in the transmission fibre. In (2.3), we assume that the span loss $e^{\alpha L}$ is much larger than 1, $e^{-\alpha L}e^{-j\Delta\beta_{ijk}L}$ is removed from the nominator. In (2.4), the subscript '1' stands for the parameters associated with the dispersion compensation fibre (DCF)). Assuming *m*-th subcarrier frequency has the form of $f_m = m \cdot \Delta f$, the phase mismatch terms $\Delta\beta_{ijk}$ and $\Delta\tilde{\beta}_{ijk}$ in (2.4) and (2.5) can be rewritten as

$$\begin{aligned}\Delta\beta_{ijk} &= \frac{2\pi\lambda^2}{c}(f_i - f_k)(f_j - f_k)D \\ &= -4\pi^2\beta_2(f_i - f_k)(f_j - f_k) \\ &= -4\pi^2\beta_2\Delta f^2(i-k)(j-k) \\ \beta_2 &= -\frac{\lambda^2}{2\pi c}D\end{aligned} \tag{2.5}$$

$$\begin{aligned}\Delta\tilde{\beta}_{ijk} &= \frac{2\pi\lambda^2}{c}(f_i - f_k)(f_j - f_k)D_r \\ &= -4\pi^2\beta_2(f_i - f_k)(f_j - f_k)L(1-\rho) \\ &= -4\pi^2\beta_2\Delta f^2 L(1-\rho)(i-k)(j-k) \\ D_r &= DL + D_1L_1 = DL(1-\rho) = DL\zeta\end{aligned} \tag{2.6}$$

where D (or D_1) is the chromatic dispersion of the transmission fibre (or DCF), ρ (or ζ) is the dispersion compensation (or residual dispersion) ratio, D_r is the residual chromatic dispersion per span accounting for both transmission fibre and DCF. At the end of each span, the FWM product P_g' along with the signal will be amplified by a gain of G equal to the loss of each span $e^{-\alpha L}$ and the FWM product becomes

$$P_g = \frac{D_x^{\,2}}{9}\gamma^2 P_i P_j P_k \eta' \tag{2.7}$$

We adopt the approach used in [22] where the nonlinear effect is considered as the multiplicative noise to the signal. In essence, we will consider *i*-th subcarrier as the reference frequency, and *j* and *k* frequencies as the interferers, namely, frequency *j* and frequency *k* generates a beating frequency component at $\left(f_j - f_k\right)$, which in turn modulates the subcarrier *i*, creating fourth components of f_g. It has been shown for large number of subcarriers, the non-degenerate FWM is the dominate effects [14], and D_x is set to 6 in (2.7). Consequently, the nonlinearity impinging on subcarrier *i*, P_{NL}^{i} is given as

$$P_{NL}^{i} = 2\gamma^2 P_i \sum_{k=-N/2}^{N/2} \sum_{j=-N/2}^{N/2} P_j P_k \eta' \tag{2.8}$$

A factor of one half is added in (2.7) because of the double counting in the dual summation. (2.8)can be understood as the number of photons or amount of energy scattered off the subcarrier *i*, and should be equivalent to the photons scattered into this subcarrier *i* with large bandwidth assumption which we will clarify later. From now on, we drop index *i* and set it to zero, or equivalently, we are investigating the performance of centre wavelength channels in broad bandwidth DS-OFDM systems. We also assume all the subcarriers have the same power of *P* for the sake of simplicity. The FWM power at the centre subcarriers becomes

$$\begin{aligned}
P_{NL} &= 2\gamma^2 P^3 \sum_{k=-N/2}^{N/2} \sum_{j=-N/2}^{N/2} \eta_1' \eta_2' \\
\eta_1' &= \left| \frac{\sin\left(N_s j\left(k-j\right)\Delta f^{\,2} / \left(2 f_{PA}^2\right)\right)}{\sin\left(j\left(k-j\right)\Delta f^{\,2} / \left(2 f_{PA}^2\right)\right)} \right|^2 \\
\eta_2' &= \frac{1}{\beta_2^2 (2\pi)^4} \frac{1}{\Delta f^{\,4} j^2 \left(k-j\right)^2 + f_W^4} \\
f_{PA} &\equiv \frac{1}{2\pi}\sqrt{\frac{1}{\left|\beta_2\right| L \zeta}}, \qquad f_W \equiv \frac{1}{2\pi}\sqrt{\frac{\alpha}{\left|\beta_2\right|}}
\end{aligned} \tag{2.9}$$

where f_{PA} is defined as the phase array bandwidth indicating frequency range of the

effectiveness of phase array effects, f_W is the defined as the walk-off bandwidth indicating the frequency range of the effectiveness of FWM nonlinearity in the presence of the dispersion. Substituting a new variable $m = k - j$, (2.9) becomes

$$P_{NL} = \frac{2\gamma^2 P^3}{\beta_2^2 (2\pi)^4} \sum_{m=-N/2-j}^{N/2-j} \sum_{j=-N/2}^{N/2} \left| \frac{\sin\left(N_s jm \cdot \Delta f^2 / \left(2 f_{PA}^2\right)\right)}{\sin\left(jm \cdot \Delta f^2 / \left(2 f_{PA}^2\right)\right)} \right|^2 \frac{1}{\Delta f^4 j^2 m^2 + f_W^4} \quad (2.10)$$

(2.10) is similar to the result in [14] where the FWM products scattering into each subcarrier is formulated. To understand the complexity of (2.10), we use a typical system where subcarrier frequency spacing Δf of 100 MHz, and a total bandwidth of 400 GHz, which gives N_s of 4000 subcarriers. This implies that in order to compute the FWM effect, it requires a summation in the order of 16 millions (4000x4000) of FWM terms in (2.10). Aside from the apparent mathematical complexity, the physical interpretation of FWM dependence on various key system parameters is difficult to ascertain. It is highly desirable to have a concise closed-form solution to the nonlinearity products in (2.10).

Although corroborating by the numerical simulation using distributed Schrödinger equation is the ultimate validation of the closed-form solutions, we would like to go through step by step below stating our assumptions and intermediate derivations towards final analytical solutions, in order to ensure certain degree of mathematical rigorousness is enforced. In each step we first summarize the main task, lay out the assumption and its justification, and then present the operations as a result of the simplification.

(I) Conversion from discrete summation to integration. We observe that the FWM coefficient η_1 represents the phase array effects and the major contribution of the summation takes place where $jm \cdot \Delta f^2 / f_{PA}^2 \le 1$. This implies that dominate contribution is coming from the terms where $j = m = \mathrm{int}\left(f_{PA} / \Delta f\right)$ where 'int' is the integer round off function. In this work, we assume that phase array effect bandwidth f_{PA} is much larger than Δf, namely

$$f_{PA} >> \Delta f \tag{2.11}$$

which is generally true in CO-OFDM systems. It can be easily shown around $j = m = \mathrm{int}\left(f_{PA} / \Delta f \right)$, the phase $j\left(k - j\right)\Delta f^{2} / f_{PA}^{2}$ inside *sine* function is changing slowly each time when *j* or *m* is changed by 1, therefore the conversion from discrete summation is justified as far as the η_1 is concerned. Similarly if we assume the walk-off bandwidth f_W is much larger than the subcarrier spacing, namely

$$f_W >> \Delta f \tag{2.12}$$

conversion from discrete to integration can be also justified in relation to η_2. We call the conditions of (2.11) and (2.12) as 'dense subcarrier' assumption. Under the assumptions of (2.11) and (2.12), substituting the continuous integral variable f for $m \cdot \Delta f$, f_1 for $j \cdot \Delta f$, the FWM power is transformed into

$$\begin{aligned} P_{NL} &= \frac{2\gamma^2}{\beta_2^2 (2\pi)^4} \frac{P^3}{\Delta f^2} \int_{-B/2-f_1}^{B/2-f_1} \int_{-B/2}^{B/2} \eta_1\left(f, f_1 \right) \eta_2\left(f, f_1 \right) df_1 df \\ \eta_1\left(f, f_1 \right) &= \left| \frac{\sin\left(N_s f_1 f / \left(2 f_{PA}^2 \right) \right)}{\sin\left(f_1 f / \left(2 f_{PA}^2 \right) \right)} \right|^2 \\ \eta_2\left(f, f_1 \right) &= \frac{1}{\left(f_1 f \right)^2 + f_W^4} \end{aligned} \tag{2.13}$$

According to the definition of *m* in (2.10), the variable *f* represents the frequency of the multiplicative noise impairing the channel. We now introduce more convenient and also fundamentally more important terms, power (spectral) densities given by

$$I_{NL} \equiv \frac{P_{NL}}{\Delta f}, \qquad I \equiv \frac{P}{\Delta f} \tag{2.14}$$

where I_{NL} and I are respectively FWM noise (spectral) density and launch power (spectral) density. Substituting (2.14) into (2.13), we arrive at the FWM noise density

$$I_{NL} = \frac{2\gamma^2}{\beta_2^2 (2\pi)^4} I^3 \int_{-B/2-f_1}^{B/2-f_1} \int_{-B/2}^{B/2} \eta_1\left(f, f_1 \right) \eta_2\left(f, f_1 \right) df_1 df \tag{2.15}$$

where $B = N\Delta f$ is the total bandwidth of the DS-OFDM systems. The important conclusion is that under 'dense subcarrier' assumption, the result of the nonlinearity is independent of the subcarrier spacing.

(II) Conversion of the integration range to more manageable forms. The proof is given in the **Appendix A**. The FWM power density becomes

$$I_{NL} = \frac{8\gamma^2}{\beta_2^2(2\pi)^4} I^3 \int_{B_0/2}^{B/2} \int_0^{\infty} \eta_1(f, f_1)\eta_2(f, f_1)\, df_1 df \tag{2.16}$$

$$B_0 = 2 f_W^2 / B \tag{2.17}$$

$$B >> f_W \tag{2.18}$$

(2.18) is another important assumption that is used for deriving (2.16), which states that the overall bandwidth is much larger than the walk-off bandwidth. We call this condition 'large bandwidth' assumption which will be repeatedly used in the remainder of the section.

(III) Closed-form expressions for nonlinear noise density. Since *f* is the nonlinearity noise frequency, the integration over f_1 in (2.16) would generate the nonlinear noise spectral density. We rewrite (2.16) in terms of the one-sided nonlinear multiplicative noise spectral density $i_{NL}(f)$ given by

$$\begin{aligned} I_{NL} &= I \int_{B_0}^{B/2} i_{NL}(f) df \\ i_{NL}(f) &= \frac{2\gamma^2}{\beta_2^2(2\pi)^4} I^2 \int_0^{\infty} \eta_1(f, f_1)\eta_2(f, f_1)\, df_1 \end{aligned} \tag{2.19}$$

The nonlinear noise spectral density $i_{NL}(f)$ has the unit of dBc/Hz similar to phase noise or relative intensity noise (RIN). $i_{NL}(f)$ can be integrated into a close-form, the derivation of which is shown in **Appendix B**. The result of the integration gives

$$i_{NL}(f) = \gamma^2 I^2 \frac{2}{\pi\alpha|\beta_2|}\left(\frac{(N_s - 1 + e^{-\alpha\zeta L N_s} - N_s e^{-\alpha\zeta L})e^{-\alpha\zeta L}}{(e^{-\alpha\zeta L} - 1)^2} + \frac{N}{2}\right)\frac{1}{f} \tag{2.20}$$

(2.20) is the first important result of the chapter. The significance of (2.20) shows that the multiplicative nonlinear noise spectral density is essentially a well-known

flicker noise or *1/f* noise. This finding makes the authors deduce that our derivation may help explain one class of the flicker noise, namely, third order nonlinearity and dispersion may be one type of mechanisms to produce of *1/f* noise and the lower bound of the *1/f* noise signature, B_0 inversely proportional to the bandwidth of the participating noise, *B* as shown in (2.17). Substituting (2.20) into (2.19), we finally arrive at the closed form expression for the nonlinear noise density I_{NL}

$$\begin{aligned} I_{NL} &= \gamma^2 I^3 \frac{1}{\pi\alpha|\beta_2|}\left(\frac{2(N_s - 1 + e^{-\alpha\zeta LN_s} - N_s e^{-\alpha\zeta L})e^{-\alpha\zeta L}}{(e^{-\alpha\zeta L}-1)^2} + N_s\right) \\ &= \frac{\gamma^2 N_s \ln(B/B_0)\cdot h_e}{\pi\alpha|\beta_2|} I^3 \end{aligned} \tag{2.21}$$

$$h_e \equiv \frac{2(N_s - 1 + e^{-\alpha\zeta LN_s} - N_s e^{-\alpha\zeta L})e^{-\alpha\zeta L}}{N_s(e^{-\alpha\zeta L}-1)^2} + 1 \tag{2.22}$$

where h_e is the (noise) enhancement factor accounting for the FWM noise interference among different spans. We will discuss this interesting nonlinear enhancement factor h_e in more detail in the next section. We further express the nonlinear noise power density I_{NL} of (2.21) in a more concise form with the definition of nonlinear characteristic power density I_0 as follows:

$$I_{NL} = \left(\frac{I}{I_0}\right)^2 I, \qquad I_0 \equiv \frac{1}{\gamma}\sqrt{\frac{\pi\alpha|\beta_2|}{N_s h_e \ln(B/B_0)}} \tag{2.23}$$

(IV) Signal-to-noise ratio and spectral efficiency limit in the presence of nonlinearity. The signal power in presence of the nonlinear interference can be expressed as [18]

$$I = I\exp\left(-(I/I_0)^2\right) \cong I \tag{2.24}$$

The noise can be considered as the summation of the white optical amplified-spontaneous-noise (ASE), n_0 and the FWM noise, and is given by [18]

$$
\begin{aligned}
n &= n_0 + I\left(1-\exp\left(-\left(I/I_0\right)^2\right)\right) \\
n_0 &= N_s\left(G-1\right)n_{sp}h\upsilon \cong 0.5N_s e^{\alpha L}h\upsilon \cdot NF
\end{aligned}
\tag{2.25}
$$

where n_{sp} is the spontaneous noise factor equal to half of the noise figure of the optical amplifier *NF*, h is the Planck constant, and υ is the light frequency. The signal-to-noise is thus given by

$$
SNR = \frac{I\exp\left(-\left(I/I_0\right)^2\right)}{n_0 + I\left(1-\exp\left(-\left(I/I_0\right)^2\right)\right)} \tag{2.26}
$$

For the SNR larger than 10, (2.26) can be approximated as

$$
SNR \cong \frac{I}{n_0 + I\left(I/I_0\right)^2} \tag{2.27}
$$

The simplification is generally valid for the case of interests where the signal power density is much smaller than I_0.

We have verified through our simulation under 'dense subcarrier' and 'large bandwidth' assumptions of (2.11), (2.12), and (2.18), the FWM noise is of Gaussian distribution. Under the assumption of Gaussian noise distribution, the information spectral efficiency (defined as the maximum information capacity *C* normalized to bandwidth *B*) for single-polarization is readily given by [22].

$$
\begin{aligned}
S &= \log_2\left(1+SNR\right) \\
&= \log_2\left(1+\frac{I\exp\left(-\left(I/I_0\right)^2\right)}{n_0 + I\left(1-\exp\left(-\left(I/I_0\right)^2\right)\right)}\right) \\
&\cong \log_2\left(1+\frac{I}{n_0 + I\left(I/I_0\right)^2}\right)
\end{aligned}
\tag{2.28}
$$

From (2.28), the maximum spectral efficiency S_{opt} in the presence of fibre nonlinearity can be easily shown as

$$
S_{opt} = \log_2\left(1+\frac{1}{3}\left(2I_0/n_0\right)^{2/3}\right) \tag{2.29}
$$

(V) Optimal launch power density, maximum Q, and nonlinear threshold of launch power density. In (2.28), the ultimate spectral efficiency is obtained. However in practice, the performance is always lower because of the practical implementation of modulation and coding. We therefore derive a few important parameters that are commonly used in the optical communications community. The first one is the maximum achievable Q factor. Under the Gaussian noise assumption and QPSK modulation, the Q factor is equal to the SNR given by

$$Q = SNR = \frac{I \exp\left(-\left(I / I_0\right)^2\right)}{n_0 + I\left(1 - \exp\left(-\left(I / I_0\right)^2\right)\right)} \cong \frac{I}{n_0 + I\left(I / I_0\right)^2} \qquad (2.30)$$

The optimum launch power density is another important parameter and is defined as the launch power density where the maximum Q takes place. By simply differentiating Q of (2.30) over *I*, and setting it to zero, we obtain the optimum launch power density and the optimal Q given by

$$I_{opt} = \left(n_0 I_0^2 / 2\right)^{1/3} = \left(\frac{n_0 \pi \alpha \left|\beta_2\right|}{2\gamma^2 N_s h_e \ln\left(B / B_0\right)}\right)^{1/3} \qquad (2.31)$$

$$Q_{max} = \frac{1}{3}\left(2I_0 / n_0\right)^{2/3} = \frac{\left(4\pi\alpha\left|\beta_2\right|\right)^{1/3}}{3\left(n_0{}^2\gamma^2 N_s h_e \ln\left(B / B_0\right)\right)^{1/3}} \qquad (2.32)$$

One of the inconveniences of using the optimum launch power expression in (2.31) is that it is dependent on the amplifier noise figure. The other commonly used term is nonlinear threshold launch power density that is defined as the maximum launch power density at which the BER due to the nonlinear noise can no longer be corrected by a certain type of forward-error-code (FEC). For standard Reed-Solomon code RS(255, 239), the threshold *Q* is 9.8 (dB), or linear q_0 of 3.09. In (2.30), setting n_0 to zero and *Q to* q_0^2, we arrive at the nonlinear threshold of power density

$$I_{th} = \frac{I_0}{q_0} = \frac{1}{q_0 \gamma}\sqrt{\frac{\pi\alpha\left|\beta_2\right|}{N_s h_e \ln\left(B / B_0\right)}} \qquad (2.33)$$

whereq_0 is the correctable linear Q for a specific FEC.

The closed-form expressions for nonlinear noise spectral density $i_{NL}(f)$ in (2.20),

nonlinear noise power density I_{NL} in (2.21), nonlinear multi-span noise enhancement factor h_e in (2.22), nonlinear characteristic power density I_0 in (2.23), information spectral efficiency *S* in (2.28), system Q factor and its optimal value in (2.30) and (2.32), optimal launch power density in (2.31), and nonlinear threshold of launch power density in (2.33) comprise the major findings in this work.

2.1.2 Corroboration of the Theories with Numerical Simulation

During the derivation in section 2.1.1, many assumptions and approximations are made in order to arrive at concise closed-form expressions. The concern is that whether several approximations may accumulate and make the closed-form solutions inaccurate. In this section, we intend to corroborate the theoretical results with the numerical simulations. Among all the analytical results, the FWM noise density I_{NL} of (2.21) is the most fundamental one, and other expressions can be considered as the derivatives of the I_{NL}. We have conducted simulation to validate the expression for I_{NL}.

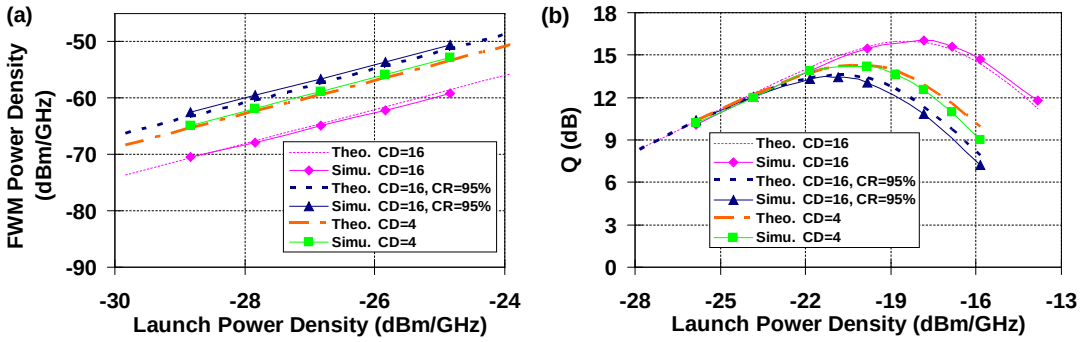

Figure 2.2. Comparison of closed-form theory and simulation results for (a) FWM power density, and (b) Q factor as a function of the launch power density. Theo.: Theory; Simu.: Simulation; CD: Chromatic dispersion with a unit of ps/nm/km; CR: (CD) compensation ratio. Both (a) and (b) assume 10x100 km single-polarization transmission systems.

The parameters for the simulated systems are as follows: 16 wavelength channels, each covering 31-GHz bandwidth, giving total bandwidth B of 496 GHz; OFDM subcarrier frequency spacing of 85 MHz; QPSK modulation for each subcarrier; no frequency guard band between wavelength channels; 10-span of 100 km fibre link;

fibre loss α of 0.2 dB/km; nonlinear coefficient $\gamma = 1.22 w^{-1} km^{-1}$; noise figure of the amplifier of 6 dB; The FWM noise density is simulated by using an perfect optical notch filter to notch out 100 MHz gap at the centre of the input signal spectrum, and the power density is measured at the output after 1000-km transmission. Figure 2.2(a) shows the simulated nonlinear noise density compared with the computed nonlinear density using the closed-form expression of (2.21). Three transmission systems are investigated: (i) SSMF type system with CD of 16 ps/nm/km without any dispersion compensation, abbreviated as 'system I', (ii) CD of 16 ps/nm/km, but with dispersion 95% compensated per span, abbreviated as system II, and (iii) non-zero dispersion-shifted type fibre with CD of 4 ps/nm/km, abbreviated as 'system III'. For systems I, II, and III, the average difference of FWM density is 14%, 12%, and 17%. This shows excellent match between the closed-form formula and simulation, considering the extreme sensitivity of the FWM density as a function of launch power density (cubic dependence). We also perform the simulation of the system Q factors with the above-described three systems, the results of which is shown in Figure 2.2(b). We can see a good match between theoretical expressions based on (2.23) and (2.30) and simulation results. For instance, the difference between the optimal Q from theory and simulation is within 0.15 dB for all simulated dispersion maps. The difference of launch power between the simulation and closed-form theory for the same Q factor is less than 0.4 dB for wide range of launch power density of -28 to -16 dBm/GHz. All these confirm the excellent match between the simulation and the closed-form expression of Q factors in (2.30).

2.1.3 Discussion of the Closed-form Expression

Because the concise closed-form expressions are available, we are ready to quickly identify their dependence on system parameters including fibre dispersion, number of spans, dispersion compensation ratio, and overall bandwidth. In the following part, we will discuss in detail the achieved system Q factor, optimum launch power, information spectral efficiency, and multi-span noise enhancement factor.

(I) System Q factor and optimum launch power

The immediate benefits of having closed-form formulas of (2.31) and (2.32) for system Q factor and optimum launch power density are their scaling over the underlying parameters. From (2.31) and (2.32), it follows that for every 3 dB increase in fibre dispersion, there is 1 dB increase in the optimal launch power density and the achievable Q; for every 3 dB increase in fibre nonlinear coefficient γ, there is 2 dB increase in the optimal launch power and achievable Q. We can quickly generate the optimum launch power and achievable Q for variety of dispersion maps. We use the three systems, system I, II and III studied in Figure 2.3 as an example. As shown in Figure 2.3(a), system I has the best performance due to large local dispersion and no per-span dispersion compensation. The advantage of system I over system II increases with the increase of the number of spans, for instance from 0 dB to 2.4 dB when the reach increases from single-span to 10 spans. The advantage of system I over system III is maintained at 1.7 dB independent of the number of spans. However, Figure 2.3(b) shows the optimal launch power versus number of spans. The optimum launch power for non-compensated systems, system I and III are constant. This is because both linear and nonlinear noises increase linearly with the number of the spans that leads to the optimum power independent of the number of spans. However, for the dispersion compensated system II, the optimum launch power density decreases with number of spans due to the multi-span noise enhancement effect. Another interesting observation from (2.31) and (2.32) is that both the optimal Q factor and launch power has very week dependence on the overall system bandwidth: proportional to 1/3 power of logarithm of the overall bandwidth. It can be easily shown that for both system I and II, the Q is decreased by only about 0.7 dB with the 10-fold increase of the overall system bandwidth from 400 to 4000 GHz whereas system II incurs a larger decrease of the Q factor of 0.84 dB with the same bandwidth increase.

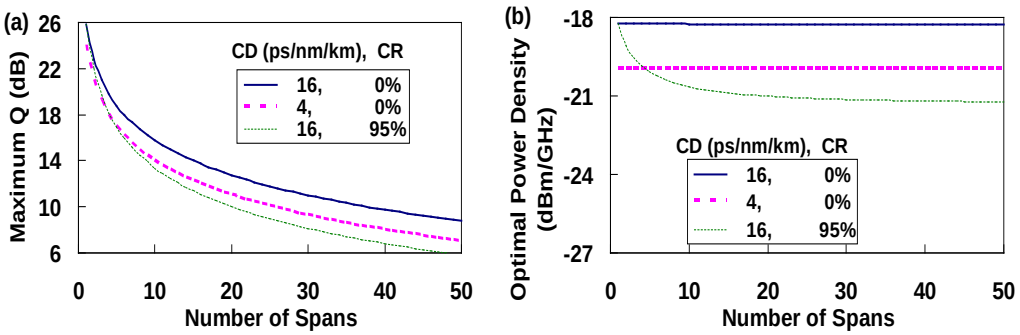

Figure 2.3. (a) The maximum Q factor, and (b) the optimal launch power density versus number of spans with various dispersion maps. CD: chromatic dispersion. CR: (CD) compensation ratio

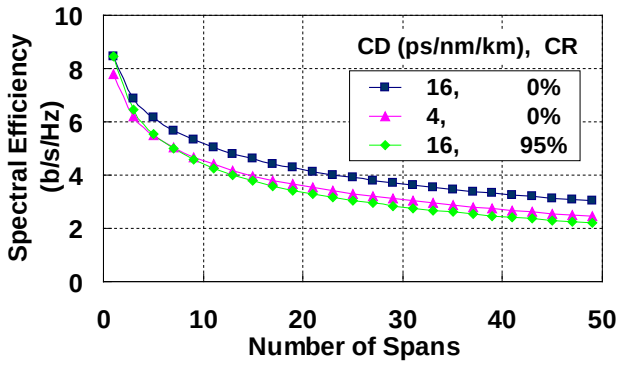

Figure 2.4. Information spectral efficiency as a function of the number spans for various dispersion maps. The total bandwidth B is assumed to be 40 nm. The other OFDM and link parameters are the same as those described at the beginning of this section.

(II)Information spectral efficiency

The information spectral efficiency is important as it represents the ultimate bound of what we can achieve by employing all possible modulations (of course not limited to QPSK) and codes. For large SNR, we simplify (2.28) into

$$\begin{aligned} S &= \log_2\left(\frac{1}{3}\left(2I_0/n_0\right)^{2/3}\right) \\ &= \log_2\left(\frac{1}{3}\left(4\pi\alpha\left|\beta_2\right|\right)^{1/3}\left(\gamma^2 n_0 N_s h_{PA}\ln\left(B/B_0\right)\right)^{-1/3}\right) \end{aligned} \tag{2.34}$$

(2.34)clearly shows the challenges of improving spectral efficiency by redesigning the fibre system parameters: to increase spectral efficiency by 1 bit/s/Hz, the dispersion

needs to be increased by a factor of 8, or the nonlinear coefficient γ be decreased by a factor of 2.8, or number of spans be reduced by a factor of 2, all of which are difficult to achieve. In a nutshell, it is of diminishing return to improve the spectral efficiency by modifying the optical fibre system parameters. The only effective method to substantially improve the spectral efficiency is to add more dimensions such as resorting to polarization multiplexing that leads to a factor of 2 improvement, or fibre mode multiplexing by at least a factor of two or more dependent on the capability of achievable digital signal processing (DSP). Figure 2.4 shows the achievable spectral efficiency for the three studied systems. The only modification is that we assume 40 nm or 5 THz for the total bandwidth. The spectral efficiency for the system I, II, and III are respectively 5.17, 4.40, and 4.52 b/s/Hz. This shows a total capacity of 25 Tb/s can be achieved for 10x100 SSMF uncompensated EDFA-only single-polarization systems within C-band.

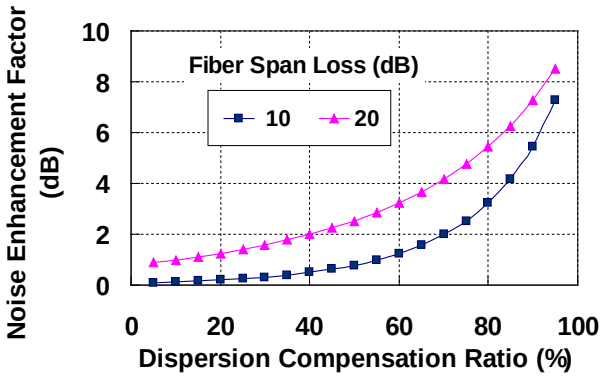

Figure 2.5. Multi-span noise enhancement factor as a function of the dispersion compensation ratio with fibre span losses of 10 and 20 dB. The number of spans is maintained at 10. The link losses of 10 and 20 dB are obtained by setting the span length to 50 and 100 km respectively.

(III) Multi-span noise enhancement factor

The multi-span noise enhancement factor h_e of (2.22) is one of the most important findings in this report. This noise enhancement effect is ignored in the prior analytical results [18]. This multi-span interference effect can be understood as the phase array effect that has been discussed in report [14]. The noise enhancement is referred to the

important fact that the overall nonlinear FWM noise of multi-span systems is enhanced by a factor of h_e over the scenario for which the nonlinear FWM noise originated in each span is assumed independent without interference with each other. We note the expression of h_e in (2.22) is the first concise close-from result where the multi-span interference effects of all the FWM products are accounted for. From (2.22), we conclude that as long as the factor $\alpha L\zeta$ is much larger than 1, h_e approaches 1, namely, the nonlinear noise generated in each span can be treated independently in this regime. However, even when the fibre loss αL is large but ζ is small, or dispersion compensation ratio is large, h_e can be significantly high. Figure 2.5 shows the noise enhancement factor h_e as a function of dispersion compensation ratio $\rho = 1-\zeta$ for span losses of 10 and 20 dB. It can be seen that for a dispersion compensation ratio of 95%, the nonlinear noise is enhanced by 8.5 and 7.3 dB for span losses of 10 and 20 dB respectively. It shows that multi-span noise enhancement can not be ignored even when the span loss is as large as 20 dB if the compensation ratio is higher than 50 %.

Appendix A: Change of the integration range.

We first argue that we can move the integration boundary for *f* from [-*B*/2-f_1, *B*/2-f_1] to more tidy form of [-*B*/2, *B*/2]. This is reasonable simplification as the major contribution of the integral is when *f* is around f_W. In essence, this fringe effect of subtracting f_1 can be ignored when $B >> f_W$. This corresponds to the 'large bandwidth' assumption in (2.18). Under the large bandwidth assumption, (2.15) can be rewritten as

$$
\begin{aligned}
I_{NL} &= \frac{8\gamma^2 I^3}{\beta_2^2 (2\pi)^4} I_{NL}^1 \\
I_{NL}^1 &= \frac{1}{4} \int_{-B/2}^{B/2} \int_{-B/2}^{B/2} \eta_1(f, f_1)\eta_2(f, f_1) df_1 df \\
\eta_1(f, f_1) &= \left| \frac{\sin\left(N_s f_1 f / \left(2 f_{PA}^2\right)\right)}{\sin\left(f_1 f / \left(2 f_{PA}^2\right)\right)} \right|^2 \\
\eta_2(f, f_1) &= \frac{1}{\left(f_1 f\right)^2 + f_W^4}
\end{aligned}
\tag{2.35}
$$

where I_{NL} and I_{NL}^1 differs merely by a constant factor. We will focus on our simplifying effort on I_{NL}^1. Using symmetry over zero for the integral variables f_1 and f, (2.35) can be expressed as

$$
I_{NL}^1 = \int_0^{B/2} \int_0^{B/2} \eta_1(f, f_1)\eta_2(f, f_1)\, df_1 df \tag{2.36}
$$

We now partition I_{NL}^1 into three regions of integration as follows:

$$
I_{NL}^1 = A_1 - A_2 + A_3 \tag{2.37}
$$

where

$$
\begin{cases}
A_1 = \int_{B_0/2}^{B/2} \int_0^{\infty} \eta_1 \eta_2 df_1 df \\
A_2 = \int_{B_0/2}^{B/2} \int_{B/2}^{\infty} \eta_1 \eta_2 df_1 df \\
A_3 = \int_0^{B_0/2} \int_0^{B/2} \eta_1 \eta_2 df_1 df
\end{cases}
\tag{2.38}
$$

$$
B_0 = 2 f_W^2 / B
$$

We will show below that A_1 is dominant over A_2 and A_3, and therefore the contribution of A_2 and A_3 can be omitted as a good approximation.

We first study the special case of N_s of 1. It is one of the most important cases as it corresponds to the system scenarios for which nonlinear noises originated from different spans are uncorrelated, and the overall noise is simply N_s times of the noise of

one span. As we show later, an uncompensated fibre system is almost a perfect example of independent span noises. Substituting $N_s = 1$ into (2.38), it can be easily shown that A_1 can be completely integrated in a closed-form as

$$A_1 = \frac{\pi}{2 f_W^2} \ln\left(B / B_0\right) \tag{2.39}$$

We now carry out the integration for A_2 over f_1, we have

$$\begin{aligned} A_2 &= \int_{B_0/2}^{B/2} \frac{1}{f \cdot f_W^2} \arctan\left(\frac{f_W^2}{f \cdot B/2}\right) df \le \int_{B_0/2}^{B/2} \frac{1}{f \cdot f_W^2} \frac{f_W^2}{f \cdot B/2} df \\ &= \frac{1}{B/2} \int_{B_0/2}^{B/2} \frac{1}{f^2} df = \frac{1}{B/2} \cdot \frac{1}{B_0/2} = \frac{2}{f_W^2} \end{aligned} \tag{2.40}$$

In (2.40), we have used the inequality of $x > \arg\tan(x)$ for $x > 0$, and $B >> B_0$, which can be considered as part of the 'large bandwidth' assumption. It can be seen that A_2 is upper bounded by $2 / f_W^2$, the ratio between A_1 /A_2 is upper bounded by $\frac{\pi}{4} \ln\left(B / B_0\right)$. Under large bandwidth assumption of $B >> f_W$, we consider this is a large number and thus A_2 in general can be ignored. The upper bound for the term A_3 can be found as follows

$$\begin{aligned} A_3 &= \int_0^{B_0} \int_0^{B/2} \frac{1}{\left(f_1 f\right)^2 + f_W^4} df_1 df \\ &< \int_0^{B_0/2} \int_0^{B/2} \frac{1}{f_W^4} df_1 df \\ &= \frac{1}{f_W^4} \left(B_0 / 2\right) \cdot B/2 = \frac{1}{2 f_W^2} \end{aligned} \tag{2.41}$$

Therefore the ratio between A_1/A_3 is upper bounded by $\pi \ln\left(B / B_0\right)$. Consequently under the large bandwidth assumption, A_1 is the dominant contribution to I_{NL}^1, and can be used as an good approximation to I_{NL}^1.

We now move to the multi-span scenario for which there is an additional factor of η_1 in the integrand of (2.38). We show that by introducing this factor, the conclusion

that A_1 being a dominate component in P_{NL}^1 still stands. η_1 generates a interference pattern with a main lobe in the low frequency region. When considering the ratio between A_1 and A_2, the weight will shift toward A_1 as A_1 is integrated at the low frequency of f_1, [0, B/2], and A_2 is integrated at the high frequency of f_1, [B/2, ∞]. Therefore the ratio of A_1/A_2 should be no less than $\frac{\pi}{4}\ln(B/B_0)$ we derived for $\eta_1 = 1$ for the single-span case, and subsequently A_2 can be ignored to a good degree of approximation. Regarding the ratio of A_1/A_3, the integration interval 'f' is over low frequency region of [0, B_0/2] for 'A_3' whereas over [B_0/2, B/2] for A_1. So the existence of the phase array pattern η_1 will shift weight toward A_3. However, we will show the ratio of A_1/A_3 is still upper bounder by a factor in the order of $\pi\ln(B/B_0)$ to a good approximation. The phase array effects dependent on the phase difference between each span largely determined by f_{PA}. When $f_{PA} >> f_W$, for instance, the dispersion is almost completely compensated, η_1 remains a constant over a large range frequency range. This is closed to the scenario for the single-span case for which we have shown A_3 can be ignored. Therefore we only need to study the ratio of A_1/A_3 when $f_{PA} << f_W$ as this is the scenario for which the main lob shifts close to the low frequency, favouringA_3. We would like to derive the ratio of A_1/A_3 when $f_{PA} << f_W$. η_1 can be also expressed as

$$\begin{aligned}\eta_1 &= \left|1 + e^{-j\theta} + e^{-j2\theta} + ... + + e^{-j(N-1)\theta}\right|^2 \\ &= N + 2\sum_{n=1}^{N-1}(N-n)\cos(n\theta) \\ \theta &= f \cdot f_1 / f_W^2\end{aligned} \qquad (2.42)$$

Substituting (2.42) into (2.38), we have

$$
\begin{aligned}
A_3 &= \int_0^{B_0/2}\int_0^{B/2} \eta_1 \frac{1}{(f_1 f)^2 + f_W^4} df_1 df \le \frac{1}{f_W^4}\int_0^{B_0/2}\int_0^{B/2} \eta_1 df_1 df \\
&= \frac{1}{f_W^4}\int_0^{B_0/2}\int_0^{B/2}\left[N + 2\sum_{n=1}^{N_S-1}(N_S-n)\cos(nf\cdot f_1 / f_{PA}^2)\right] df_1 df \\
&= \frac{N_s}{2f_W^2} + 2\frac{1}{f_W^4}\sum_{n=1}^{N-1}(N_S-n)\int_0^{B_0/2}\int_0^{B/2}\cos(nf\cdot f_1 / f_{PA}^2) df_1 df \\
&= \frac{N_s}{2f_W^2} + 2\frac{1}{f_W^4}\sum_{n=1}^{N-1}(N_S-n)\int_0^{B_0/2}\frac{f_{PA}^2}{nf}\sin\left(nf\cdot B/\left(2f_{PA}^2\right)\right) df \\
&= \frac{N_s}{2f_W^2} + 2\frac{1}{f_W^4}\sum_{n=1}^{N-1}(N_S-n)\frac{f_{PA}^2}{n}\int_0^{\frac{n\cdot f_W^2}{4f_{PA}^2}}\frac{1}{f}\sin(f) df
\end{aligned}
\tag{2.43}
$$

As the upper boundary of integration for variable f in (2.43), $nf_W^2/\left(4f_{PA}^2\right)$ is much larger than 1 under the assumption of $f_{PA} << f_W$, and can be considered approximated as infinity. Using formula $\int_0^\infty \sin(f)/f\, df = \pi/2$ and after some simple arrangement, (2.43) can be transformed into

$$
\begin{aligned}
A_3 &\le \frac{N_s}{f_W^2} + \frac{\pi f_{PA}^2}{f_W^4}\sum_{n=1}^{N-1}\frac{(N_S-n)}{n} f_{PA}^2 \\
&\approx \frac{N_s}{2f_W^2} + \frac{\pi f_{PA}^2\left(N_s\log N_s - N_s + 1\right)}{f_W^4} \approx \frac{N_s}{2f_W^2}
\end{aligned}
\tag{2.44}
$$

In (2.44), we have used the assumption of $f_{PA} << f_W$ to justify omitting the second term. It can be also shown that using the closed-form developed for A_1 in **Appendix B**, under assumption of $f_{PA} << f_W$, A_1 can be approximated as

$$
A_1 = \frac{\pi N_s}{2f_W^2}\ln\left(B/B_0\right) \tag{2.45}
$$

Combing (2.44) and (2.45), we conclude that A_1/A_3 is also upper bounded in the order of $\pi\ln\left(B/B_0\right)$. In summary, we conclude that A_1 can be used as an approximation for I_{NL}^1 for a wide range of the system parameters. Unless specifically mentioned in this chapter, we consider

$$I_{NL} = \frac{8\gamma^2 I^2}{\beta_2^2 (2\pi)^4} I_{NL}^1$$
$$I_{NL}^1 = \int_{B_0/2}^{B/2} \int_0^{\infty} \eta_1(f, f_1)\eta_2(f, f_1)\, df_1 df \tag{2.46}$$

Using the definition of $i_{NL}(f)$ in (2.19), we have

$$i_{NL}(f) = \frac{8\gamma^2 I^2}{\beta_2^2 (2\pi)^4} i_{NL}^1(f)$$
$$i_{NL}^1(f) = \int_0^{\infty} \eta_1(f, f_1)\eta_2(f, f_1)\, df_1 \tag{2.47}$$

There are two other important factors that make (2.46) a very good approximation: First, in(2.37), not only are A_2 and A_3 small compared to A_1, but they also have opposite signs and their combined effects tend to cancel each other, which further improves the accuracy of using A_1 as an approximation to I_{NL}^1. Second, the phase array effect will tend to deemphasize the contribution of A_2 and add more weight to A_3. However, because A_3 is integrated in the low frequency of f, in practical application, the low frequency noise including DC components can be estimated and removed. Therefore the lower integration boundary for f, $B_0/2$ in (2.46) can be also interpreted as that the low frequency noise from [0, $B_0/2$] is being removed due to the phase estimation. Therefore, to be complete, we redefine the B_0 as

$$B_0 = \max\left(2 f_W^2 / B,\ 2B_{PE}\right) \tag{2.48}$$

where B_{PE} is the phase estimation bandwidth which is equal to half of the subcarrier channel spacing Δf in CO-OFDM systems, or the phase locked loop (PLL) bandwidth in single-carrier systems. This is to accommodate the scenario for which the phase estimation bandwidth is high enough such that the lower integration boundary for $f$in (2.46) should be B_{PE} instead of f_W^2 / B.

Appendix B: Closed-form solution for FWM noise spectral density

In deriving close-form for I_{NL}^1 we will repeatedly employ a useful formula of

complex functional analysis as follows:

$$\int_{-\infty}^{\infty} \frac{f(x)}{x^2 + a^2} dx = \frac{\pi}{a} f(ia) \tag{2.49}$$

where $f(x)$ is an analytical function over the upper half of the complex plane. Substituting (2.42) into (2.47) , we have

$$\begin{aligned} i_{NL}^1(f) &= \frac{1}{f} \int_0^{\infty} \left[N + 2 \sum_{n=1}^{N_S - 1} (N_S - n) \cos(n f_2 / f_{PA}^2) \right] \frac{1}{f_2^2 + f_W^4} df_2 \\ &= \frac{1}{2f} \mathrm{Re} \left\{ \int_{-\infty}^{\infty} \left[N + 2 \sum_{n=1}^{N_S - 1} (N_S - n) \exp(jn f_2 / f_{PA}^2) \right] \frac{1}{f_2^2 + f_W^4} df_2 \right\} \end{aligned} \tag{2.50}$$

where 'Re' stands for operation of extracting the real component. We have exchanged variable $f_1 f$ to f_2 in (2.50). Applying formula of (2.49) into (2.50), we obtain

$$\begin{aligned} i_{NL}^1(f) &= \frac{1}{2f} \left\{ N_s + 2 \sum_{n=1}^{N_S - 1} (N_S - n) \exp(-n f_W^2 / f_{PA}^2) \right\} \\ &= \frac{\pi}{2f \cdot f_W^2} \left\{ \frac{2(N_s - 1 + e^{-N_s f_W^2 / f_{PA}^2} - N_s e^{-f_W^2 / f_{PA}^2}) e^{-f_W^2 / f_{PA}^2}}{(e^{-f_W^2 / f_{PA}^2} - 1)^2} + N_s \right\} \end{aligned} \tag{2.51}$$

Substituting the definitions for f_W and f_{PA} in (2.9) into (2.51), we have

$$i_{NL}^1(f) = \frac{2\pi^3 |\beta_2|}{f \cdot \alpha} \left\{ \frac{2(N_s - 1 + e^{-N_s \alpha L \zeta} - N_s e^{-\alpha L \zeta}) e^{-\alpha L \zeta}}{(e^{-\alpha L \zeta} - 1)^2} + N_s \right\} \tag{2.52}$$

Substituting (2.52) into (2.47), we arrive at the FWM noise spectral density

$$i_{NL}(f) = \frac{\gamma^2}{\pi} \frac{I^2}{\alpha |\beta_2|} \left\{ \frac{2(N_s - 1 + e^{-N_s \alpha L \zeta} - N_s e^{-\alpha L \zeta}) e^{-\alpha L \zeta}}{(e^{-\alpha L \zeta} - 1)^2} + N_s \right\} \frac{1}{f} \tag{2.53}$$

2.2 Preliminary Study on Information Capacity of CO-OFDM Transmission via TMF

It has been discussed in section 2.1 and other research works that there exists a fundamental Shannon capacity limit due to fibre nonlinearity in SMF optical systems [19, 20, 23]. Recent demonstrations show that on SMF platform, this capacity limit has been quickly approached within some practical engineering margin [5, 24, 25]. As a

result, multi-core fibre (MCF) and few-mode fibre (FMF) were proposed to keep up with the dramatic capacity improvement [26-29]. In MCF, the optical signals are carried on several individual cores [26, 27], and the inter-core nonlinear interaction is minimized. Therefore, the system capacity is expected to be increased by the number of cores. For FMF based transmission, there is strong field overlapping between different modes, and subsequently it is important to analyse the FMF systems taking into account potential inter-modal nonlinearity. Therefore, in this section, the previously derived closed-form expressions for channel capacity [19, 20] from SMF are extended to FMF systems [30]. We then conduct experiments to measure these nonlinear coefficients for a customized two-mode fibre (TMF) (actually containing three spatial modes including one LP_{01} mode and two degenerate LP_{11} modes, LP_{11}^{a} and LP_{11}^{b}). It is found that despite strong spatial overlapping of the 3 modes in TMF, the channel capacity approaches to 3 times of that of SMF. Moreover, there could be an advantage of using FMF as opposed to MCF in terms of higher integration density and power efficiency [30]. Our research outcomes show that by densely packing optical signals into a few modes does not significantly reduce the link capacity limit in comparison with much loosely packed MCF systems.

2.2.1 Capacity Limit for FMF Based CO-OFDM Systems

The channel capacity can be estimated by filling all the bandwidth with densely-spaced OFDM subcarriers as shown in Figure 2.6. When the spectrum is

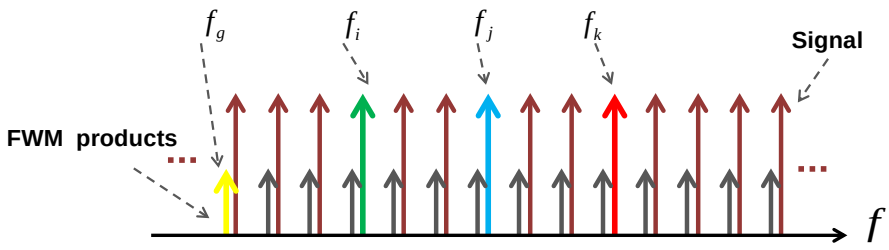

Figure 2.6. Schematic of densely-spaced subcarriers with four-wave mixing products.

continuously occupied, the nonlinear effects such as self-phase modulation (SPM), cross-phase modulation (XPM), and four-wave mixing (FWM) can be considered as

FWM [19, 20]. Due to the FWM effect, the interaction of subcarriers at the frequencies of f_i, f_j, and f_k produces a mixing product at the frequency of $f_g = f_i + f_j - f_k$. The magnitude of the FWM product for one span of a fibre link is given by [19, 20]

$$\boldsymbol{c}'_{\boldsymbol{m}_g,\boldsymbol{g}} = \gamma_{ijkg}\left[\left(\boldsymbol{c}^{+}_{\boldsymbol{m}_k,\boldsymbol{k}}\boldsymbol{c}_{\boldsymbol{m}_i,\boldsymbol{i}}\right)\boldsymbol{c}_{\boldsymbol{m}_j,\boldsymbol{j}} + \left(\boldsymbol{c}^{+}_{\boldsymbol{m}_k,\boldsymbol{k}}\boldsymbol{c}_{\boldsymbol{m}_j,\boldsymbol{j}}\right)\boldsymbol{c}_{\boldsymbol{m}_i,\boldsymbol{i}}\right]e^{-\alpha L/2 - i\beta_g L}\frac{1-e^{-\alpha L}e^{-j\Delta\beta_{ijk}L}}{j\Delta\beta_{ijk}+\alpha} \quad (2.54)$$

where $\boldsymbol{c}_{\boldsymbol{m}_i,\boldsymbol{i}}$ is the optical field in Jones vector form for the frequency f_i in the mode m_i, $\beta_{m_i,i}$ is the wavenumber for the frequency f_i, $\Delta\beta_{ijk} \equiv \beta_{m_i,i} + \beta_{m_j,j} - \beta_{m_k,k} - \beta_{m_g,g}$ represents the phase mismatch for the FWM product, and L is the length of the fibre. The subscript for mode at times is dropped for brevity. Without loss of generality, we assume all the modes have the same loss coefficient of α. γ_{ijkg} is the nonlinear coefficient between the four waves, expressed as

$$\gamma_{m_i m_j m_k m_g} = \frac{n_2\omega_0}{A_{m_i m_j m_k m_g} c}$$

$$A_{m_i m_j m_k m_g} = \frac{\left[\left\langle\left|F_{m_i}\right|^2\right\rangle\left\langle\left|F_{m_j}\right|^2\right\rangle\left\langle\left|F_{m_k}\right|^2\right\rangle\left\langle\left|F_{m_g}\right|^2\right\rangle\right]^{1/2}}{\left\langle F_{m_i}{}^{*}F_{m_j}{}^{*}F_{m_k}F_{m_g}\right\rangle} \quad (2.55)$$

where '< >' stands for integration over the cross-section of the fibre, n_2 is the intrinsic nonlinear coefficient of fibre equal to 2.41x10^{-20} m^2/W, ω_0 is the centre frequency of the FWM, c is the speed of light, $A_{m_i m_j m_k m_g}$ is the effective area of the nonlinear interaction, and F_k is the mode profile for the frequency component k. From Eq. (1), for FMF to be effective, it is very critical that $\Delta\beta_{ijk}$ is maintained to be small on the order of fibre loss coefficient of α. There are two mechanisms that greatly reduce the FWM impact:

(i) Modal wavenumber mismatch. Assume that β_i and β_j are in the same mode, but β_k and β_g are in the other modes, then $\Delta\beta_{ijk} = \Delta\beta$ where $\Delta\beta$ is the wavenumber

mismatch between the LP_{01} and LP_{11} modes. $\Delta\beta$ is a few orders of magnitude larger than α [28], and therefore makes the FWM effects insignificant.

(ii) Modal group delay mismatch. Assume that β_i and β_k are in the same mode, e.g., in LP_{01} mode, but β_j and β_g are in the other mode, LP_{11} mode. This is equivalent to classical cross-phase modulation. Then we have

$$\Delta\beta_{ijk} \equiv \beta_{m_i,i} + \beta_{m_j,j} - \beta_{m_k,k} - \beta_{m_g,g} = \Delta\omega\left(1/\upsilon_g^{m_i} - 1/\upsilon_g^{m_j}\right) \quad (2.56)$$

where $\Delta\omega$ is the angular frequency difference between frequency component *i* and *k*. $\upsilon_g^{m_{i,j}}$ is the group velocity for mode *i* or *j*. The group delay mismatch between two LP_{01} and LP_{11} modes gives a value of a few ps/m [28], indicating that as long as $\Delta\omega$ is larger than several tens of MHz, the FWM or nonlinear interaction is also negligible.

The modal group delay mismatch between two LP_{11} modes are less than that between LP_{11} and LP_{01}. However, it is still measured at a few hundreds ps/km for our customized fibre, implying that as long as $\Delta\omega$ is larger than a few hundreds of MHz, the FWM or nonlinear interaction is also negligible. The wavenumber mismatch is larger than group delay mismatch. All these indicate the nonlinear interactions between two LP_{11} modes are also negligible. Now we can conclude that to have significant nonlinear effects, all the four waves should be in the same mode. Otherwise, the produced FWM is insignificant due to modal wavenumber or group delay mismatch. Based on these observations, the spectral efficiency (SE) for three modes (S_t) can be the summation of SE from three individual modes S_i. S_i is given by [19, 20]

$$\begin{aligned}
&S_t = \sum_{i=1}^{3} S_i \\
&S_i \cong 2\log_2\left(\frac{1}{3}\left(8\pi\alpha_i\left|\beta_i\right|\right)^{1/3}\left(3\gamma_i{}^2 n_0^2 N_s h_e \ln\left(B/B_0\right)\right)^{-1/3}\right) \\
&n_0 = N_s N_0 \\
&N_0 = \left(G-1\right)n_{sp}h\upsilon \cong 0.5e^{\alpha_i L}h\upsilon\cdot NF \\
&B_0 = \alpha_i/\left(2\pi^2\left|\beta_i\right|B\right)
\end{aligned} \quad (2.57)$$

where *i* of 1, 2, 3 stands for modes of LP_{01}, LP_{11}^a and LP_{11}^b respectively, $\gamma_i = \gamma_{m_i m_i m_i m_i}$ is

the nonlinear coefficient for the *i*-th mode, n_0 is the accumulated optical noise, N_s is number of spans, G is the amplifier gain, NF is the noise figure of amplifier, h is Planck constant, υ is the light frequency, B is the overall optical bandwidth, and h_e is noise enhancement factor given by Eq.(36) in ref. [20]. Derivation of Eq.(2.57) is shown in ref.[20] using Eq.(31), (36), and (40) from the reference.

2.2.2 Measurement of the Fibre Nonlinear Coefficients for LP_{01} and LP_{11} Modes

We construct an experimental setup to measure the nonlinear coefficient of LP_{11} and LP_{01} modes by means of using degenerate FWM products where frequency *i* and *j* in Eq. (2.54) are identical. The LP_{01} (or LP_{11}) nonlinear coefficient is measured by launching two optical pumps in LP_{01} (or LP_{11}) mode. As shown in Figure 2.7, two tuneable ECL lasers are separately amplified, and launched into a free-space mode coupling systems consisted of two collimator input ports, free-space combiner, and collimator output port that is connected to the input of a customized TMF fibre with detailed parameters shown in Table 1. To generate two LP_{11} modes, two long period fibre grating (LPFG) based mode converters are used to convert LP_{01} to LP_{11} [28]. We choose TMF of 10 meters and 50 meters for the measurement. The reason of utilizing short fibre is to improve the stability and repeatability. With the increase of fibre length, the spatial mode patterns become hard to maintain due to any mechanical disturbance, making it difficult to identify different nonlinear products. As a result, we use 10 meters and 50 meters TMF in this chapter. The disadvantage of shorter fibre is reduced FWM product. Nevertheless, we manage to generate FWM products with these fibres at least 10 dB above the sensitivity floor of the optical spectrum analyser (OSA) used. The launch powers of two pumps into the TMF are between 14 to 16 dBm, producing FWM of between -50 to -80 dBm, depending on launched wavelengths and modes. At the output of the TMF fibre, the right-side FWM product is filtered before fed into OSA for power measurement to avoid dynamic range limitation of OSA. For LP_{11} FWM products measurement, a free-space coupler is used to couple LP_{11} mode into LP_{11}-to-LP_{01} mode converter. The loss from the output fibre to the OSA is measured and used to calibrate

the data obtained from the OSA.

Table 1. Parameters of the custom-designed two-mode fibre

Core Diameter	***Refractive Index Step***	***LP_{11} Mode Cutoff Wavelength***	***Differential Mode Delay (DMD)***
11.9 μm	5.4×10^{-3}	2323 nm	3.0 ns/km
Chromatic Dispersion (LP_{01})	***Chromatic Dispersion (LP_{11})***	***Fibre Loss***	
22.1 ps/nm/km	17 ps/nm/km	0.26 dB/km	

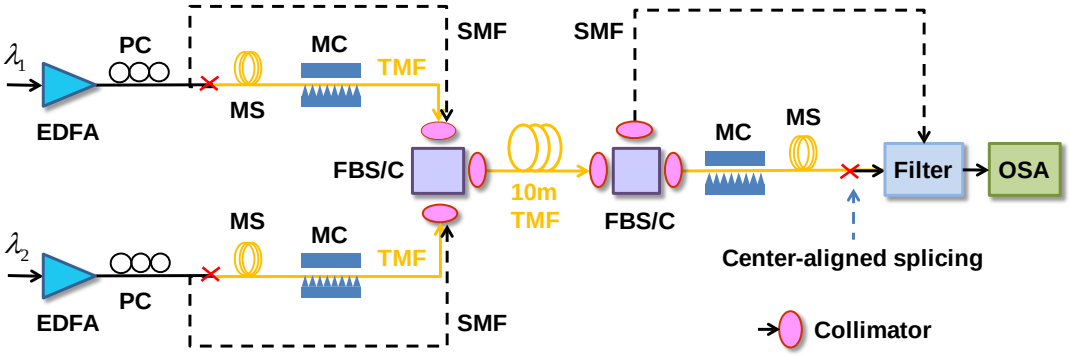

Figure 2.7. Experimental setup for fibre nonlinear coefficient measurement. PC: polarization controller; MS: mode stripper; MC: mode converter; FBS/C: free-space splitter/combiner; TMF: two-mode fibre; SMF: single-mode fibre; OSA: optical spectrum analyser.

Figure 2.7 shows the measurement of the FWM power after calibration as a function of the two pump wavelength spacing for both LP_{01} and LP_{11} nonlinear coefficient measurement. For LP_{11} mode, besides 10 meters TMF fibre, we also measured the nonlinear coefficient for fibre length of 50 meters. Insets show the spectra for LP_{01} and LP_{11} FWM products measured after a filter centred at the right-side FWM with residual pumps (λ_1, λ_2) and ASE noise. Theoretical simulation is also conducted using Eq. (2.54) with the following parameters based on our customized TMF fibre design: chromatic dispersion (CD) of 22.1 ps/nm/km for LP_{01} and 17 ps/nm/km for LP_{11}. Effective area (EA) is 94.7 μm^2 for LP_{01} and 99.9 μm^2 for LP_{11}. We have relatively good agreement of nonlinear coefficient of LP_{01} mode measured at 1.15/W/km, as opposed to theoretical 1.03/W/km. However, there is a big mismatch for LP_{11} nonlinear coefficient measured at 0.52/W/km for 10 m TMF measurement and

0.58/W/km for 50-m TMF measurement respectively, as opposed to the theoretical value of 0.98/W/km. We contribute the error of LP_{11} measurement to possible excitation of all the true modes, TE_{01}, TM_{01}, and two degenerated EH_{21} in the TMF, which degrades the overall FWM efficiency of LP_{11}. It is worth noting that we also measure FWM (i) between LP_{01} and LP_{11} modes, and (ii) between LP_{11}^{a} and LP_{11}^{b} modes. In the case (i), we find no measurable product confirming insignificant nonlinearity between LP_{01} and LP_{11} modes. In the case (ii), at 2-nm pump wavelength spacing, it is about 16 dB down

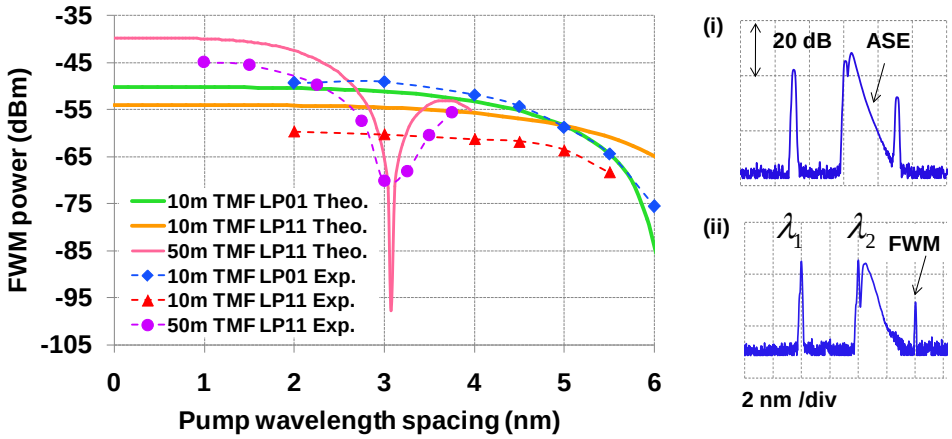

Figure 2.8. FWM product measurement. Inset: Spectra after filter centred at right-side FWM product for (i) LP_{01} and (ii) LP_{11} modes. Theo.; Theoretical results; Exp.: Experimental results.

below the FWM product between LP_{11}^{a} and LP_{11}^{a} modes. This verifies that the nonlinear interaction between LP_{11}^{a} and LP_{11}^{b} modes is also insignificant. We leave it to a future work to further improve the measurement accuracy of LP_{11} nonlinear coefficients by launching either true fibre modes or using even shorter TMF fibres.

2.2.3 Results and Discussion

Figure 2.9. Spectral efficiency (SE) for TMF systems. SE of SSMF is also drawn for comparison.

Figure 2.9 shows the numerical calculation of SE for TMF systems using Eq. (1). The span length is assumed to be 100 km, and the noise figure of optical amplifier is set to be 6 dB. The chromatic dispersion and nonlinear coefficients are as follows: CD is 22.1 (17) ps/nm/km for LP_{01} (LP_{11}). EA is 94.7 (99.9) μm^2 for LP_{01} (LP_{11}). These are the data based on the design and simulation of the customized TMF. Because of the CD and EA of LP_{01} are both larger than those of SSMF (CD of 17 ps/nm/km, fibre loss of 0.2 dB/km, EA of 80 μm^2), we expect a slight nonlinear enhancement of link capacity for TMF. The current fibre loss is measured at 0.26 dB/km in our TMF. However, there is an expectation that the loss for both modes should approach those of SSMF if properly designed. For the fibre loss of 0.26 dB/km using current design and for 10-span transmission, the capacity for TMF is 23.6 bit/s/Hz less than three times of 9.5 bit/s/Hz for SSMF. If we use 0.2 dB/km for the TMF fibre, the capacity is increased to 29.5 bit/s/Hz, slightly better than 3 times of that of SSMF. Similar ratio can be found with different number of spans. We conclude that although the three modes are densely packed and overlapped with each other, TMF fibre nonlinearity does not additionally decrease the SE. However, the fibre loss is a critical parameter for TMF to attain the full capacity of factor of 3 time SE enhancement compared to SSMF.

We note that by using short fibres, we are able to obtain accurate and repeatable measurement. However, this preference for using short fibres is only applicable to characterization of fibre nonlinearity. In practical transmission systems, long fibres

with mechanical disturbance can be readily accommodated by using electronic multiple input multiple output (MIMO) digital signal processing (DSP) [31-33]. The MIMO technique in FMF systems is able to equalize the modal coupling during fibre transmission, similarly to polarization-division multiplexed (PDM) SMF systems where the mechanical disturbance is not problematic.

2.3 Conclusions

In this chapter, we first derived closed-form analytical expressions for nonlinear system performance for densely spaced CO-OFDM systems via SMF transmission. The closed-form solutions include the results for the achievable Q factor, optimum launch power density, and nonlinear threshold of launch power density, as well as information spectral efficiency limit. These analytical results clearly identify their dependence on system parameters including fibre dispersion, number of spans, dispersion compensation ratio, and overall bandwidth. The closed-form solution is further substantiated by numerical simulations using distributed nonlinear Schrödinger equation.

We then show some preliminary study on information capacity of densely spaced CO-OFDM transmission via TMF. We have measured fibre nonlinear Kerr coefficient and presented discussion of system capacity for two-mode fibre. The system capacity approaches 3 times of that of single-mode fibre even though there is strong spatial overlapping between the modes in TMF. The future work on TMF nonlinear coefficients measurement and channel capacity analysis will be improving the measurement accuracy of LP_{11} nonlinear coefficients by launching either true fibre modes or using even shorter TMF fibres.

The derived closed-form equations in this chapter can be applied to both CO-OFDM systems and single carrier (SC) systems in dispersion uncompensated systems. The reason is that in dispersion uncompensated systems, both OFDM and SC systems exhibit high PAPR during transmission, which makes these two system possess similar nonlinear transmission performance. This observation has been confirmed by the works from other groups [34].

Chapter 3 Fibre Nonlinearity Mitigation for CO-OFDM

Following the discussion on the information capacity limits in the presence of fibre nonlinearity for CO-OFDM transmission in Chapter 2, we focus on nonlinearity mitigation for CO-OFDM systems in this chapter. Though it has been demonstrated that CO-OFDM transmission is promising to support single channel transmission with a data rate beyond 100 Gb/s [9, 11, 35, 36] for its high spectral efficiency and dispersion resilience, CO-OFDM has drawbacks of high peak-to-average power ratio (PAPR) which results in excessive nonlinear noise. As a result, it is of significant importance to mitigate the nonlinearity for CO-OFDM transmission. In this chapter, two approaches of nonlinearity mitigation will be discussed including (i) DFT-spread OFDM, and (ii) mid-link digital phase conjugation. Principle of each mitigation algorithm will be given, and the algorithm will be verified by experiments.

3.1 DFT-Spread CO-OFDM for Fibre Nonlinearity Mitigation

There is a common belief that the high PAPR of optical OFDM signals causes excessive nonlinear noise during fibre transmission [14]. Recently, discrete-Fourier-transform spread OFDM (DFT-S OFDM) was proposed as an attractive alternative to conventional CO-OFDM that possesses low PAPR within each OFDM sub-band [37]. The superior nonlinear performance of DFT-spread (DFT-S) OFDM is predicted by simulation in comparison with conventional OFDM [40]. In this section, we experimentally verify the nonlinear performance advantage of DFT-S OFDM systems over conventional OFDM systems [38]. Densely-spaced 8×55.1-Gb/s DFT-S OFDM channels are successfully received after 1120-km transmission with a spectral efficiency of 3.5 b/s/Hz [38]. We adopt a novel approach of consecutive transmission for both DFT-S OFDM and conventional OFDM signals, enabling stable and repeatable comparison between these two formats. It is shown that DFT-S OFDM

has an advantage of about 1dB in Q factor and 1 dB in launch power over conventional OFDM. Additionally, unique word (UW) aided phase estimation algorithm is proposed and demonstrated which enables extremely long OFDM symbol transmission and subsequently improves the spectral efficiency [38].

3.1.1 Principle of Unique-word (UW) DFT-S OFDM

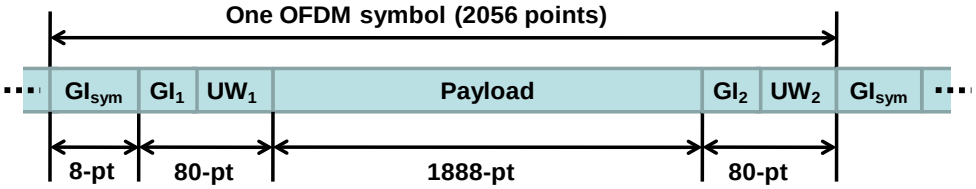

Figure 3.1. Structure of one DFT-S OFDM symbol. UW: Unique Word; GI: Guard Interval; pt: Point.

The concept of unique-word and its application were proposed for single carrier frequency-domain equalization (SC/FDE) [39]. Aided by the known UWs, better synchronization, channel estimation, and carrier phase estimation can be achieved for UW based systems compared with CP based counterparts [40, 41].

Figure 3.1 illustrates the UW OFDM symbol structure for one of the two polarizations. The UWs are periodically inserted in the data sequence. In this chapter, we choose the length of one DFT-S OFDM symbol to be 2048 points, including two 64-point UW patterns at two ends. Each 64-point UW pattern is cyclically extended by 16 points as shown in Figure 3.1 (where GI_1 and GI_2 are 16-point GIs for UW_1 and UW_2, respectively.), which results in an 80-point UW pattern at each side of OFDM symbol. An optional 8-point GI (GI_{sym}) is appended at the start of the OFDM symbol, which is a copy of the last 8-point of UW_2. The purpose of this optional 8-point is to keep data symbol length the same as training symbols. This GI is needed for training symbols so that no extra interpolation is required when calculating channel matrix. But it is only optional for data symbols and thus can be dropped for data symbols without affecting any performance. The total length of one DFT-S OFDM symbol is 2056 points. We use Zadoff-Chu sequence as UW patterns, for its flat frequency-domain response and constant time-domain amplitude [42]. The Zadoff-Chu sequence is generated by the following equation

$$x(n) = e^{-j\frac{\pi n^2}{N_{zc}}} \ (0 \le n \le N_{zc} - 1) \tag{3.1}$$

where $x(n)$ is the Zadoff-Chu sequence, and N_{zc} is the sequence length. We adopt block-based decision-feedback (DF) phase estimation given by [43-46]

$$\langle \phi_i \rangle = \frac{1}{K} \sum_{j=1}^{K} \arg\left(A_{ij} A_{ij}^{0*} \right) \left(1 \le i \le M \ / \ K \right) \tag{3.2}$$

where $\langle\ \rangle$ represents ensemble average, ϕ_i represents the carrier phase estimated for the *i*-th segment, A_{ij} and A_{ij}^0 are respectively received and transmitted *j*-th point in the *i*-th block of a OFDM symbol, *M* is the OFDM symbol length, and *K* is the block length for phase estimation. A_{ij}^0 can be replaced with the recovered (or sliced) data after symbol decision on the received symbols when the transmitted symbols are not known. The procedure of UW-based DF phase estimation is as follows: the first block for the phase estimation in each OFDM symbol is calculated within the UW, where the transmitted symbols A_{ij}^0 are known. The constellation of the second block will be de-rotated using the phase estimated from the first block given by

$$A_{ij}' = A_{ij} e^{-j\langle \phi_{i-1} \rangle} \ \left(i = 2, 1 \le j \le K \right) \tag{3.3}$$

where A_{ij} and A_{ij}' are the *j*-th point in the *i*-th block of a OFDM symbol before and after phase compensation, respectively. After constellation de-rotation, the symbol decision will be made to the phase compensated symbols A_{ij}'. Then another iteration of phase estimation and compensation will be made by applying Eqs. (3.2) and (3.3) (for arbitrary *i*), which will be subsequently passed to the following block. The propagation will continue until the end of payload blocks. It is noted that the phase estimation can also be performed using UW_2 and propagate the phase estimation backward. In this section, we use *K* of 16 if not otherwise mentioned.

A similar OFDM symbol structure to that shown in Figure 3.1 can be drawn for the second polarization by using different UWs. The reason to use two UWs within one OFDM symbol is compatibility with polarization diversity where the first and the

second UWs are orthogonal to each other when combining the two OFDM symbols for two polarizations in a Jones vector form. The two UWs for the two polarizations, $\begin{pmatrix} UW_{x1} \\ UW_{y1} \end{pmatrix}$ and $\begin{pmatrix} UW_{x2} \\ UW_{y2} \end{pmatrix}$ are given by

$$\begin{pmatrix} UW_{x1} \\ UW_{y1} \end{pmatrix} = \begin{pmatrix} UW \\ circshift(UW) \end{pmatrix}, \quad \begin{pmatrix} UW_{x2} \\ UW_{y2} \end{pmatrix} = \begin{pmatrix} -circshift(UW)* \\ UW* \end{pmatrix} \quad (3.4)$$

where $circshift()$ denotes a circular shift of the sequence by half of the sequence length and * denotes complex conjugate. The circular shift ensures that UWs for two polarizations, e.g., UW_{x1} and UW_{y1} are uncorrelated as long as the channel length is shorter than 16. Such configuration can aid fast synchronization and channel estimation (not explored in this section).

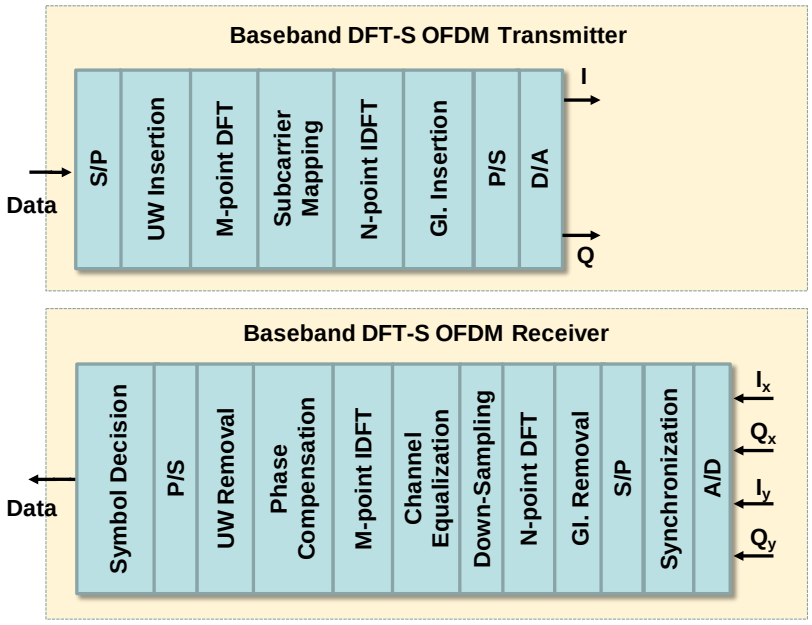

Figure 3.2. Configuration of baseband DFT-S OFDM transmitter and receiver; S/P (P/S): Serial-to-Parallel (Parallel-to-Serial) conversion; UW: Unique Word; GI: Guard-Interval; D/A (A/D): Digital-to-Analogue (Analogue-to-Digital) conversion.

UW aided phase estimation can be very effective in comparison with phase compensation method in conventional OFDM system. Since the phase estimation compensation is implemented in the time domain, it is possible to perform intra-symbol phase noise estimation rather than conventional symbol-wise phase estimation.

Additionally, because of known UWs are used to initiate phase estimation, the errors resulting from wrong symbol decisions do not propagate beyond one OFDM symbol.

Figure 3.2 shows the signal flow diagram for DFT-S OFDM transmitter and receiver. At the transmitter, after serial to parallel conversion, the UWs are added with data, and converted to frequency domain by applying a *M*-point DFT. The DFT spread signal is then mapped onto an *N*-point vector which is subsequently converted to a time-domain signal by IDFT. Typically *N* is an integral larger than *M*. In this work, we choose *M* of 2048 and N of 4096. The subcarrier mapping is a localized mapping [47], which means subcarriers are placed continuously and are occupying the centre part of the spectrum in this work. The guard-interval is inserted before digital-to-analogue conversion (DAC) to avoid inter-symbol interference. The comparison of RF spectra between DFT-S OFDM and conventional OFDM is shown in Figure 3.3. The spectra are plotted under the condition that two signals have exactly the same root mean square (RMS) value. For conventional OFDM signal, it uses 128-point FFT size. The reason we choose FFT size of conventional OFDM different from that of DFT-S OFDM signal is due to the phase noise. The conventional OFDM FFT size is limited by the phase noise and FFT of 128 is chosen. However, for DFT-S OFDM, the phase noise can be estimated in the time domain. After the IFFT at the receiver, the signal is transformed back to the time domain where a proper averaging window can be chosen for phase estimation. In this way, the FFT size is not limited by phase noise. As a result, the OFDM symbol length can be relatively large. Meanwhile, due to the use of 160-point UW, a long OFDM symbol is required to reduce the overhead. Consequently, we choose quite different sizes for DFT-S and conventional OFDM: FFT size of 4096-point for DFT-Spread, and 128 for conventional OFDM. From Figure 3.3, both signals have the same bandwidth and identical gap width in the middle to avoid impairment from DC. It can be seen that DFT-S OFDM signal has less power fluctuation and out-of-band leakage because it has much larger FFT size of 4096 than FFT size of 128 in conventional OFDM.

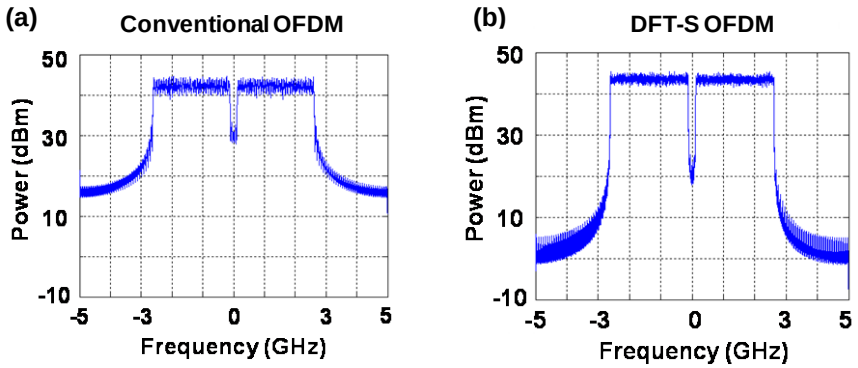

Figure 3.3. Baseband spectra for (a) conventional OFDM and (b) DFT-S OFDM.

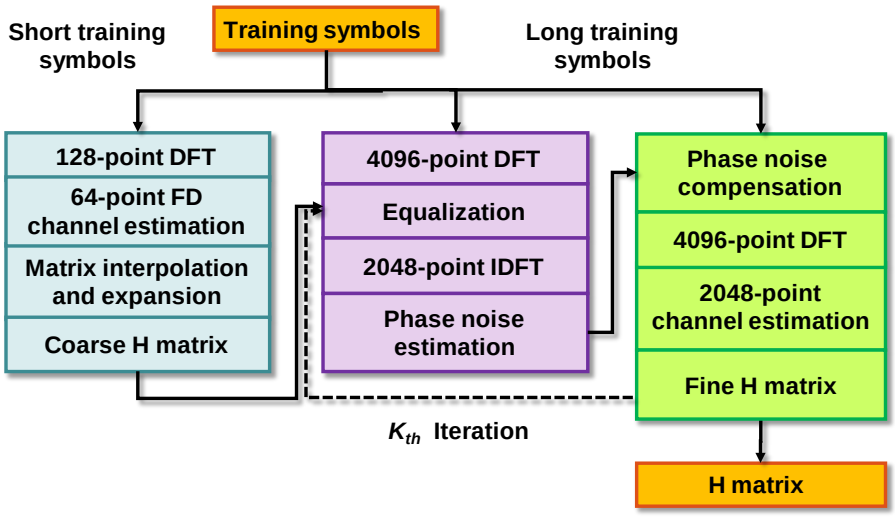

Figure 3.4. Flow diagram for channel estimation.

At the receiver, after the signal is down-converted to baseband, timing synchronization and serial-to-parallel conversion is made. Then the guard-interval is removed and a proper *N*-point window is selected to apply DFT. After the DFT, the frequency-domain signal is down-sampled and equalized with a one-tap equalizer. We use a hybrid of short and long training symbols for channel estimation. Only 2 short training symbols and 2 long training symbols are used in this work. The short and long training symbols consist of 128- and 4096-point Zadoff-Chu sequence respectively. Figure 3.4 shows the detailed channel estimation procedure: the first step is to calculate a coarse channel matrix (or *H* matrix) by using short training symbols. This coarse channel matrix will be interpolated and then expanded to the same length as long

symbols. The next step is to perform frequency-domain equalization to the long symbols by using coarse *H* matrix. The equalized long symbols are further transformed back to time domain to estimate intra-symbol phase noise. This estimated phase noise is then used to apply phase compensation on the original long training symbols. After the phase noise compensation, the conventional maximum-likelihood channel estimation can be performed to obtain the updated *H* matrix [43]. The same process can be repeated for a few times until an accurate *H* matrix can be obtained. In this work, no iteration is used since it is found that a single round of channel estimation is sufficient. After the frequency-domain equalization, *M*-point IDFT is applied to the equalized signal to rewind the DFT spreading at the transmitter. The UWs are employed to seed the DF aided phase estimation and compensation as described previously. Finally, symbol decision is made to the phase compensated OFDM symbols.

The nonlinear advantage of multi-band DFT-S OFDM has been theoretically analysed [37]. In multi-band DFT-S OFDM systems, each subband is essentially filled with a digitally-generated single-carrier signal. It has been shown that DFT spreading can significantly lower the PAPR for DFT-S OFDM compared with conventional OFDM [47]. For instance, DFT-S OFDM signal exceeds a PAPR of 7.5 dB for less than probability of 0.1 %, and this PAPR is 3.2 dB lower than the value in conventional OFDM with the same probability [47]. Furthermore, one of the important findings of DFT-OFDM for optical transmission is that there exists an optimal bandwidth which the subbands should be partitioned. The reason for this optimal bandwidth with respect to the nonlinearity performance is as follows [37, 48]: if in the case of small number of subbands, e.g., single carrier, the subband bandwidth becomes too broad. Although the PAPR within each subband is low at launch, due to large walk off among frequency components within each subband, the PAPR of each subband will grow rapidly thus inducing nonlinearity penalty; In the case of large number of subbands, the subband bandwidth becomes too narrow. Neighbouring subbands interact just as narrowly-spaced OFDM subcarriers, generating large inter-band nonlinear crosstalk and thereby large penalty due to narrow subband spacing. Subsequently there exists a sweet spot in number of subbands that gives the optimal nonlinearity performance. In

this experiment, each DFT-OFDM subband is 5 GHz, which is close to the optimal subband bandwidth predicted in [37].

Due to one extra DFT at the transmitter and one extra IDFT at the receiver, the complexity of digital signal processing (DSP) of DFT-S OFDM is higher than that of conventional OFDM. However, due to the improved nonlinearity tolerance, DFT-S OFDM may be a good choice where additional system margin is needed.

3.1.2 Experimental Results and Nonlinear Performance Analysis

The experimental setup is shown in Figure 3.5. At the transmitter, 8 CW lasers are combined and fed into an intensity modulator to impress 3 tones onto each wavelength. The tone spacing is controlled by the drive RF frequency at 5.3125-GHz, and wavelength spacing is set to be 16.4375-GHz. The optical signal is then split with a 3-dB coupler for separate modulation on the two polarizations. The OFDM signal for each individual band is generated by a Tektronix Arbitrary Waveform Generator (AWG). The time-domain OFDM waveform is first generated in a Matlab program with parameters as follows: total number of subcarriers is 4096 with 4-QAM encoding, guard interval is 16/4096 of the observation period, and middle 2145 subcarriers out of 4096 are filled, from which 160 subcarriers are occupied by UW patterns, and 97 subcarriers in the middle are left null to avoid contamination from DC. The real and imaginary parts of the OFDM waveforms are uploaded onto the AWG operated at 10-GS/s to generate two corresponding analog signals. The two polarization signals from the outputs of a 3-dB coupler are separately fed into two optical IQ modulators that are driven by the two AWGs. Consequently, the baseband OFDM signals are impressed onto all the 24 optical tones. The optical spectra of 8-lasers, 24-tones with and without data modulation are shown as insets. The spectra have flatness over 1.1nm bandwidth.

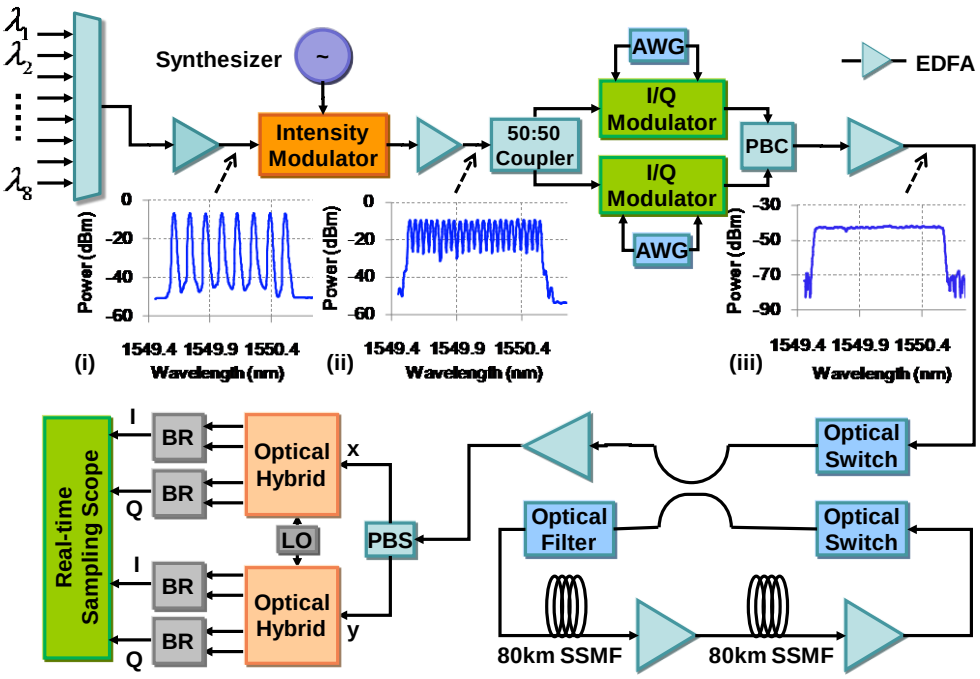

Figure 3.5. Experimental setup of 8x55.1-Gb/s DFT-S OFDM system. AWG: Arbitrary Waveform Generator; PBC: Polarization Beam Combiner; PBS: Polarization Beam Splitter; LO: Local Oscillator; BR: Balanced Receiver; The three insets are (i) measured optical spectrum of 8 wavelength lasers; (ii) Measured optical spectrum of (3x8) 24 tones; (iii) Measured optical spectrum of 24 bands after data modulation.

The optical outputs from two IQ modulators are combined with a polarization-beam combiner (PBC), forming a dual-polarization 8-channel DFT-S OFDM signal, with each channel carrying 55.1-Gb/s data. The signal is coupled into a recirculation loop for 1120-km transmission. The recirculation loop is consisted of two spans of 80-km SSMF fibre, with two EDFAs at the end of each span to compensate fibre loss. After transmission the signal is received with a polarization diversity coherent receiver. The RF signals from the coherent receiver are then input into a Tektronix real-time sampling scope at 50-GS/s, and processed with a Matlab program using a 2x2 MIMO-OFDM model. To achieve stable and repeatable comparison, DFT-S OFDM and conventional OFDM waveforms are cascaded in time domain digitally before loading onto AWG, with the same RMS value. Parameters for conventional OFDM signal are as follows: total number of subcarriers is 128 with 4-QAM encoding, guard interval is 1/8 of the

observation period, middle 67 subcarriers out of 128 are filled, and DF-based common phase error is calculated for phase estimation. 3 subcarriers close to DC are unfilled to avoid degraded performance due to DC. As such, the unfilled portion of the spectra are kept the same for both DFT-S and conventional OFDM.

Figure 3.6 shows an example of phase evolution over 16 DFT-S OFDM symbols (or about 6.5 μs). The phase noise within 12th symbol is shown in inset. It can be seen that due to the long symbol length, the phase can varies more than 0.6 rad within one OFDM symbol. It is obvious that the symbol-wise phase noise compensation is not suitable for extra long symbols. Thus it is necessary to introduce the UW-based time domain phase compensation.

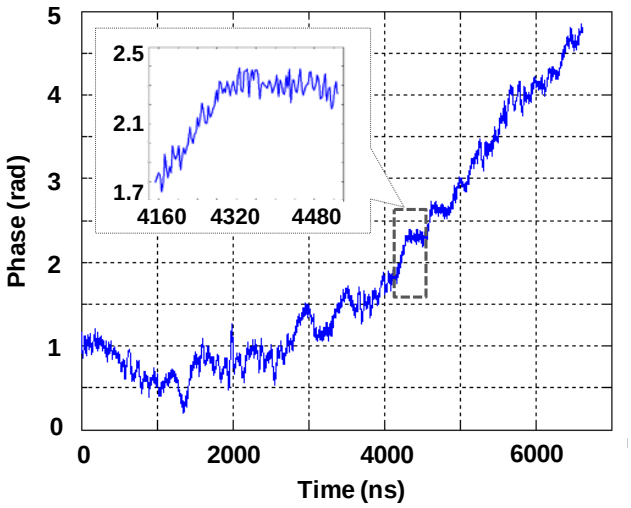

Figure 3.6. Phase evolution for the received DFT-S OFDM signal. The inset is the zoomed-in phase noise of 12th symbol.

Figure 3.7 gives the BER sensitivity of 18.4-Gb/s, 55.1-Gb/s, and 8×55.1-Gb/s signal at back-to-back for both DFT-S OFDM and conventional OFDM, which corresponds to one-band, three-band (or one wavelength), and 24-band (or 8 wavelengths) OFDM signals. For 18.4- and 55.1-Gb/s system, the BER is respectively measured over 1,208,320 and 3,624,960 bits. Figure 3.7 suggests that DFT-S OFDM and conventional OFDM have the same linear performance at back-to-back. The OSNR requirement for a BER of 10^{-3} is about 6-dB, 11-dB, and 21-dB for 18.4-Gb/s, 55.1-Gb/s, and 440.8-Gb/s system respectively.

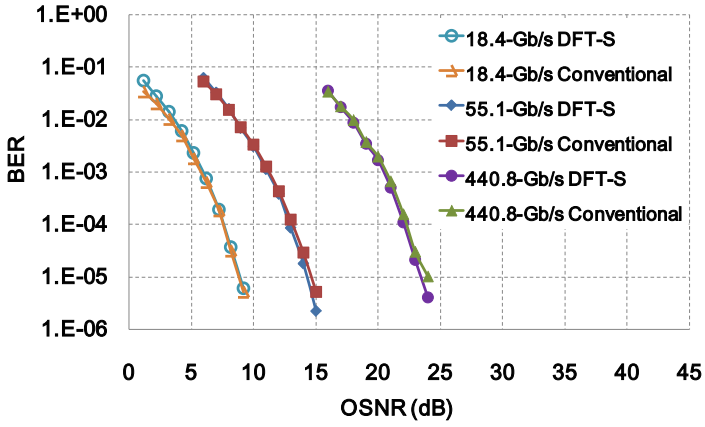

Figure 3.7. Bit Error Rate (BER) versus OSNR for 18.4-, 55.1- and 440.8-Gb/s DFT-S OFDM and conventional OFDM system at the back-to-back.

Figure 3.8 shows the nonlinear performance of both DFT-S OFDM signal and conventional OFDM signal for 440.8-Gb/s after 1120-km transmission. Figure 3.8(a) shows signal launch power vs. Q factor. It can be seen that DFT-S OFDM has a better nonlinear performance, with 1dB optimal Q factor improvement, and about 1 dB improvement in optimal launch power. The effectiveness of DFT-S OFDM system is more evident at high nonlinear region. For instance, at a launch power of 7 dBm or 8 dBm, the Q factor of DFT-S OFDM is improved by more than 2 dB. The constellations measured at a launch power of 7 dBm are shown as inset in Figure 3.8(a). It is evident that DFT-S OFDM has better performance after 1120-km transmission. To further isolate the nonlinear effect from the phase noise effect, we conduct signal processing by using phase estimation with block size *k* of 64. Since the conventional OFDM is also using phase estimation window of 64 points, the phase noise has the same impact on both DFT-S and conventional OFDM. The Q factor difference between DFT-S and conventional OFDM is shown in Figure 3.8(b) when both have the same phase estimation window size. As can be seen in the figure, when the launch power is higher than 1 dBm, with the increasing power level, the advantage of DFT-S OFDM increases, e.g., 2.8 dB at launch power of 8 dBm. Secondly, there is no observable difference if both OFDM formats use either 16 or 64-point phase estimation window. Therefore, the Q factor difference between these two formats in Figure 3.8(b) is clearly caused by

nonlinearity tolerance.

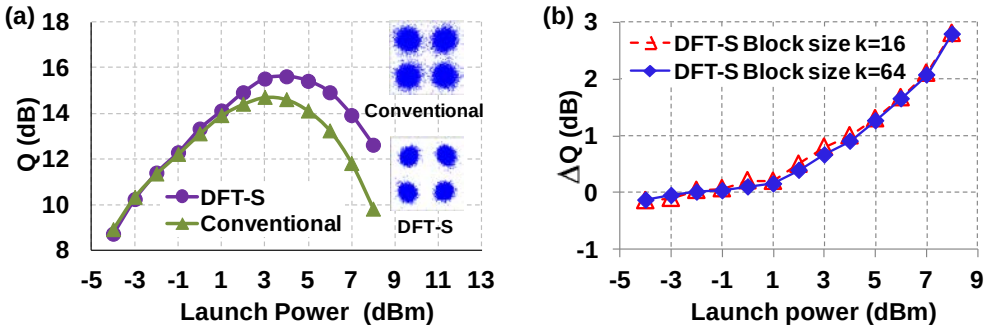

Figure 3.8. (a) Q factor vs. launch optical power for 440.8-Gb/s signal after 1120-km transmission. Insets are constellations for conventional and DFT-S OFDM signals. (b) Q factor difference between DFT-S OFDM signal and conventional OFDM when using the same phase estimation window size.

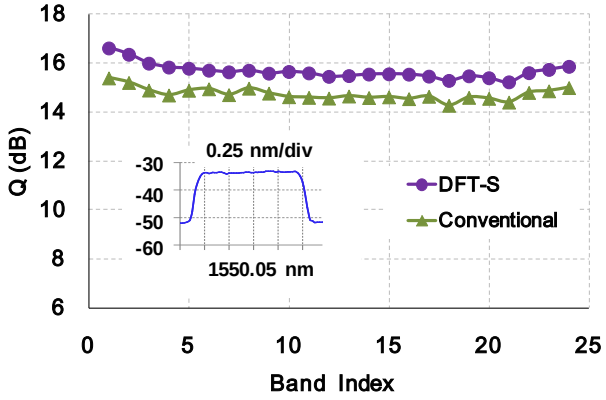

Figure 3.9. Q factor measurement for all the 24 bands after 1120-km transmission at the optimal launch power of 4 dBm. Inset is the measured received optical spectrum after 1120-km transmission.

We also measure performance after transmission for the 24 OFDM sub-bands of 8 lasers. The launch power is 4 dBm, which is the optimal power for 440.8-Gb/s DFT-S signal. The Q factors are shown in Figure 3.9. We can see that the advantages of DFT-S OFDM system have been preserved over all sub-bands, about 1 dB on average. It is noted that due to the middle portion of the spectrum is unfilled (Figure 3.3(b)), the DFT-OFDM signal in this work is not strictly a single-carrier one. Nevertheless, this demonstration shows not only this quasi-single-carrier format can be received properly

for long-haul transmission, but it also possess nonlinear advantages over the conventional OFDM. Additionally, because of the long OFDM symbol used, the overhead is reduced to below 10% as opposed to 20-25% in conventional CP based OFDM systems.

3.2 Nonlinearity Mitigation by Means of Mid-link Digital Phase Conjugation

The algorithm and signal processing discussed in section 3.1 is a method especially designed for CO-OFDM transmission. Essentially, we can also employ some universal techniques that are proposed for nonlinearity mitigation of general optical transmission including both single carrier and multi-carrier systems [49-52]. Among these techniques, Digital backward propagation (DBP) has drawn much attention for its flexible and comprehensive compensation of both intra- and inter- channel nonlinear effects [49]; Mid-link optical phase conjugation (OPC) [50, 53], also known as spectral inversion, inverts the spectrum by using four-wave-mixing (FWM), all-optically compensating both dispersion and fibre nonlinear effects. Although both methods show their capability in fibre nonlinearity compensation, DBP suffers from high computational complexity whereas OPC involves complicated nonlinear processes and doubles the optical spectrum occupation. One of the candidates which provide spectral inversion with low complexity is electrical phase conjugation (EPC) [52]. EPC deals with analogue signals and inverts spectra in electrical domain.

In this section, we propose digital phase conjugation (DPC) to realize phase conjugation with simple digital signal processing and offer the capability to compensate for implementation penalties such as time delay mismatch, bandwidth limitation, and frequency offset [54]. Furthermore, we experimentally demonstrate the use of DPC to improve the nonlinear transmission performance of a CO-OFDM signal. A single-channel 40-Gb/s 16-QAM polarization division multiplexed (PDM) CO-OFDM signal is successfully received after 10,400-km ultra-large area fibre (ULAF) transmission with mid-link digital phase conjugation at an FEC threshold of 1.8×10^{-2}

(Q^2 = 6.4 dB). The experimental results show 4-dB improvement of power tolerance, and 53% extension of transmission length compared with those without DPC [54].

3.2.1 Principle of DPC and Experimental Setup

The DPC is essentially a spectral inversion implemented in the electrical domain using digital signal processing. At mid-link, the signal is down-converted to the digital electrical domain by analogue-to-digital converters (ADC). The digitized signal is conjugated and converted back to the analogue domain using digital-to-analogue converters (DAC). After conjugation, the signal is up-converted to the optical domain using an optical modulator. The DPC enables fibre nonlinearity and chromatic dispersion compensation with low processing complexity. Compared with all-optical phase conjugation, DPC saves optical spectrum utilization by avoiding spectrum width doubling. Compared with EPC, DPC is capable of compensating for implementation penalties such as time delay mismatch, bandwidth limitation, and frequency offset between the transmitter laser and the optical local oscillator (OLO). DPC also provides the flexibility to perform digital filtering to optimize spectrum utilization when needed. Compared to a conventional optical-electronic-optical (OEO) repeater, mid-span DPC not only requires much less digital signal processing (DSP) load by not needing digital dispersion compensation and forward-error correction (FEC), but also reduces the DSP complexity of the receiver at the destination, since digital dispersion compensation is no longer required. For instance, for a 25-Gbaud signal transmitting over a 5000-km ULAF link, a conventional coherent receiver needs to compensate ~100000 ps/nm worth of dispersion, which requires a large equalizer with a tap size on the order of 1000 [55].

Figure 3.10 shows the experimental configuration of a 10,400-km CO-OFDM transmission with mid-link DPC. At the transmitter, the OFDM waveform was generated by an offline program (shown in inset (i) of Figure 3.10). Four drive patterns were stored in two synchronized arbitrary waveform generators (AWGs), each having two 10-GS/s DACs. Pseudo-random bit sequences (PRBS) of length 2^{15}-1 were used as the payload data. The IFFT size used for OFDM was 128, and a guard-interval (GI) of 2

samples was added between adjacent OFDM symbols, resulting in a small GI-overhead of 1.56%. Each polarization component of an OFDM symbol contained 79 16-QAM data subcarriers (SCs), 3 pilot SCs, one unfilled DC SC, and 45 unfilled edge SCs. The spectral bandwidth of the modulated signal was 6.48 GHz (=83/128×10GHz). Three correlated dual-polarization training symbols (TSs) [56] were used for every 697 payload OFDM symbols, resulting in a small TS-overhead of 0.43%. Assuming using 19.5% overhead hard-decision FEC limit [57], a BER of 1.84×10^{-2} (a Q^2 of 6.4 dB) was shown to be correctable to a BER better than 1×10^{-15}. Excluding the FEC overhead, the net payload data rate of the OFDM signal was 40 Gb/s (=10GHz×8b/s/Hz×79/130×697/700/1.195).

The four outputs of the AWGs were fed into a polarization-diversity nested Mach-Zehnder modulator. The signal was then launched into a recirculating loop to propagate over the first half of the link (5,200 km). The loop was consisted of four spans of 100-km ULAF. The fibre loss of 0.185 dB/km was compensated by backward Raman amplification. The nonlinearity coefficient of the ULAF was 0.81 $W^{-1}km^{-1}$. An optical filter was inserted into the loop to prevent the accumulation of out-of-band ASE noise. After the first half of the link, the signal was converted into the digital electrical domain and processed as described previously. The processed waveforms were then re-loaded to AWGs and converted to the optical domain for the second half (5,200 km) of the transmission link. This process is shown as a dashed line and inset (ii) in Figure 3.10. After 10,400-km (2×5,200-km) transmission, the signal was received by a coherent receiver and offline DSP was conducted to recover the signal. The key digital signal processing steps are shown as inset (iii) in Figure 3.10. Note that when mid-link DPC was not applied, digital dispersion compensation was additionally used in the receiver DSP [56].

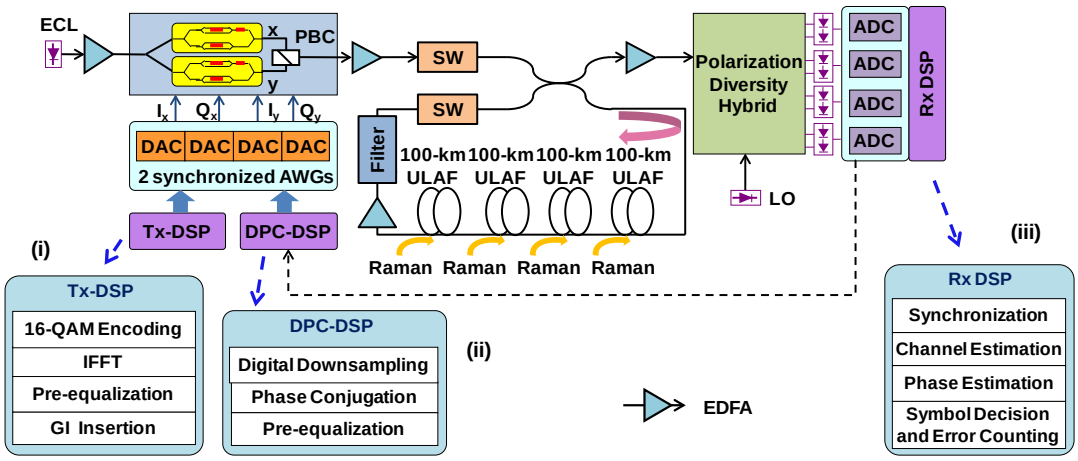

Figure 3.10. Schematic of the experimental setup for nonlinearity compensation using DPC. ECL: External cavity laser, PBC: Polarization beam combiner, SW: optical switch, LO: local oscillator, ULAF: Ultra-large-area fibre, AWG: Arbitrary waveform generator, DAC/ADC: Digital-to-analogue (analogue-to-digital) converter, DSP: Digital signal processing, Insets: (i) DSP of OFDM transmitter, (ii) DSP of mid-link processing, and (iii) DSP of receiver offline processing.

3.2.2 Results and Discussion

Figure 3.11 shows the experimental results of 10,400-km transmission, reported as a Q^2 factor derived from BER measurements. The solid circles show the transmission results without DPC. The signal launch power was -3 dBm, the optimal launch power for mid-link DPC transmission. At the FEC threshold of 6.4 dB, the signal can reach a transmission distance of 4,000 km. In the case of DPC (solid diamonds), the signal is conjugated at mid-link. It is evident that in the first half of the link, the Q factor drops with increase of distance due to accumulation of both ASE noise and fibre nonlinear noise. Remarkably, after mid-link conjugation, the Q factor begins to increase with the increase of distance until distance reaches ~10,000 km, as nonlinear effects are partially cancelled due to phase conjugation. At a transmission distance of 10,400 km, the Q factor is improved by 4.1 dB. By comparing the constellations of transmission with or without DPC (inset (i) and (ii) in Figure 3.11), it is evident that the performance is greatly improved due to the compensation of fibre nonlinearity by the mid-link DPC. It is interesting to note that the maximum Q factor is reached at 10,000 km rather than

10,400 km, at which the distance of the second half of the link equals that of the first half. This suggests that there is some asymmetry in the transmission link, e. g., an asymmetry of power distribution along propagation. After 10,400 km, the Q factor begins to decline quickly since excessive nonlinearity and noise start to degrade the performance.

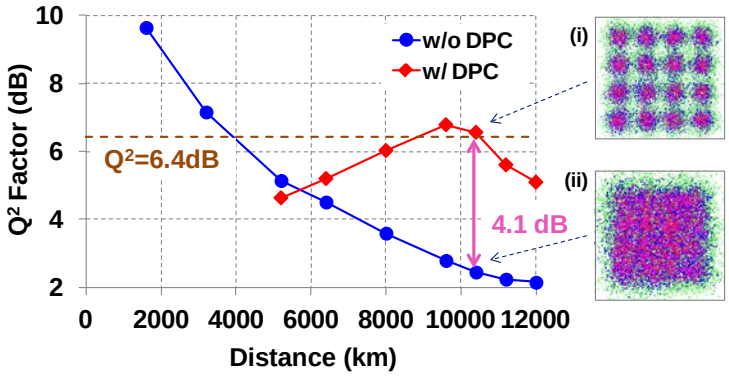

Figure 3.11. Q factor versus transmission distance with and without DPC. Inset (i): Recovered signal constellation after 10,400-km transmission with DPC; (ii) Recovered signal constellation after 10,400-km transmission without DPC.

In order to understand the nonlinear performance of the mid-link conjugated system, we measured the Q factor as a function of the launch power. Figure 3.12(a) illustrates three scenarios of transmission. The solid triangles and diamonds show transmission without DPC for a reach of 6,800 and 10,400 km respectively. These two curves suggest that without DPC, the optimal launch power is -7 dBm for both distances. For an FEC threshold of 6.4 dB, the maximum transmission length without DPC is 6,800 km. When employing DPC, since part of the fibre nonlinearity is mitigated, the optimal launch power increases to -3 dBm (4-dB power tolerance improvement), and the transmission distance increases to 10,040 km, which extends the distance by 53% compared to transmission without DPC. The optimal launch power is increased because nonlinear effects are partially compensated after spectral inversion, then the system becomes mostly OSNR limited. Furthermore, the maximum Q factor with DPC is increased by 1.3 dB compared with no DPC after 10,400 km.

Since the mid-link ADC/DACs introduce extra digitization noise, to identify the

degradation, we measured the back-to-back performance with or without DPC. In the case of DPC back-to-back performance, the signal was received, conjugated, reloaded to the AWGs, and then received again by a coherent receiver. The BER measurements are shown in Figure 3.12(b). By comparing the two curves, it can be seen that the digitization obviously increases the noise floor of the 16-QAM OFDM signal. However, at the FEC threshold of 1.8×10^{-2}, the penalty from the extra digitization step is less than 0.5 dB.

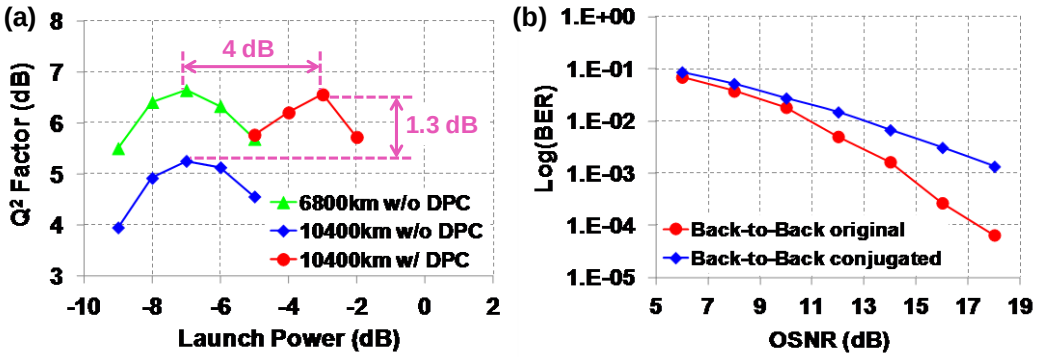

Figure 3.12. (a) Q factor versus launch power for different reaches, with or without DPC respectively. (b) Back-to-Back BER performance with and without digital phase conjugation.

3.3 Conclusions

In this chapter, we have demonstrated two approaches for fibre nonlinearity mitigation in CO-OFDM transmission including DFT-S OFDM and mid-link digital phase conjugation.

We have shown the first experimental verification of nonlinear performance advantage of DFT-S OFDM systems over conventional OFDM systems. Densely spaced 8×55.1-Gb/s DFT-S OFDM channels are successfully received after 1120-km transmission with a spectral efficiency of 3.5 b/s/Hz. We adopt a novel approach of consecutive transmission of DFT-S-OFDM and conventional OFDM enabling stable and repeatable measurements. It is shown that DFT-S OFDM has advantage of about 1 dB in Q factor and 1 dB in launch power over conventional OFDM. Additionally, unique word (UW) aided phase estimation algorithm is proposed and demonstrated

which enables extremely long OFDM symbol transmission.

We have also demonstrated single-channel 40-Gb/s PDM CO-OFDM-16QAM transmission over 10,400-km ULAF by mid-link digital phase conjugation, showing a power-tolerance improvement of 4 dB and a reach extension of over 50% for this high-level modulation format. Together with its high DSP efficiency, mid-link digital phase conjugation could be a promising candidate for future ultra-long-haul point-to-point transmission systems. This digital phase conjugation scheme is not limited to CO-OFDM systems, and can be extended to single carrier systems.

Chapter 4 Phase Noise Monitoring for High Spectral Efficiency CO-OFDM Transmission

Laser phase noise has been one of the hot research topics in coherent optical communications since late 1980s [58]. Due to the recent resurgence of the coherent optical communications in long-haul transmission, the study of the laser phase noise impact on transmission systems has attracted even more interests [59]. As we learn from Chapter 2 and Chapter 3, coherent optical OFDM (CO-OFDM) has drawn significant attention from the optical communication community and is a potential candidate for long-haul 100-Gb/s to 1-Tb/s Ethernet transport. However, it is well-known that OFDM is more susceptible to phase noise than coherent single-carrier systems [59]. Therefore, it is important to control and monitor the laser phase noise in high spectrum-efficiency CO-OFDM systems. Meanwhile, in recent years, the embedded digital signal processing (DSP) in coherent optical receivers have been employed to monitor the performance of the optical links [60-62]. It has been shown that OSNR, chromatic dispersion, Q and polarization mode dispersion (PMD) can be effectively monitored [60-62]. In this chapter, we provide a systematic study of phase noise monitoring in coherent systems.

4.1 Analysis of Differential Phase-error Variance for Filtered Phase Noise

One of the challenges of phase noise monitoring is that it is contaminated by many other noise sources such as white amplified-spontaneous-emission (ASE) source, fibre nonlinearity, and 1/*f* flicker noise [58]. Subsequently it is desirable to monitor the laser linewidths free from the influence of ASE, nonlinearity and 1/*f* flicker noise. In this section, we derive a closed-form expression for differential phase error variance for the phase noise averaged over a finite time window [63, 64]. A method of laser linewidth characterization and monitoring is proposed in presence of additive white noise

including ASE and nonlinear phase noise applicable to both single-carrier and multi-carrier systems [63, 64]. The algorithm is substantiated by experiments of coherent optical OFDM transmission over 960-km SSMF fibre. Additionally, we propose and demonstrate the use of an arbitrary waveform generator (AWG) to emulate the lasers with various linewidths, which can be useful to systematically study the laser phase noise impact. The significance of laser phase monitoring aided by embedded electronic DSP is that the potential fault from the laser phase noise can be isolated and identified [63, 64].

One of the widely used qualities to characterize the phase noise is differential phase error variance defined as [58]

$$\sigma_{\phi}^{2}(T) = \left\langle \left\{ \phi(t) - \phi(t-T) \right\}^{2} \right\rangle \tag{4.1}$$

where $\langle\ \rangle$ stands for ensemble average, $\phi(t)$ is the laser phase noise, and T is the relative delay. If the laser phase noise is a pure Wiener noise, or random walk noise, and is unfiltered, the relationship between phase error variance and 3-dB laser linewidth is given by [58, 65].

$$\begin{aligned} \sigma_{\phi}^{2}(T) &= 2\pi f_{3dB} T \\ or \quad f_{3dB} &= \sigma_{\phi}^{2}(T) / 2\pi T \end{aligned} \tag{4.2}$$

where f_{3dB} is the 3-dB width of the Lorentzian shape present in the spectral power density of the laser source with a pure Wiener phase noise. Therefore for the unfiltered Wiener noise, the 3-dB laser linewidth f_{3dB} can be estimated by computing the differential phase error variance normalized to 2π times the delay.

However in practical systems, the phase noise is not usually measured at each instantaneous of time. In OFDM systems, the phase noise is estimated over an entire OFDM symbol and the phase noise at each sampling point is not available [7]. In single-carrier systems, even though the phase noise at each sampling point can be obtained, it is rather noisy, and it is averaged over an appropriate time window for accuracy [66]. We thereby consider the phase noise that is averaged over a block of time as filtered phase noise. As a result, a closed-form expression different than (4.2)

ought to be derived to consider the phase noise filtering effect.

The phase-error variance can be generally expressed as [58]

$$\sigma_\phi^2(T)=4\int_{f_l}^{f_u} S_F(f)\frac{\sin^2(\pi fT)}{f^2}df \tag{4.3}$$

where $S_F(f)$ is single-sided frequency noise spectral density of the instantaneous frequency, which is related to phase noise density according to formula $S_F(f)=f^2S_\phi(f)$. T is the relative delay, f_l and f_u are the lower and higher integration bound which are related to symbol duration and signal bandwidth respectively.

In order to obtain a closed-form expression for $\sigma_\phi^2(T)$, we change the integration range to a more manageable form as follows

$$\sigma_\phi^2(T)=4\int_{0}^{\infty} S_F(f)\frac{\sin^2(\pi fT)}{f^2}df \tag{4.4}$$

In essence, we have set f_i to zero and f_u to infinity. It can be justified as follows: normally the signal to be studied is relatively long compared to the block time over which the noise is being averaged. We use an example of a signal trace with 100,000 samples at 10 GS/s. The duration is thus 10 μs. Therefore f_l equals to 100 kHz, and f_u equals to the signal bandwidth of 5 GHz.

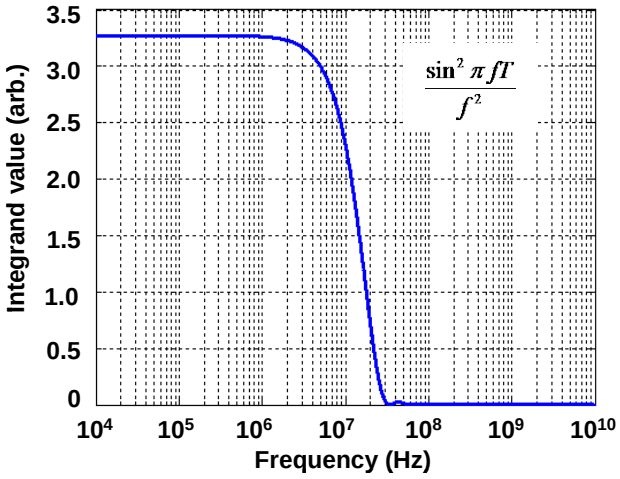

Figure 4.1. Integrand value of noise variance versus the frequency

Figure 4.1 shows the graph of function $\frac{\sin^2(\pi fT)}{f^2}$ with T of 14.4 ns (which corresponds to the averaging window length in subsequent simulations and experiments, the duration of an OFDM symbol). Assuming that $\phi(t)$ is Wiener noise, its frequency noise spectral density $S_F(f)$ thus equals to f_{3dB}/π [58], which is a constant over frequency. Therefore the plot in Fig.1 corresponds to the integrand value of Eq. (4.4). From Figure 4.1, one can conclude it is reasonable to change the integration range to $[0,\infty]$. This is because the integration from 0 Hz to 100 kHz contributes less than 1% of overall value. Meanwhile, for higher bound, because the function value drops quickly to zero after 100MHz, there is insignificant difference in changing it from 5 GHz to infinity.

We now denote $\tilde{\phi}(t)$ as the phase noise averaged over a moving window of T_s, and subsequently $\tilde{\phi}(t)$ can be expressed as

$$\tilde{\phi}(t) = \frac{1}{T_s}\int_0^{T_s} \phi(t-\tau)d\tau \tag{4.5}$$

Equation (4.5) shows that the single-sided frequency noise density for the filtered phase noise $\tilde{\phi}(t)$ is given by

$$\begin{aligned}\tilde{S}_F(f) &= S_F(f)\left|\frac{1}{T_s}\int_0^{T_s} e^{-j2\pi f\tau}d\tau\right|^2 \\ &= S_F(f)\frac{1}{\pi^2 T_s^{\,2}}\frac{\sin^2(\pi T_s f)}{f^2}\end{aligned} \tag{4.6}$$

It follows from (4.6) that the frequency noise spectral density of the averaged phase noise is essentially the original one filtered by a low-pass filter. The filter can be expressed as $\frac{1}{\pi^2 T_s^{\,2}}\frac{\sin^2(\pi T_s f)}{f^2}$. Since frequency noise spectral density $S_F(f)$ is considered as a constant, by substituting (4.6) into (4.4) we have

$$\sigma_{\Phi_0}^2(T) = \frac{4f_{3dB}}{\pi^3 T_s^2}\int_0^\infty \frac{\sin^2(\pi T_s f)}{f^2}\frac{\sin^2(\pi T f)}{f^2}df \qquad (4.7)$$

(4.7) can be integrated into a closed-form expression as

$$\begin{aligned}\sigma_{\Phi_0}^2(T) &= \begin{cases}\frac{2\pi f_{3dB}}{3}(3T - T_s), & T \ge T_s\\ \frac{2\pi f_{3dB}}{3}(3T_s - T), & T < T_s\end{cases}\\ &= \begin{cases}\frac{2\pi f_{3dB}T_s}{3}(3k-1), & T \ge T_s\\ \frac{2\pi f_{3dB}T_s}{3}(3-k), & T < T_s\end{cases}\\ k &\equiv T / T_s\end{aligned} \qquad (4.8)$$

where k is the ratio between the delay and averaging window length. The result in (4.8) is valid for both single-carrier and multi-carrier systems when the phase noise is averaged across a time window of T_s. For most practical cases, we assume that $T \ge T_s$, or, the delay time of the phase error variance is chosen to be no less than the averaging window period. It can be seen from (4.8) that the effect of the averaging reduces the phase error variance by an amount proportional to the window size T_s. Namely, the filtering effect depends on the length of averaging window rather than the relative delay.

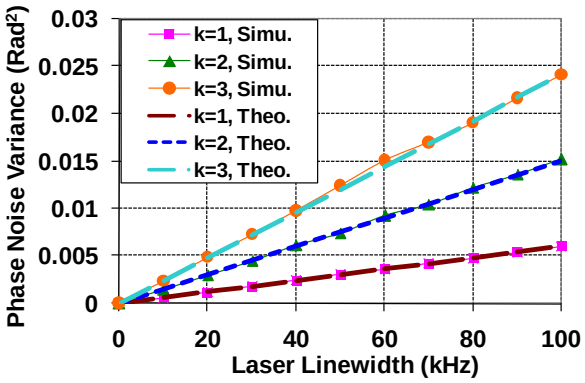

Figure 4.2. Differential phase noise variance as a function of laser linewidth with varying delay time.

We conduct numerical simulations to verify the result in (4.8). We generate lasers

with varying digital phase noise from 0 to 100 kHz. For the laser at each linewidth, the phase noise is averaged over a window of 14.4 ns. We calculate the differential phase error variance with the delay time normalized to the window size of 14.4 ns. Figure 4.2 shows the simulation results of the phase error variance using three different delays. For all the three delays, the simulation results match the theoretical ones very well.

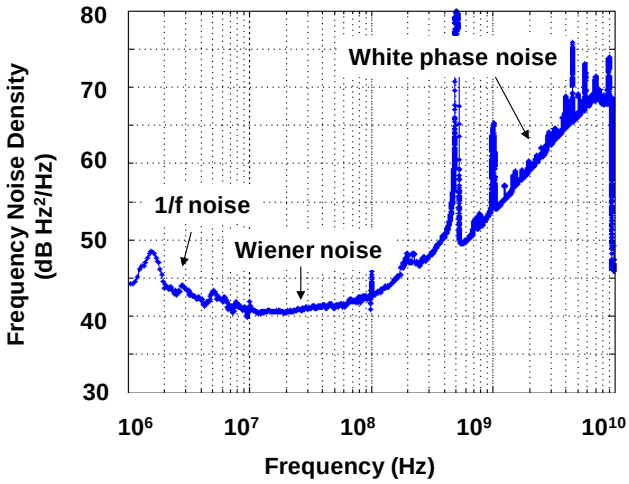

Figure 4.3. Frequency noise spectrum of the lasers without signal modulation.

We then conduct experiment to further verify the formula(4.8). We first measure the laser phase noise without any signal modulation by beating local oscillator (LO) and signal lasers using a standard complex coherent receiver (only one polarization) [67]. The laser phase noise can be computed directly from the phase of the complex field value [67]. $S_F(f)$ can be also computed. Figure 4.3 shows the combined frequency noise density spectrum for transmitter and receiver lasers. It is interesting to note that the frequency noise is comprised of three components: 1/f noise, white frequency (Wiener) noise, and white phase noise. At the frequency range of 10 MHz to 100 MHz, white frequency noise is dominant at the level of about 41 dB Hz^2/Hz, the laser linewidth can be estimated by multiplying this value by π, which gives a value of about 40-kHz for laser linewidth (combination of source and local laser).

After the original laser linewidth is obtained, in order to study the laser phase noise systemically, we adjust the laser linewidth digitally by adding phase noise to a known

waveform given by

$$s'(t) = s(t) \cdot e^{j\phi(t)} \tag{4.9}$$

$$\phi(t) = 2\pi\Delta t f_d n_t + \phi(t - t_0) \tag{4.10}$$

where $s'(t)$ and $s(t)$ is respectively the digital time-domain signal with and without digitally added phase noise $\phi(t)$, n_t is a Gaussian random variable with zero mean and variance of 1, f_d is the added laser linewidth, and Δt is the sampling time step.

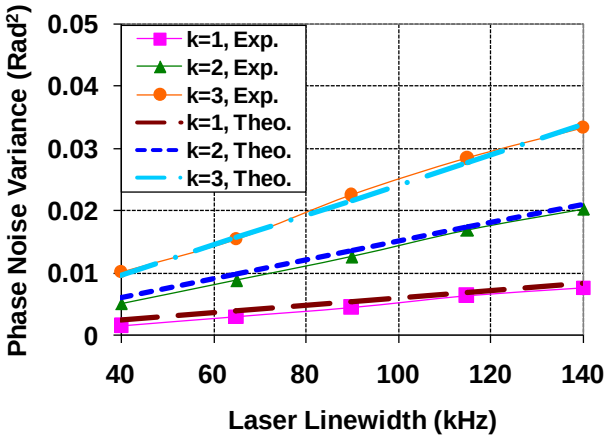

Figure 4.4. Differential phase noise variance as a function of laser linewidth with varying delay time. Both experimental and theoretical results are shown. Exp.: Experiment; Theo.: Theory.

In the experiment, we chose $s(t)$ as a 1-GHz tone which is digitally generated with an AWG. The 1-GHz RF tone is fed to an I/Q modulator, up-converted to an optical tone, and then detected by a coherent receiver. The output of the coherent receiver is captured by a real-time sampling scope. Similar to the simulation work described previously, the measured laser phase noise is averaged over a window of 14.4 ns. The differential phase error variance is calculated with the delay time normalized to the window size. Again (4.8) is used to compute laser linewidths theoretically. Both theoretical and experimental results are shown in Figure 4.4. From Figure 4.4, it can be seen that the closed-form expression of differential phase error variance in Eq.(4.8) closely matches both simulation and experiments.

4.2 Characterization of Laser Linewidths in Coherent Optical OFDM Systems

In CO-OFDM systems, the common phase error (CPE) which represents the collective rotation of one OFDM symbol is given by [7]

$$\Phi_i = \sum_{m=1}^{N} \phi_i(m)/N \tag{4.11}$$

where Φ_i is the CPE of the *i*-th OFDM symbol, and $\phi_i(m)$ is the laser phase noise at the *m*-th sample in the *i*-th OFDM symbol. Since each OFDM symbol is spaced at the OFDM symbol period of T_s in time, it is very tempting to apply (4.2) using CPE as

$$\begin{aligned}\sigma_\Phi^2(k) &\equiv \left\langle \left(\Delta\Phi(k)\right)^2 \right\rangle = \left\langle \left(\Phi_i - \Phi_{i-k}\right)^2 \right\rangle \\ &= 2\pi k T_s f_{3dB}\end{aligned} \tag{4.12}$$

where $\Delta\Phi(k) \equiv \Phi_i - \Phi_{i-k}$ and *k* is OFDM symbol delay while computing the phase error variance. There are two potential problems associated with applying (4.2) while using CPE: (i) the phase noise is contaminated by other noise sources, and (ii) Φ_i is already averaged within the window of T_s. To illustrate the problem, we assume the laser phase noise is consisted of two sources, one is the intrinsic laser phase noise $\phi_0(t)$ such as Wiener noise and flicker noise, and the other is white additive noise $\phi_n(t)$ from optical ASE noise and fibre nonlinearity such as four-wave-mixing noise, namely

$$\phi(t) = \phi_0(t) + \phi_n(t) \tag{4.13}$$

Assuming the independence of the two noise sources and combining (4.1), (4.2), (4.11), and (4.13), we have

$$\sigma_\Phi^2(k) = \sigma_{\Phi_0}^2(k) + \sigma_{\Phi_n}^2(k) \tag{4.14}$$

It follows from (4.14) that when using the CPE to compute the laser phase error variance, it is contaminated by the white noise term of $\sigma_{\Phi_n}^2(k)$. Since ϕ_n is a white

noise, its differential phase error variance $\sigma_{\Phi_n}^2(k)$ should be independent of the two phase instances which used to compute the error as shown in (4.1). In other words, $\sigma_{\Phi_n}^2(k)$ should be independent of OFDM symbol delay *k*.

To avoid the influence from the white noise, we elect to compute the results with two different delays. Substituting (4.8) into (4.14), setting *k* to 1 and 2, we have

$$\sigma_{\Phi}^2(1) = \frac{2}{3}(2\pi f_{3dB} T_s) + n_0 \tag{4.15}$$

$$\sigma_{\Phi}^2(2) = \frac{5}{6}(4\pi f_{3dB} T_s) + n_0 \tag{4.16}$$

where $n_0 = \sigma_{\Phi_n}^2(k)$ is white noise variance independent of OFDM symbol delay k. The factor 2/3 and 5/6 are the scaling factors calculated from Eq. (4.8) which is attributed to the fact that the CPE is a filtered phase noise. The reason we chose k to be the two smallest values is to avoid the *1/f* noise effect as is well explained in [68]. Combining (4.15) and (4.16), we arrive at the expression of the laser linewidth given by

$$f_{3dB} = \left(\sigma_{\Phi}^2(2) - \sigma_{\Phi}^2(1)\right) \Big/ 2\pi T_s \tag{4.17}$$

The advantages of applying (4.17) is that the laser linewidth can be estimated from CPE variance $\sigma_{\Phi}^2(k)$ and the result is free from the white phase noise. Moreover, CPE is naturally available in OFDM signal processing and there is no need to alter the DSP algorithm for laser phase noise monitoring.

4.3 Experimental Demonstration of Laser Linewidth Monitoring in CO-OFDM Transmission Systems

We conduct experiments of phase noise monitoring based on a 107-Gb/s CO-OFDM system. As shown in Figure 4.5, the five-tone optical source spaced at 6.5625GHz is generated using two cascaded intensity modulators. The tone spacing and AWG sampling clock are locked through the 10-MHz frequency standard. The OFDM signal in each individual band is generated by a Tektronix Arbitrary Waveform Generator (AWG). The time domain OFDM waveform is first generated in a Matlab

program with the parameters as follows: total number of subcarriers is 128 with 4QAM

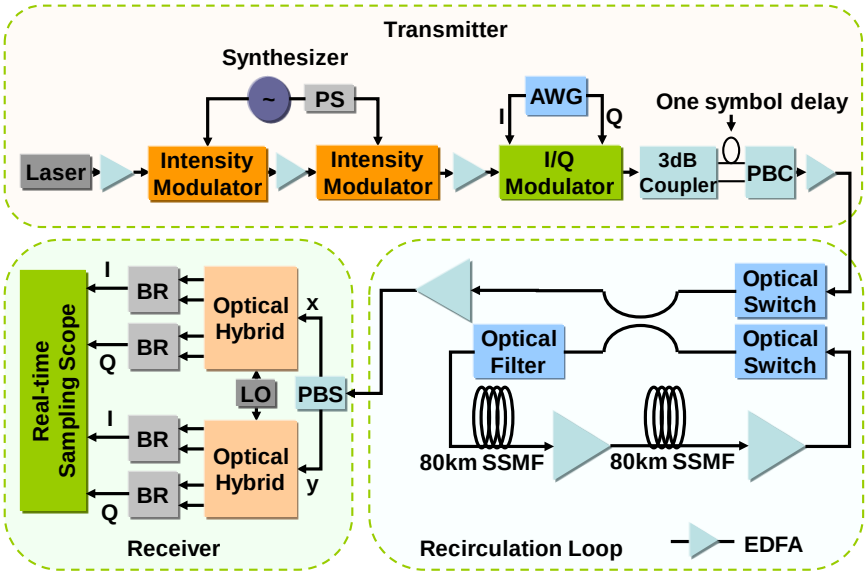

Figure 4.5. Experimental setup for phase noise monitoring in 107 Gb/s CO-OFDM systems. PS: Phase Shifter, AWG: Arbitrary Waveform Generator, PBC: Polarization Beam Combiner, PBS: Polarization Beam Splitter, BR: Balanced Receiver.

encoding, guard interval is 1/8 of the observation period, middle 80 subcarriers out of 128 are filled, from which 10 pilot subcarriers are used for phase estimation. The real and imaginary parts of the OFDM waveforms are uploaded into the AWG operated at 10 GS/s to generate two analogue signals, which are then fed into I and Q ports of an optical I/Q modulator to impress the baseband OFDM signal onto five optical tones. The optical output of the I/Q modulator consists of five-band orthogonal-band-multiplexed OFDM (OBM-OFDM) signals, with each band carrying 10.7-Gb/s data. The optical OFDM signal from the I/Q modulator is then split into two branches that are delay-mismatched by one OFDM symbol period (14.4 ns), and then combined using a polarizing beam combiner to obtain a polarization multiplexed signal. The signal with launch power of -1.5 dBm is further input into a recirculation loop comprised of 2 spans of 80-km fibre and two EDFAs to compensate the loss. The signal is coupled out from the loop after 6 circulations (960 km), and received with a polarization diversity coherent receiver on a per band basis. The RF signals are then input into a Tektronix real-time sampling scope at 50 GS/s, and processed with a

Matlab program using 2x2 MIMO OFDM models.

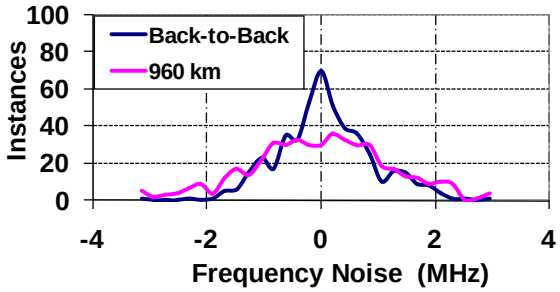

Figure 4.6. Frequency noise distribution for back-to-back and 960-km transmission.

Figure 4.6 shows the frequency noise distribution for a block of 500 OFDM symbols at the back-to-back and 960-km transmission. The frequency noise is obtained by using the formula of $\Delta f_i = \Delta\Phi_i / (2\pi T_s)$, where $\Delta\Phi_i$ is the variance of CPE Φ_i defined in (4.11). The frequency noise represents the CPE change per OFDM symbol normalized to $2\pi T_s$, which is essentially the frequency noise averaged over one OFDM symbol. Due to large white phase noise from ASE noise and fibre nonlinearity, the frequency noise after 960-km transmission is much more severe than back-to-back.

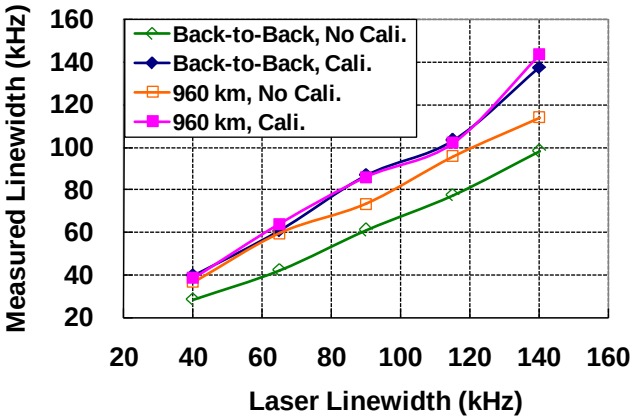

Figure 4.7. Estimated laser linewidths before and after calibration. Cali: Calibration

We adjust laser phase noise digitally in CO-OFDM system as described by (4.9).Laser linewidths of 0, 25, 50, 75, and 100 kHz are added to the original laser linewidth of 40 kHz producing lasers with 40, 65, 90, 115, and 140 kHz linewidths,

respectively. Figure 4.7 shows experimental results of back-to-back and transmission for both the proposed method using Eq.(4.17) (labelled as 'Cali.' for calibration) and the conventional method using (4.2) (labelled as 'No Cali.' for no calibration). We observe that when using conventional method, neither back-to-back results nor 960-km transmission matches the 'true' laser linewidths of 40, 65, 90, 115, and 140 kHz. Secondly, the laser linewidths estimated at the back-to-back using expression (4.2) is much smaller than that of 'true' laser linewidths, which can be attributed to the scaling coefficient as shown in (4.16). When using conventional approach, the laser linewidths estimated after transmission is much larger than at the back-to-back, which is mainly due to the ASE noise and nonlinearity added after 960-km transmission. In comparison, we also show in Figure 4.7 the laser linewidth monitoring using our proposed approach expressed in (4.17). Even after 960-km transmission with significant optical noise and nonlinearity introduced, the laser linewidths measured agree very well with the 'true' laser linewidths. Furthermore, both laser linewidths measured at the back-to-back and 960-km transmission agree with each other, using the approach we proposed in Eq.(4.17).

4.4 Conclusions

In this chapter, a closed-form expression of differential phase-error variance is presented. The phase noise is averaged over a finite time window, cancelling the effects of additive white noise. A method of laser linewidth characterization and monitoring is proposed in the presence of additive white noise applicable to both single-carrier and multi-carrier systems. Using the proposed method, laser linewidth can be extracted via embedded signal processing. Therefore the monitoring can be done in-service without interrupting data transmission. The method is further substantiated by experiments in a 107-Gb/s coherent optical OFDM system with 960-km transmission over SSMF fibre. A novel method of digitally adjusting laser linewidth is proposed and demonstrated which is useful to the systematic study of laser phase noise impacts.

Chapter 5 Enabling Spectrum-Efficient Transmission by Using TMF Fibres

It follows from previous chapters that that high spectral efficiency transmission can be readily achieved with the concept of CO-OFDM. In such systems, the CO-OFDM wavelength channels can be either continuously spaced without frequency guard band [8-10], or densely spaced with extremely small frequency guard band [11, 12]. These densely spaced systems present the ultimate limit of achieving high spectral efficiency by allowing very little or no frequency guard band. This capacity has been quickly approached by the recent demonstration within some practical engineering margin [5]. If we continue to stay with the SMF platform, it is not possible to enjoy the same dramatic capacity improvement in the future as in the past two decades. Therefore, space-division-multiplexing (SDM) is developed to overcome the capacity barrier. Generally, there are two main approaches at the moment for SDM: multi-core fibre (MCF) [26, 27, 69] based SDM systems and few-mode fibre (FMF) based SDM systems [28, 29, 32, 70, 71]. In this chapter, we perform the design and implementation of spectrally efficient CO-OFDM transmission by using FMF fibres. In particular, we propose (i) MIMO channel equalisation algorithm for mode-division multiplexed CO-OFDM superchannel and (ii) a design of mode-compatible optical add/drop multiplexer (OADM).

5.1 MIMO Channel Equalisation for Mode-division Multiplexed CO-OFDM Signals

Essentially, the MIMO processing for MDM CO-OFDM superchannel is similar to the digital signal processing (DSP) of its counterpart, namely, the single mode CO-OFDM signals. However, one of the problems we encounter is that in the FMF-based systems, there exist a variety of mechanisms inducing mode dependent loss (MDL), for instance, non-ideal mode multiplexing and de-multiplexing, and MDL of

the splices, couplers, and optical amplifiers. Excessive MDL results in significant system penalty [72, 73]. Therefore, various methods are proposed to improve the system performance by coupling and decoupling modes with low loss and low OSNR penalty using novel system components (low-loss mode coupler), or using carefully aligned mode multiplexer and demultiplexer [74, 75]. There was also report on performance improvement using delayed signals from additional receivers [75].

In this section, we introduce a systematic and detailed discussion on digital signal processing to improve receiver sensitivity by using larger receiver sets. In particular we demonstrate signal processing of 4x6 MIMO systems using 3 different channel equalization algorithms: zero-forcing (ZF), minimum-mean-square-error (MMSE), and successive interference cancellation (SIC). The results show that the receiver sensitivity can be improved respectively by 1.8, 2.9, and 4.9 dB for ZF, MMSE, and SIC equation in a 100-Gb/s 4x6 MIMO-OFDM systems [76].

5.1.1 Algorithms for TMF-based MIMO Channel Equalization

We now introduce the principle of the three equalization methods. We consider the MIMO channel with N transmitters and M receivers. The received signal can be expressed as

$$y_i^k = \sum_{j=1}^{N} H_{ij}^k x_j^k + n_i^k \quad (1 \le i \le M) \tag{5.1}$$

where H is the $M \times N$ channel matrix, y is the $M \times 1$ received signal, x is the $N \times 1$ transmitted signal, and n is the additive white Gaussian noise. The superscript k denotes the k-th OFDM subcarrier, subscript i denotes i-th receiver, and j denotes the j-th transmitter. For the reminder of the section, we shall omit the subcarrier index for brevity, implying that the signal processing is done on per-subcarrier basis.

There are a myriad of available techniques for channel equalization and estimation [77, 78]. We apply three well-developed algorithms in our FMF optical communication systems. They are ZF equalization, MMSE equalization, and SIC equalization.

(i) Zero-forcing (ZF)

The ZF equalizer applies the inverse of the channel frequency response to the

received signal, to remove the signal distortion. As the name suggests, ZF would completely remove the inter-modal-interference (IMI) if there were no noise. The ZF equalization utilizes general method of Pseudo-inverse of the MxN channel matrix, which is defined as

$$W = pinv(H) = \begin{cases} (H^H H)^{-1} H^H & if\ M > N \\ H^{-1} & if\ N = M \end{cases} \tag{5.2}$$

where $pinv(H)$ stands for Pesudo-inverse, the superscript H denotes Hermitian conjugation of a matrix. W is the channel equalization matrix, and the superscript '-1' represents the inverse of matrix. The estimated transmitted symbol, $\hat{x}$ is therefore given by

$$\hat{x} = W \cdot y \tag{5.3}$$

(ii) Minimum mean square error (MMSE)

The ZF equalizer removes all linear distortion, but amplifies noise greatly where the channel response has small amplitude due to fading. An improved equalizer for a noisy channel is the MMSE equalizer, which does not usually eliminate interference completely but instead minimizes the total power of the noise and the interference components. Formally, it is an approach that tries to find an equalization matrix W minimizing the criterion

$$E\left\{\left(W \cdot y - x\right)^H \left(W \cdot y - x\right)\right\} \tag{5.4}$$

where 'E' stands for ensemble average. Minimizing Eq. (5.4) yields

$$W = \left(H^H H + \frac{\delta_n^2}{\delta_s^2} I \right)^{-1} H^H \tag{5.5}$$

where δ_n^2 and δ_s^2 are respectively the variance for the noise and transmitted signal.

(iii) Successive interference cancellation (SIC)

The performance of the channel equalization can be further improved by having some prior knowledge of channel information, for instance, the strength of each mode. The interference from stronger modes to the weaker ones can be cancelled by recovering them early. The equalizer estimates and cancels the interference of

transmitted signal one by one, until all the transmitted signals have been processed. The estimation of transmitted waveform (the interference) is done by either ZF or MMSE equalization. In this work, we choose MMSE approach for its better performance compared with ZF equalization. Usually, the signal with higher SNR (e.g. $\hat{x}_j$) will be equalized and processed first using Eq.(5.5). The signal after cancelling the interference of the first (*j*-1) estimated modes is given by:

$$y' = y - H_{1:M,1:j-1}\hat{x}_{1:j-1} \tag{5.6}$$

where $H_{1:M,1:j-1}$ is the first (*j*-1) columns corresponding to the first (*j*-1) recovered modes $\hat{x}_{1:j-1}$. At the end of each iteration, the channel matrix shrinks to $M \times (N-p)$ for the *p*-th iteration. y' will be applied to Eq.(5.5) to recover the next mode. The iteration repeats until all the transmitted modes have been processed.

5.1.2 Experimental Results and Discussion

We conduct 4x6 back-to-back measurement for a 102 Gb/s TMF CO-OFDM system to verify the performance of the above mentioned three algorithms. As shown in Figure 5.1, the signal is created by combining 3 optical tones spaced at 6.5185 GHz. The 3 tones are fed into optical IQ modulator, which is driven by OFDM signal from arbitrary waveform generator (AWG). The polarization multiplexing is emulated by splitting the CO-OFDM signal from IQ modulator into two branches, which are delayed with each other by 1 OFDM symbol (500 ns), and recombined with a polarization beam combiner (PBC). We then emulate the signals for two orthogonal LP_{11} modes by splitting the signal and delaying one branch by 2 OFDM symbols (1 μs delay). Two pairs of long-period fibre grating (LPFG)-based mode converters (MC) and mode strippers (MS) are used to convert LP_{01} mode to LP_{11} mode. Free space mode combining and splitting is achieved with collimators and prism beam splitters (BS).

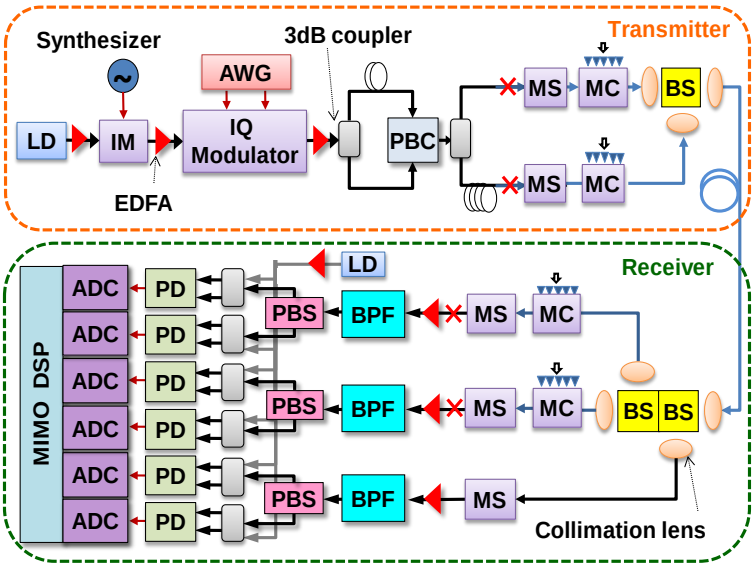

Figure 5.1. Experimental setup for 4x6 FMF MIMO CO-OFDM measurement. LD: Laser diode; IM: Intensity modulator; AWG: Arbitrary waveform generator; PBS/C: Polarization beam splitter/combiner; MS: Mode stripper, MC: Mode convertor; BS: (free-space) beam splitter; BPF: Band pass filter; PD: Photo diode; ADC: analogue-to-digital convertor.

The mode-division multiplexed signal is then sent to the receiver by a 7-meter TMF fibre. We employ two synchronized sampling scopes for coherent heterodyne detection. We use a narrow band pass filter (BPF) to remove the unwanted bands and keep an intermediate frequency gap between the LO and signal to avoid image folding. For 4x6 MIMO configuration, at the transmitter side, there are 4 transmitted signal (2 degenerate LP_{11} modes with each being polarization-division multiplexed), and at the receiver we implement 6 receivers to collect not only the 4 LP_{11} signals but also the 2 LP_{01} signals which is excited by the non-ideal coupling. In contrast, for 4x4 MIMO configuration, only the 4 LP_{11} signals are processed at the receiver. The OFDM parameters are: OFDM symbol length of 2560 points; cyclic prefix of 452 points; 4 OFDM training symbols employed to represent alternate launch of 4 combinations of polarizations and modes, which is used for 4x6 (or 4x4) channel matrix by means of intra-symbol averaging [79]; unique word length of 32 used at each end of OFDM symbol to seed phase estimation for data symbols [38]. The phase estimation of training symbols is done by using RF pilot [80]. The data symbols use DFT-spread (DFT-S)

OFDM signal, and the phase estimation of data symbol is done using decision feedback seeded by using unique word [38]. The CO-OFDM single channel occupies 19.5 GHz bandwidth, carrying a net data rate of 102 Gb/s.

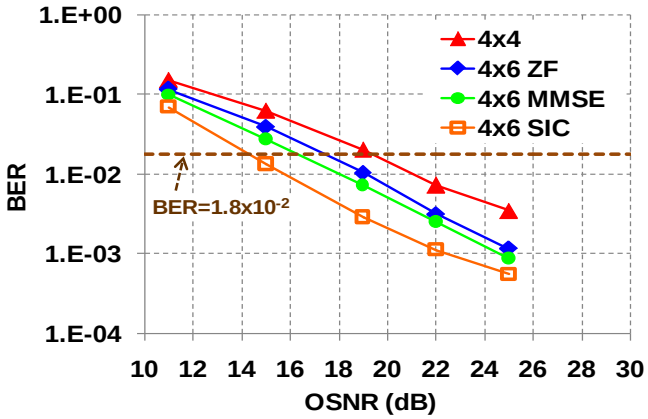

Figure 5.2. BER performance for 102-Gb/s CO-OFDM by using 4x4, 4x6 ZF, 4x6 MMSE, and 4x6 MMSE+SIC.

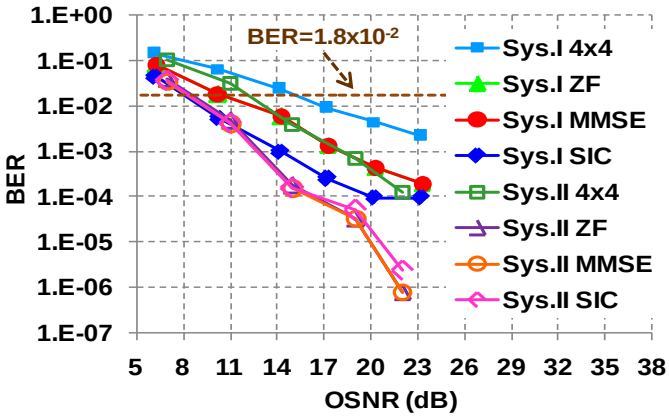

Figure 5.3. BER performance comparison between systems I and II of a 34-Gb/s CO-OFDM system. The MIMO size is 4x6 if not specified.

To study the effectiveness of the 4x6 MIMO equalization, and to verify how the algorithms can adapt the changing channel, we measured the CO-OFDM system under two different channel conditions: (i) the two LP_{11} modes are launched in non-orthogonal orientation to emulate non-ideal mode coupling, which is called system I, (ii) the two LP_{11} modes are launched in orthogonal orientation, which is called system II. Figure 5.2 shows the BER as a function of OSNR in system I, where the system suffers large penalty due to the non-ideal mode coupling. It can be seen that compared

with 4x4 configuration, the system sensitivity is improved by 1.8 dB, 2.9 dB, and 4.9 dB using equalization of 4x6 ZF, MMSE, and SIC respectively. All the three bands of the 102 Gb/s OFDM signal are measured and the average BER is plotted. There are 5,836,800 bits measured in total for each OSNR value. We consider OSNR penalty at FEC BER threshold of 1.8×10^{-2} for 19.5% overhead [57].

Figure 5.3 shows BER performance for comparison of systems I and II but with measurement of only 1 band of 34-Gb/s data. We point out a few instructive observations from Figure 5.3. When the channel condition is 'good' in system II, there is no obvious difference between the three algorithms. While the channel becomes 'bad' in system I, i.e., the channel matrix is badly skewed implying excessive MDL, there are significant disparity among the three methods. We conclude that although SIC provides the best performance, for the channel without severe fading, ZF is sufficient. Moreover, channel equalization using 4x6 to recover the non-ideal coupling (system I) is extremely effective, especially for SIC algorithm, the sensitivity difference between system I and system II are reduced from 2.8 dB to merely 0.2 dB after SIC equalization.

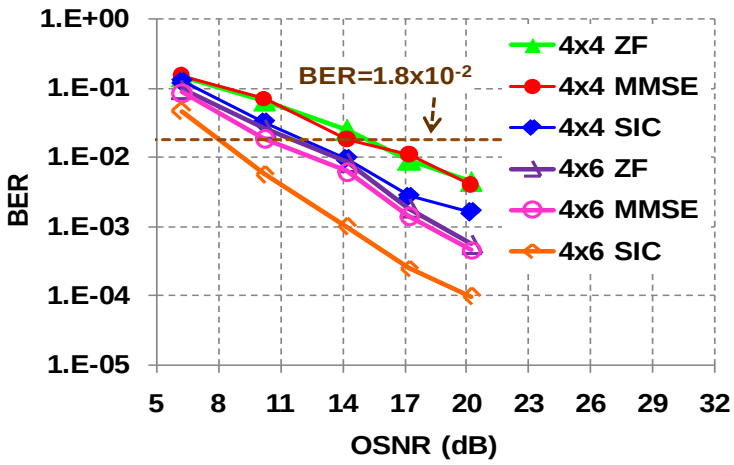

Figure 5.4. Comparison of 4x4 and 4x6 MIMO of 34-Gb/s CO-OFDM by using ZF, MMSE, and SIC.

To further confirm the sensitivity improvement from larger receiver sets, we also apply ZF, MMSE, and SIC to 4x4 CO-OFDM signals of system I. Both 4x4 and 4x6 MIMO results are plotted in Figure 5.4. The 4x4 ZF is the conventional 4x4 MIMO system which serves as the baseline of the comparison. By applying SIC to 4x4 signal,

the sensitivity can be improved by 1.1 dB. Increasing number of receivers from 4 to 6 improves the sensitivity by 3.8 dB for SIC equalization. In practice, this performance improvement should be justified against the increased cost of higher receiver complexity.

5.2 Mode-compatible OADM for High Spectrum Efficiency Optical Networking

So far, FMF compatible optical amplifiers based on Raman effect [81] and few-mode EDFA [82] have been reported. By using well-controlled pump modes, mode dependent gain variations can be minimized, opening the ways for long-haul FMF transmission. Similar to the trends in SMF-based optical networks, the capacity scaling in FMF systems will be achieved by wavelength-division multiplexing (WDM). In such systems, reconfigurable optical add-drop multiplexers (ROADM) that support all propagation modes will be a key element for realizing flexible networking. Although point-to-point WDM transmission over FMF has been demonstrated, the study of FMF-compatible ROADM has not been fully investigated.

In this section, we show that besides optical amplification, another element essential to high capacity optical network, the OADM can be greatly simplified in FMF-based systems compare with MCF systems. While in MCF systems, the optical signals in different cores are transmitted independently, in FMF-based ones the wavelength channels containing all the modes are processed as one entity. Thus, in FMF systems, all the modes can be optically added/dropped without mode demultiplexing/multiplexing during transmission. We call this wavelength channel containing few-mode tributaries the mode-division multiplexed (MDM) superchannel. In the future high-capacity few-mode fibre networks, the MDM channels will be wavelength-routed when traversing optical networks. The idea of such FMF-based systems is similar to that of polarization-multiplexed (PM) systems where the two polarizations are not separately processed during transmission. This greatly reduces the complexity of the system design while doubling the system capacity.

In this section, we show our design of an FMF-compatible OADM, which is an important first step towards FMF-compatible ROADMs. We demonstrate the reception of 3x318 Gb/s MDM superchannels CO-OFDM signals via the proposed OADM [83, 84]. The experimental results show that there are respectively 2.6, 2.4, 0.7 dB OSNR penalties for add, drop and through ports.

5.2.1 Single-mode OADM Technologies

There are a variety of technologies to realize SMF-based OADMs including thin film filters (TFF) [85], fibre Bragg gratings (FBGs) [86], integrated planar arrayed waveguide gratings (AWGs) [87], and liquid crystal on silicon (LCos) -based wavelength selective switches (WSS) [88]. Figure 5.5 illustrates the principles of these four technologies. As depicted in Figure 5.5(a), for a TTF- based OADM, collimation lens are used to launch light from optical fibre into a free space TFF with a specific angle of incident (AOI). The TFF acts as a band-pass filter in transmission mode and as a notch-filter in the reflection mode. The transmitted beam from the TFF is thus the dropped signal and will be collimated and coupled back into fibre. Meanwhile the reflected beam from the TFF combined with the light beam from ‘Add’ port is sent into the ‘Out’ port via another collimator. Such OADMs can be miniaturized and the number of input/output ports can be scaled up by using well-established technologies such as micro-electro-mechanical systems (MEMS) and LCoS [89]. Figure 5.5(b) shows FBG-based OADM architecture. This OADM is consisted of two three-port optical circulators and an FBG with central wavelength matching the add/drop channel, which will be dropped and added at the OADM. Figure 5.5(c) illustrates AWG based OADM. As shown in the exemplary configuration, the 2 NxN AWGs are respectively placed at the input and output as the wavelength de-multiplexer and multiplexer. The add/drop operation on a given wavelength channel can be obtained with a 2x2 switch. Finally, LCoS-based WSS is another commonly-used OADM for its high flexibility. As shown in Figure 5.5(d), a typical LCoS-based WSS comprises a conventional grating (usually an AWG), imaging optics, imaging mirror, LCoS array, and polarization diversity optics. The multiplexing and demultiplexing functionalities can be achieved by the

AWG, and the capability of switching can be also realized using either MEMS technology.

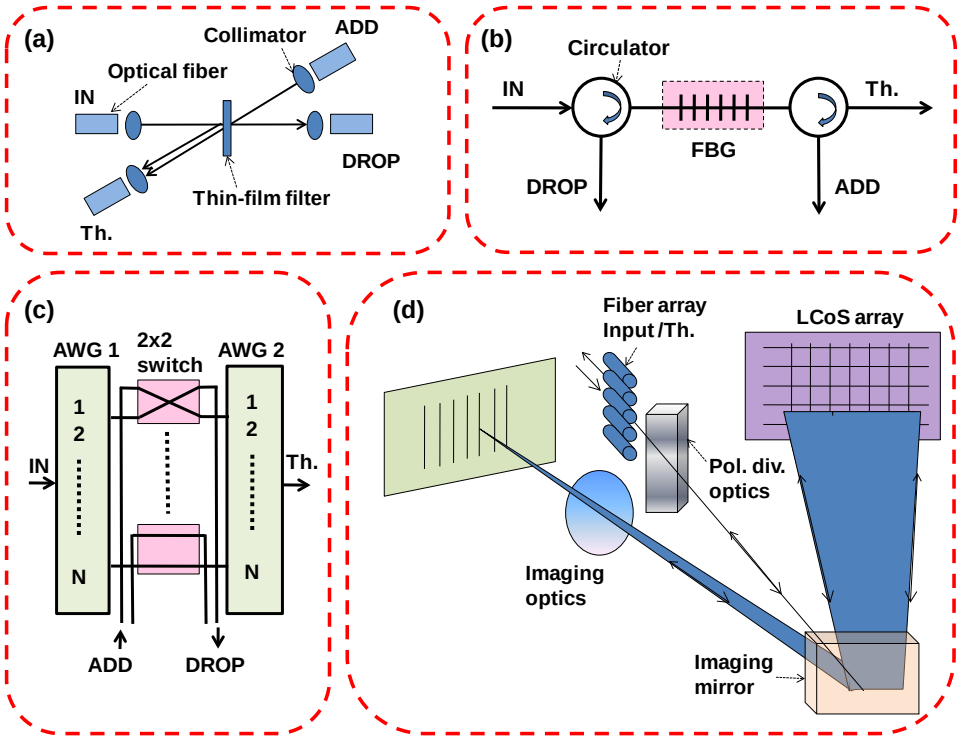

Figure 5.5. Schematic diagram of four different OADM technologies. (a) Thin-film filter approach; (b) FBG with optical circulators; (c) AWG; (d) wavelength selective switching. FBG: fibre Bragg gratings, AWG: arrayed waveguide gratings, Pol.: Polarization, div.: diversity, Th.: Through.

The major challenge in designing few-mode OADM is to achieve low modal and polarization dependence. We choose TFF-based OADM for the proof-of-principle demonstration. We will discuss the modal and polarization dependence in details in the following section.

5.2.2 Design of Few-mode Compatible OADM

The architecture of the TFF-based FMF compatible OADM can be similar to their SMF counterparts discussed in section 5.2.1. We consider that mode dependence of beam divergence angle in a FMF to be small for a practical implementation of OADM with free-space components. Since different modes have different mode field diameters (MFDs), after collimation the divergence of these two light beams will be different as well. The argument is that for our OADM the difference of the divergence between

LP_{01} and LP_{11} modes is small enough to ensure low mode-dependence transmission. This argument is reasonable since the beam divergence Θ can be calculated as $\Theta = D_m / f$, where D_m is the MFD and f is the focal length of collimators. We use collimators of 11-mm focal length, and the MFDs are 11.0 μm and 11.3 μm for LP_{01} mode and LP_{11} mode respectively. The above parameters give less than 0.06 degree difference in terms of divergence, which makes the transmission characteristics insensitive to different modes.

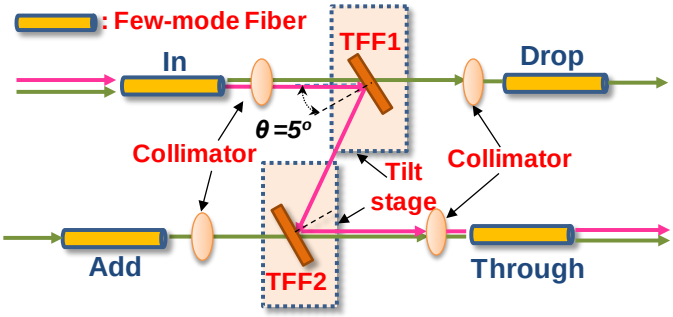

Figure 5.6. Schematic diagram of the few-mode compatible OADM.

We design and build a two-mode compatible free-space OADM using collimators and a pair of TFFs. Figure 5.6 shows the OADM architecture. As explained in 5.2.1, the TFFs act as band-pass filters in transmission mode and as notch-filters in the reflection mode. We use double reflection in order to sufficiently suppress the drop channel in output, which would otherwise serve as in-band crosstalk for the add channel. We tilt the TFFs by 5° in order to achieve lateral separation of the in/add and drop/through ports in the double reflection configuration. The 5° tilt launch also prevents any parasitic reflection from the drop or add ports from accumulating multiple reflections. The diameter of the free-space light beam is 2 mm.

In order to characterize the few-mode compatible OADM, we conduct measurement for the OADM using both LP_{11} modes and LP_{01} mode. First, we attach two-mode fibre (TMF) to the four ports (in, add, through, and drop) and use LP_{11} mode to measure the transmission characteristics. The LP_{11} mode (LP_{11a} or LP_{11b}) is generated by a conventional SMF transmitter, a long-period fibre grating (LPFG)-based mode converters (MC) [28, 33], and a mode stripper (MS). The generated LP_{11} mode is fed through a collimator lens, a prism, the other collimator lens, and then coupled to a

TMF fibre which is connected to an OADM. At the through and the drop ports of the OADM, the TMF fibre is directly attached to a multimode OSA to measure the spectrum. The transmission characteristics of the two LP_{11} modes measured by the OSA are shown in Figure 5.7. It can be seen from in-to-out transmission characteristics for both LP_{11a} and LP_{11b} that, the dropped channel (at the centre of the spectrum) is 25 dB below the through channel over a bandwidth of 0.5 nm. This ensures that the added signal will not be affected by in-band crosstalk. The loss for add, drop, and through channel are about 2.2, 2.1, 2.5 dB under the best operation condition, respectively. The add/drop transmission characteristics resembles a band-pass filter but with some ripples, which is caused by the beating between LP_{11} and residual LP_{01} modes. The residual LP_{01} can be attributed to many sources, such as imperfection of the mode converter, mode combiner, and even OADM. The transmission characteristics for LP_{01} mode of the OADM is also measured by removing the MC and MS and replacing TMF with SMF at each port. The LP_{01} mode is presented in Figure 5.7, showing much smooth transmission characteristics due to immunity from LP_{01} and LP_{11} beating. This point to the difficulty of characterizing FMF based devices such as OADM. In other words, two-port transmission characteristics should be represented by a 4x4 input to output matrix, with both inputs and outputs could be a choice from any two polarizations of any two LP_{11} modes. This poses a huge challenge to fully measure the FMF compatible devices in terms of measurement complexity and a need for high-precision mode multiplexing and de-multiplexing devices.

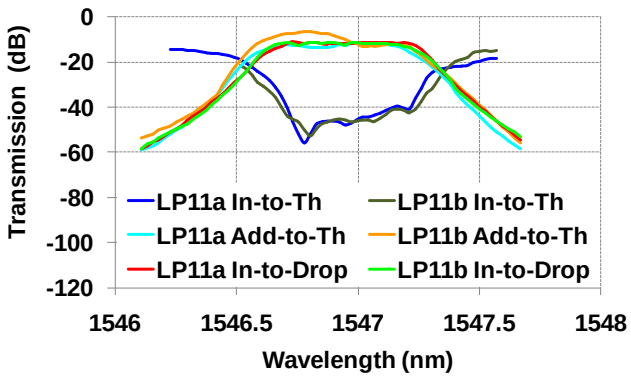

Figure 5.7. Measured transmission characteristics of the OADM based on TMF. Th: Through.

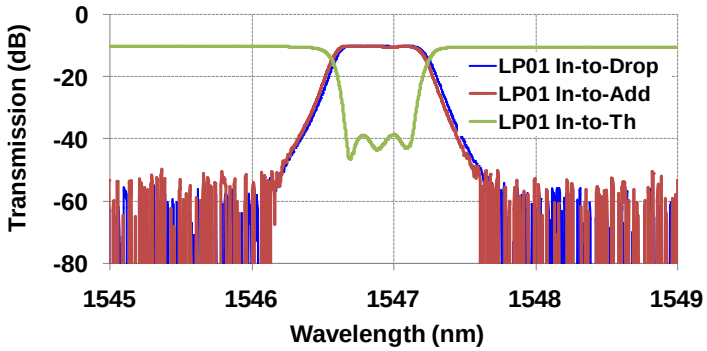

Figure 5.8. Measured transmission characteristics of the OADM based on SMF. Th: Through.

To identify the polarization dependence, we insert SMF based polarization controller before MC and MS. By rotating the polarization state, we find there is no observable change on the OSA. From this we conclude that the polarization dependence of this OADM is insignificant (< 0.2 dB). The reason for such negligible polarization dependence is that we utilize thin-film filter with an AOI as small as 5 degree.

5.2.3 Phase Estimation for Mode-Division Multiplexed CO-OFDM Signals

We here describe our revised RF-pilot aided phase estimation for the training symbols in our CO-OFDM signal processing. Since we use relatively long OFDM symbols (500 ns), before performing channel estimation, the phase noise in training symbols should be properly removed. One of the efficient phase estimation approaches for CO-OFDM is the RF-pilot tone aided estimation [80]. In such a scheme, a RF pilot tone is created for each OFDM symbol at the transmitter. At the receiver, this pilot tone is filtered out and the phase evolution can be extracted from the RF-pilot.

One of the problems associated with our 4x4 MIMO digital signal processing (DSP) is that, due to the random coupling among polarization and spatial modes, the RF pilots spread into all of the four modes (2 polarization- and 2 spatial-modes). For instance, in an extreme case, the RF pilot tone could be totally lost for one of the 4 modes. Therefore, instead of the conventional way of processing each mode separately, we process all the four modes jointly. Namely, we use the RF-pilot tones from all the

modes to perform the phase estimation. This would ensure reliable phase estimation, regardless how the coupling condition is among all the polarization and spatial modes.

We partition the OFDM symbol into N_{sym}/K blocks each containing K points. The estimated phase for the s-th block via RF-pilot tones is given by

$$\phi_s = \arg\left(\frac{1}{M} \frac{1}{K} \sum_{i=1}^{M} \sum_{j=1}^{K} A_{ij}^{s} A_{ij}^{1*} \right),\ s = 1, 2, ...N_{symbol} / K \quad (5.7)$$

Where N_{sym} is the OFDM symbol length, M is the number of modes, and A_{ij}^{s} represents the j-th point in the s-th block of the i-th mode, and '*' stands for complex conjugate. It follows from Eq. (5.7) that the estimated phase of each block is obtained by averaging the phase noise first within a block and then over the four modes. In this way, reliable and robust phase estimation can be achieved, regardless how the signal power distributes among the four modes.

Although this RF-pilot aided phase estimation method can be applied to data symbols as well, we employ unique-word aided phase estimation for the DFT-spread (DFT-S) OFDM signals for the data symbols [38].

5.2.4 Experimental Results and Discussion

We use 3 channels to measure add, drop, and through functionalities of our custom-designed OADM, with the centre channel to be dropped and added, and two side channels to pass through. Each channel contains a multiband CO-OFDM signal consisting of 9 densely-spaced bands. Figure 5.9 shows the experimental setup. The optical mode coupling from SMF to FMF and vice versa is achieved using two pairs of MS and MC. Free space mode combining and splitting is utilized with collimators and prism beam splitters (BS). There is an adjusting key assembled to each collimation port, to enable convenient adjustment of the orthogonality of the two LP_{11} patterns. Each channel is created by combining 3 external cavity lasers (ECLs), each carrying 3 tones spaced at 6.5185 GHz. Thus there are 9 tones in total for each channel. The frequency guard band between different lasers is 500 MHz. The 27 tones from 3 channels are

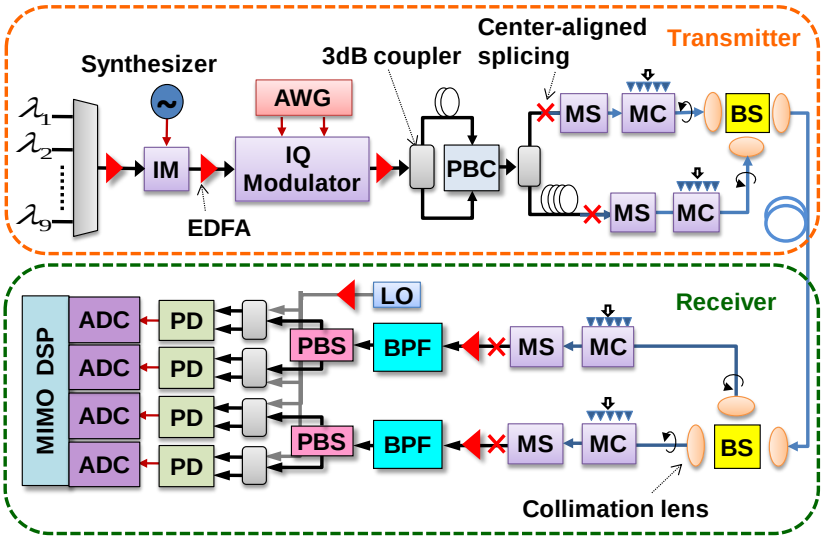

Figure 5.9. Experimental setup for TMF compatible OADM performance measurement. AWG: Arbitrary waveform generator, PBS: polarization beam splitter, MS/C: Mode stripper/converter, BS: Beam Splitter, BPF: Band-pass filter, PD: Photodiode, ADC: Analogue-to-digital converter, LO: local oscillator.

combined and fed into an optical IQ modulator, which is driven by OFDM signals. Then polarization multiplexing is emulated by splitting the CO-OFDM signal from IQ modulator into two branches that are delayed with each other by 1 OFDM symbol (500 ns), and recombined with a polarization beam splitter (PBS). We emulate signals for two orthogonal LP_{11} modes by splitting the signal and delaying one branch by two OFDM symbols (1 μs). These two signals are mode converted into LP_{11} mode using LPFG-based MCs, combined and launched using free-space optics into a 4 meter TMF fibre. The signal is then inserted into the input port of the OADM module. All the amplification is achieved by SMF EDFAs (namely, the amplifiers are placed either before LP_{01}-to-LP_{11} conversion or after LP_{11}-to-LP_{01} conversion). Since the TMF is linear in the demonstration, TMF channel effect is insignificant in this work which is focused on the OADM impact.

In order to reduce required number of ADCs, optical 90° hybrids, and balanced receivers, we employ heterodyne configuration for the CO-OFDM detection. As depicted in Figure 5.9, the heterodyne receiver comprises two sharp roll-off band pass filters (BPFs) to filter the target optical band, four 3-dB power couplers to mix a local

oscillator (LO), four balanced photo diodes, and a real-time sampling scope. The challenge of the heterodyne detection is to ensure that the coherent detection can be performed without a need for excessive frequency guard band. For this purpose, sharp roll-off filters are employed to effectively reject the image interference from neighbouring bands, which otherwise will fold back and overlap with the target band if not sufficiently filtered. The frequency spacing between LO and the signal carrier is about 10 GHz, which allows enough gap to ensure the isolation of the image from other bands.

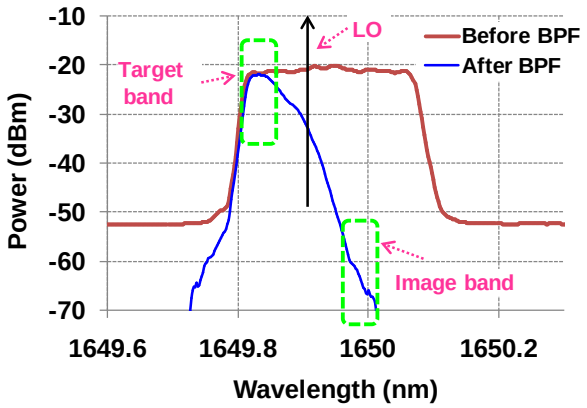

Figure 5.10. Received spectra for multi-band heterodyne detection. LO: Local oscillator.

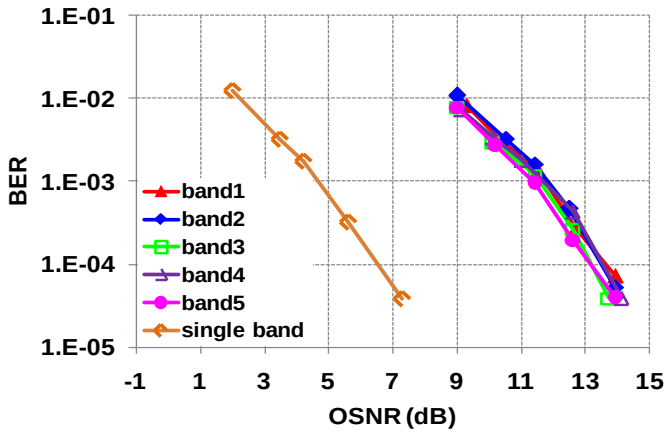

Figure 5.11. Measured BER as a function of OSNR for heterodyne single-band detection at 13.3 Gb/s and multi-band detection at 66.8 Gb/s.

To verify the effectiveness of the proposed heterodyne setup, we first conduct an experiment to measure the performance in a single polarization SMF configuration. We compare the performance of single band and multi bands (5 bands). The 5 bands are

placed continuously on the spectrum without frequency guard band as shown in Figure 5.10. The centre wavelength of BPF is carefully tuned so that it aligns with the signal carrier frequency of the target band. The LO and signal carrier is spaced at 10 GHz. From Figure 5.10 it can be seen that due to the sharp roll-off of the BPF, the power of neighbouring bands drop quickly from the edge of target band to image band. The rejection ratio of image band to target band is higher than 40 dB. As such, we expect there should be negligible penalty from the image band folding into the target band. Additionally, the measurements of the multi-band heterodyne detection performance are illustrated in Figure 5.11. If we compare the performance of single band detection (open yellow diamond curve) with multi-band detection, the difference of OSNR requirement (for instance, at BER level of $1x10^{-3}$) is about 7.2 dB, which agrees very well with the theoretical value of 7 dB corresponding to the increase of number of bands. This means that there is almost no implementation penalty for the proposed multi-band heterodyne detection. Moreover, it is worth noting that the performances of 5 bands are almost the same, which suggests both the image band and the neighbouring bands incur insignificant degradation to each band.

OFDM parameters used are as follows: OFDM symbol length of 2560 points; cyclic prefix of 452 points; 4 OFDM training symbols employed to represent alternate launch of 4 combinations of polarizations and modes, which is used for 4x4 channel matrix by means of intra-symbol averaging [79]; unique word length of 32 used at each end of OFDM symbol to seed phase estimation for data symbols [38]. The phase estimation of training symbols is done by using RF pilot subcarrier as explained in section IV. The data symbols use DFT-S signal, and the phase estimation is done using decision feedback seeded by unique words [38]. The three CO-OFDM channels each occupying 59.67 GHz bandwidth and carrying a net data rate of 318 Gb/s. All the BERs are calculated using 998,400 bits. Signal processing uses 4x4 MIMO OFDM procedure [33].

Figure 5.12 depicts the optical spectra of the transmitted superchannels and the MDM superchannels after OADM. The channel spacing is 100 GHz. From the spectra of the dropped channel and the through channel without add, it can be seen that the

centre channel have been effectively eliminated. The neighbour channel isolation is more than 25 dB determined from the spectrum at the drop port.

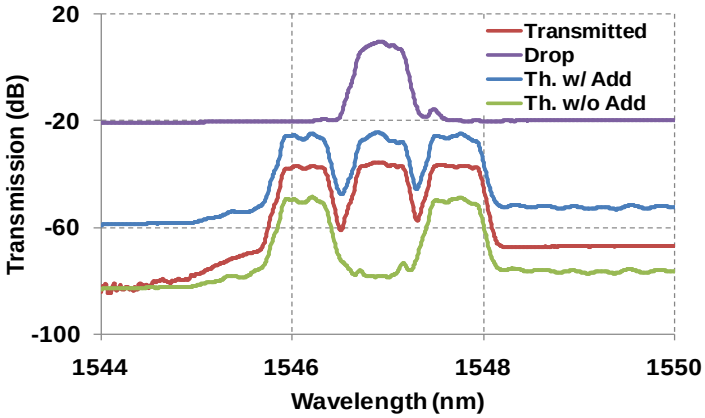

Figure 5.12. Measured spectra for transmitted signal, OADM through channels (w/ and w/o add channel), and the drop channel.

Figure 5.13 shows the BER of all the functionalities of the OADM. The OSNRs are measured for the entire channel at 318 Gb/s. It can be seen that the penalty at a 7% FEC limit (BER=$3.8\text{x}10^{-3}$) for add, drop and through ports are 2.6, 2.4, 0.7 dB, respectively. Figure 5.14 presents the performance of all the bands for add, drop, through channels measured at an OSNR of 22.8 dB. It can be seen all the bands are below 7% FEC threshold. The inset shows the constellation for drop channel at an OSNR of 22.8 dB. We attribute the relatively large penalty to the beating between LP_{01} and LP_{11} modes.

This system is limited to 4x4 MIMO and does not capture the LP_{01} mode due to the following two reasons. First, the free-space based mode couplers (shown as BS in Figure 5.9) seriously degrade the performance by inducing low modal extinction ratio and large mode-dependent loss. Second, due to the extreme large differential-mode-delay (DMD) between the LP_{01} and LP_{11} for our TMF, the transmission demonstration is not considered in this work. However, by using the 4x4 MIMO configuration, any coupling between LP_{01} and LP_{11} modes in the OADM will be detrimental to the performance. This explains relatively large penalty shown in OSNR sensitivity in Figure 5.13. However, low DMD FMF fibre can be used aided by 6x6 or 4x6 MIMO signal processing to compensate for this effect. Therefore we expect the OADM performance for 4x6 and 6x6 MIMO will be robust to inter mode coupling

between LP_{01} and LP_{11} mode.

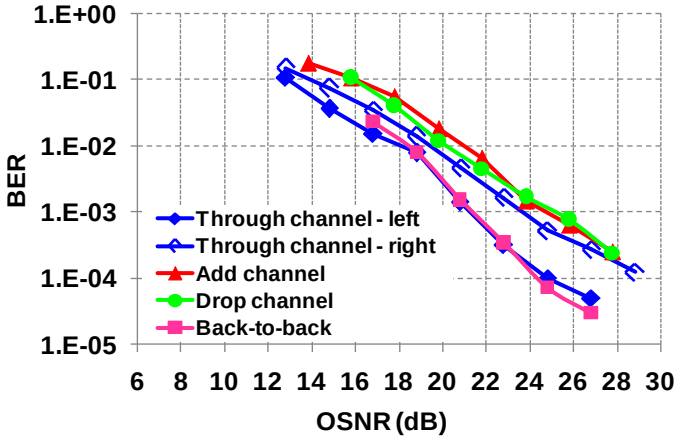

Figure 5.13. Measured BER-vs-OSNR for add, drop and through channels at 318 Gb/s. Inset shows constellation for the add port signals at OSNR of 22.8 dB.

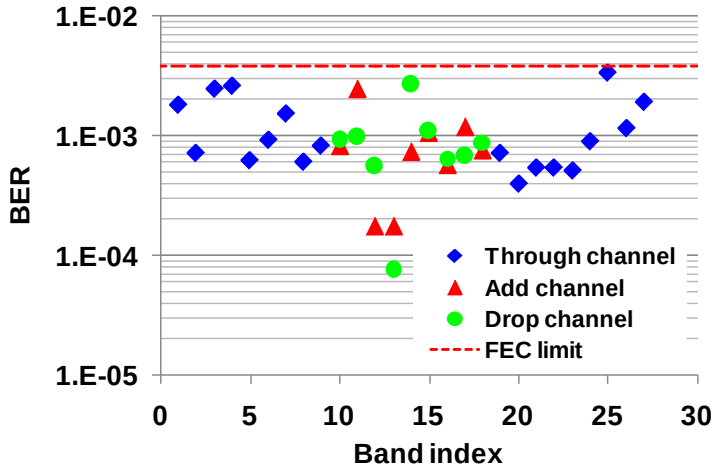

Figure 5.14. BER for all bands after OADM at an OSNR of 22.8 dB.

Our work also reveals tremendous challenges ahead in characterizing FMF based components. There are a few critical elements that need to be developed to fully characterize the FMF based components. For instance, pure higher-order mode sources, high extinction-ratio mode-multiplexers and de-multiplexers are essential to identify the inter-modal interference of the few-mode compatible components under test. The first-order estimate is that the mode extinction ratio for those characterization devices should be better than 20 dB.

5.3 Conclusions

In this chapter, we demonstrated three channel equalization methods for FMF-based CO-OFDM systems. The results show that the 4x6 MIMO receiver can improve the receiver sensitivity by 1.8 dB, 2.9 dB, and 4.9 dB for ZF, MMSE, and SIC respectively.

At last, we designed an OADM that supports two orthogonal LP_{11} modes of a FMF. We demonstrate add, drop and through functionalities for 3x318 Gb/s OFDM signals, and found that the OSNR penalties for add, drop and through ports are 2.6, 2.4, 0.7 dB, respectively. Additionally, a heterodyne coherent detection which supports multi-band signal with high spectral efficiency is proposed and investigated.

Chapter 6 Conclusion

6.1 Summary of the Work

In this thesis, we have conducted theoretical and experimental study on high spectral efficiency CO-OFDM systems. We first presented theoretical analysis on information capacity limits in the presence of fibre nonlinearity for CO-OFDM systems. We then showed two effective approaches for fibre nonlinearity mitigation. We also developed an algorithm for phase noise monitoring in high spectral efficiency CO-OFDM systems. At last, we designed and demonstrated high spectral efficiency CO-OFDM transmission using two-mode fibres.

6.1.1 Information Capacity Limits of CO-OFDM Systems

With the expansion of signal bandwidth and adoption of higher-order constellations, fibre nonlinearity becomes a critical impairment in optical transmission. Moreover, there is a common belief that due to their high peak-to-average power ratio (PAPR), CO-OFDM systems are more susceptible to fibre nonlinearity compare with single carrier systems. It is therefore necessary to study the information capacity limit of CO-OFDM systems in the presence of fibre nonlinearity. As a result, we presented theoretical study of information capacity limit for densely spaced CO-OFDM systems. The theoretical study includes derivation of closed-form expressions for transmission via both single mode fibre (SMF) and few-mode fibre (FMF). The theory has been further verified by numerical simulation and some preliminary experimental results.

We first derived closed-form analytical expressions of nonlinear system performance of densely spaced CO-OFDM systems via SMF transmission. The closed-form solutions include the results of the achievable Q factor, optimum launch power density, nonlinear threshold of launch power density, and information spectral efficiency limit. These analytical results clearly identify their dependence on system parameters including fibre dispersion, number of spans, dispersion compensation ratio,

and overall bandwidth. The closed-form solution is further substantiated by numerical simulations using distributed nonlinear Schrödinger equation.

We then showed some preliminary study on the information capacity of densely spaced CO-OFDM transmission via two-mode fibre (TMF). We have measured fibre nonlinear Kerr coefficient and presented discussions of system capacity for two-mode fibre. The system capacity approaches 3 times of that of single-mode fibre even though there is strong spatial overlapping between the modes in TMF.

6.1.2 Mitigation of Fibre Nonlinear Noise for CO-OFDM Systems

We have proposed two approaches of nonlinearity mitigation including DFT-spread (DFT-S) OFDM and mid-link digital phase conjugation.

First, we have shown the first experimental verification of nonlinear performance advantage of DFT-S OFDM systems over conventional OFDM systems. Densely spaced 8×55.1-Gb/s DFT-S OFDM channels are successfully received after 1120-km transmission with a spectral efficiency of 3.5 b/s/Hz. We adopt a novel approach of consecutive transmission of DFT-S OFDM and conventional OFDM enabling stable and repeatable measurements. It is shown that DFT-S OFDM has about 1 dB in Q factor and 1 dB in launch power improvement over conventional OFDM. Additionally, unique word (UW) aided phase estimation algorithm is proposed and demonstrated enabling extremely long OFDM symbol transmission.

Second, we have also demonstrated single-channel 40-Gb/s polarization-division multiplexed (PDM) CO-OFDM-16QAM transmission over 10,400-km ultra-large area fibre (ULAF) by mid-link digital phase conjugation, showing a power-tolerance improvement of 4 dB and a reach extension of over 50% for this high-level modulation format. Together with its high DSP efficiency, mid-link digital phase conjugation could be a promising candidate for future ultra-long-haul point-to-point transmission systems.

6.1.3 Phase Noise Monitoring for High Spectral Efficiency CO-OFDM Transmission

To achieve high spectral efficiency transmission, besides the nonlinearity

mitigation methods we discussed in Chapter 3, there are a few other techniques to monitor system performance. We presented closed-form expressions for differential phase-error variance. The phase noise is averaged over a finite time window, cancelling the effects of additive white noise. The method of laser linewidth characterization and monitoring is proposed in the presence of additive white noise applicable to both single-carrier and multi-carrier systems. With the proposed method, laser linewidth can be extracted via embedded signal processing. Therefore the monitoring can be done in-service without interruption of data transmission. The method is further substantiated by experiments in a 107-Gb/s coherent optical OFDM system with 960-km transmission over SSMF fibre. Additionally, a novel method of digitally adjusting laser linewidth is proposed and demonstrated which can be used to systematically study the laser phase noise impact.

6.1.4 Enabling Spectrum-Efficient Transmission by Using TMF Fibres

We demonstrated three channel equalization methods for FMF-based CO-OFDM systems. The results show that the 4x6 MIMO receiver can improve the receiver sensitivity by 1.8 dB, 2.9 dB, and 4.9 dB for zero-forcing (ZF), minimum mean square error (MMSE), and successive interference cancellation (SIC) respectively. We then designed an optical add/drop multiplexer (OADM) that supports two orthogonal LP_{11} modes of a FMF. We demonstrated add, drop and through functionalities for 3x318 Gb/s CO-OFDM signals, and found that the OSNR penalties for add, drop and through ports are 2.6, 2.4, 0.7 dB, respectively. Additionally, the heterodyne coherent detection which supports multi-band signal with high spectral efficiency is proposed and investigated.

Bibliography

[1] I.-T. G.694.1. *Spectral grids for WDM applications: DWDM frequency grid*. Available: http://www.itu.int/rec/T-REC-G.694.1/en

[2] I.-T. G.694.2. *WDM applications: CWDM wavelength grid*. Available: http://www.itu.int/rec/T-REC-G.694.2/en

[3] A. Li, X. Chen, G. J. Gao, and W. Shieh, "Transmission of 1-Tb/s Unique-word DFT-Spread OFDM Superchannel over 8,000-km SSMF," in *Asia Communications and Photonics Conference (ACP)*, 2011, pp. 830929-830936.

[4] S. Chandrasekhar, X. Liu, B. Zhu, and D. W. Peckham, "Transmission of a 1.2-Tb/s 24-carrier no-guard-interval coherent OFDM superchannel over 7200-km of ultra-large-area fiber," in *35th European Conference on Optical Communication (ECOC)*, 2009, p. PD2.6.

[5] D. Qian, M.-F. Huang, E. Ip, Y.-K. Huang, Y. Shao, J. Hu, and T. Wang, "101.7-Tb/s (370×294-Gb/s) PDM-128QAM-OFDM Transmission over 3×55-km SSMF using Pilot-based Phase Noise Mitigation," in *Optical Fiber Communication Conference (OFC)*, 2011, p. PDPB5.

[6] J. X. Cai, Y. Cai, C. Davidson, A. Lucero, H. Zhang, D. Foursa, O. Sinkin, W. Patterson, A. Pilipetskii, G. Mohs, and N. Bergano, "20 Tbit/s Capacity Transmission Over 6,860 km," in *Optical Fiber Communication Conference (OFC)*, 2011, p. PDPB4.

[7] W. Shieh, H. Bao, and Y. Tang, "Coherent optical OFDM: theory and design," *Optics Express*, vol. 16, pp. 841-859, Jan 21 2008.

[8] E. Yamada, A. Sano, H. Masuda, E. Yamazaki, T. Kobayashi, E. Yoshida, K. Yonenaga, Y. Miyamoto, K. Ishihara, Y. Takatori, T. Yamada, and H. Yamazaki, "1Tb/s (111Gb/s/ch x 10ch) No-Guard-Interval CO-OFDM Transmission over 2100 km DSF," *Joint Conference of the Opto-Electronics and Communications Conference and the Australian Conference on Optical Fibre Technology (OECC/ACOFT)* pp. 670-671, 2008.

[9] Y. R. Ma, Q. Yang, Y. Tang, S. M. Chen, and W. Shieh, "1-Tb/s single-channel coherent optical OFDM transmission over 600-km SSMF fiber with subwavelength bandwidth access," *Optics Express*, vol. 17, pp. 9421-9427, May 25 2009.

[10] G. Goldfarb, G. F. Li, and M. G. Taylor, "Orthogonal wavelength-division multiplexing using coherent detection," *Photonics Technology Letters*, vol. 19, pp. 2015-2017, Nov-Dec 2007.

[11] R. Dischler and F. Buchali, "Transmission of 1.2 Tb/s Continuous Waveband PDM-OFDM-FDM signal with Spectral Efficiency of 3.3 bit/s/Hz over 400 km of SSMF," *Conference on Optical Fiber Communication (OFC)*, p. PDPC2, 2009.

[12] H. Takahashi, A. Al Amin, S. L. Jansen, I. Morita, and H. Tanaka, "Highly Spectrally Efficient DWDM Transmission at 7.0 b/s/Hz Using 8 x 65.1-Gb/s

Coherent PDM-OFDM," *Journal of Lightwave Technology,* vol. 28, pp. 406-414, Feb 15 2010.

[13] A. J. Lowery, S. Wang, and M. Premaratne, "Calculation of power limit due to fiber nonlinearity in optical OFDM systems," *Optics Express,* vol. 15, pp. 13282-13287, Oct 1 2007.

[14] M. Nazarathy, J. Khurgin, R. Weidenfeld, Y. Meiman, P. Cho, R. Noe, I. Shpantzer, and V. Karagodsky, "Phased-array cancellation of nonlinear FWM in coherent OFDM dispersive multi-span links," *Optics Express,* vol. 16, pp. 15777-15810, Sep 29 2008.

[15] X. Liu, F. Buchali, and R. W. Tkach, "Improving the Nonlinear Tolerance of Polarization-Division-Multiplexed CO-OFDM in Long-Haul Fiber Transmission," *Journal of Lightwave Technology,* vol. 27, pp. 3632-3640, Aug 15 2009.

[16] M. Mayrock and H. Haunstein, "Monitoring of Linear and Nonlinear Signal Distortion in Coherent Optical OFDM Transmission," *Journal of Lightwave Technology,* vol. 27, pp. 3560-3566, Aug 15 2009.

[17] K. Inoue, "Phase-Mismatching Characteristic of 4-Wave-Mixing in Fiber Lines with Multistage Optical Amplifiers," *Optics Letters,* vol. 17, pp. 801-803, Jun 1 1992.

[18] P. P. Mitra and J. B. Stark, "Nonlinear limits to the information capacity of optical fibre communications," *Nature,* vol. 411, pp. 1027-1030, Jun 28 2001.

[19] X. Chen and W. Shieh, "Closed-form expressions for nonlinear transmission performance of densely spaced coherent optical OFDM systems," *Optics Express,* vol. 18, pp. 19039-19054, Aug 30 2010.

[20] W. Shieh and X. Chen, "Information Spectral Efficiency and Launch Power Density Limits Due to Fiber Nonlinearity for Coherent Optical OFDM Systems," *IEEE Photonics Journal,* vol. 3, pp. 158-173, Apr 2011.

[21] R. W. Tkach, A. R. Chraplyvy, F. Forghieri, A. H. Gnauck, and a. R. M. Derosier, "Four-photon mixing and high-speed WDM systems," *Optics Express* vol. 16, pp. 21944-21957 1995.

[22] C. E. Shannon, "A Mathematical Theory of Communication," *Bell System Technical Journal,* vol. 27, pp. 379-423, 1948.

[23] R. J. Essiambre, G. Kramer, P. J. Winzer, G. J. Foschini, and B. Goebel, "Capacity Limits of Optical Fiber Networks," *Journal of Lightwave Technology,* vol. 28, pp. 662-701, Feb 15 2010.

[24] X. Liu, S. Chandrasekhar, P. J. Winzer, S. Draving, J. Evangelista, N. Hoffman, B. Zhu, and D. W. Peckham, "Single Coherent Detection of a 606-Gb/s CO-OFDM Signal with 32-QAM Subcarrier Modulation Using 4x 80-Gsamples/s ADCs," in *36th European Conference and Exhibition on Optical Communication (ECOC),* 2010, p. PD2.6.

[25] X. Zhou, L. Nelson, P. Magill, R. Isaac, B. Zhu, D. W. Peckham, P. Borel, and K. Carlson, "8x450-Gb/s, 50-GHz-Spaced, PDM-32QAM transmission over 400km and one 50GHz-grid ROADM," in *Optical Fiber Communication Conference (OFC)* 2011, p. PDPB3.

[26] J. Sakaguchi, Y. Awaji, N. Wada, A. Kanno, T. Kawanishi, T. Hayashi, T. Taru, T. Kobayashi, and M. Watanabe, "109-Tb/s (7x97x172-Gb/s SDM/WDM/PDM) QPSK transmission through 16.8-km homogeneous multi-core fiber," in *Optical Fiber Communication Conference (OFC)*, 2011, p. PDPB6.

[27] B. Zhu, T. Taunay, M. Fishteyn, X. Liu, S. Chandrasekhar, M. Yan, J. Fini, E. Monberg, and a. F. Dimarcello, "Space-, wavelength-, polarization-division multiplexed transmission of 56-Tb/s over a 76.8-km seven-core fiber," in *Optical Fiber Communication Conference (OFC)*, 2011, p. PDPB.7.

[28] A. Li, A. Al Amin, X. Chen, and W. Shieh, "Reception of Mode and Polarization Multiplexed 107-Gb/s CO-OFDM Signal over a Two-Mode Fiber," in *Optical Fiber Communication Conference (OFC)*, 2011, p. PDPB8.

[29] R. Ryf, S. Randel, A. H. Gnauck, C. Bolle, R.-J. Essiambre, P. Winzer, D. W. Peckham, A. McCurdy, and R. Lingle, "Space-division multiplexing over 10 km of three-mode fiber using coherent 6 × 6 MIMO processing," in *Optical Fiber Communication Conference (OFC)*, 2011, p. PDPB10.

[30] X. Chen, A. Li, G. J. Gao, A. Al Amin, and W. Shieh, "Characterization of fiber nonlinearity and analysis of its impact on link capacity limit of two-mode fibers," *IEEE Photonics Journal*, vol. 4, pp. 455-460, Apr 2012.

[31] S. Randel, R. Ryf, A. Sierra, P. J. Winzer, A. H. Gnauck, C. A. Bolle, R. J. Essiambre, D. W. Peckham, A. McCurdy, and R. Lingle, "6x56-Gb/s mode-division multiplexed transmission over 33-km few-mode fiber enabled by 6x6 MIMO equalization," *Optics Express*, vol. 19, pp. 16697-16707, Aug 2011.

[32] E. Ip, N. Bai, Y.-K. Huang, E. Mateo, F. Yaman, S. Bickham, H.-Y. Tam, C. Lu, M.-J. Li, S. Ten, A. P. T. Lau, V. Tse, G.-D. Peng, C. Montero, X. Prieto, and G. Li, "88x3x112-Gb/s WDM Transmission over 50-km of Three-Mode Fiber with Inline Multimode Fiber Amplifier," in *37th European Conference and Exhibition on Optical Communication (ECOC)*, 2011, p. Th.13.C.2.

[33] A. Al Amin, A. Li, S. M. Chen, X. Chen, G. J. Gao, and W. Shieh, "Dual-LP11 mode 4x4 MIMO-OFDM transmission over a two-mode fiber," *Optics Express*, vol. 19, pp. 16672-16679, Aug 15 2011.

[34] G. Bosco, P. Poggiolini, A. Carena, V. Curri, and F. Forghieri, "Analytical results on channel capacity in uncompensated optical links with coherent detection," *Optics Express*, vol. 19, pp. B440-B451, 2011.

[35] S. L. Jansen, I. Morita, T. C. W. Schenk, and H. Tanaka, "121.9-Gb/s PDM-OFDM Transmission With 2-b/s/Hz Spectral Efficiency Over 1000 km of SSMF," *Journal of Lightwave Technology*, vol. 27, pp. 177-188, Jan-Feb 2009.

[36] X. Liu, S. Chandrasekhar, B. Y. Zhu, P. J. Winzer, A. H. Gnauck, and D. W. Peckham, "448-Gb/s Reduced-Guard-Interval CO-OFDM Transmission Over 2000 km of Ultra-Large-Area Fiber and Five 80-GHz-Grid ROADMs," *Journal of Lightwave Technology*, vol. 29, pp. 483-490, Feb 2011.

[37] Y. Tang, W. Shieh, and B. S. Krongold, "DFT-Spread OFDM for Fiber Nonlinearity Mitigation," *Photonics Technology Letters*, vol. 22, pp. 1250-1252, Aug 15 2010.

[38] X. Chen, A. Li, G. J. Gao, and W. Shieh, "Experimental demonstration of improved fiber nonlinearity tolerance for unique-word DFT-spread OFDM systems," *Optics Express,* vol. 19, pp. 26198-26207, Dec 19 2011.

[39] D. Falconer, S. L. Ariyavisitakul, A. Benyamin-Seeyar, and B. Eidson, "Frequency domain equalization for single-carrier broadband wireless systems," *IEEE Communications Magazine,* vol. 40, pp. 58-66, 2002.

[40] M. Huemer, H. Witschnig, and J. Hausner, "Unique word based phase tracking algorithms for SC/FDE-systems," in *Global Telecommunications Conference (GLOBECOM)*, 2003, pp. 70-74 Vol.1.

[41] L. Deneire, B. Gyselinckx, and M. Engels, "Training sequence vs. cyclic prefix a new look on single carrier communication," in *Global Telecommunications Conference (GLOBECOM)*, 2000, pp. 1056-1060 vol.2.

[42] D. Chu, "Polyphase codes with good periodic correlation properties," *IEEE Transactions on Information Theory,* vol. 18, pp. 531-532, 1972.

[43] W. Shieh, "Maximum-likelihood phase and channel estimation for coherent optical OFDM," *IEEE Photonics Technology Letters,* vol. 20, pp. 605-607, Mar-Apr 2008.

[44] M. E. Mousa-Pasandi and D. V. Plant, "Zero-overhead phase noise compensation via decision-directed phase equalizer for coherent optical OFDM," *Optics Express,* vol. 18, pp. 20651-20660, Sep 27 2010.

[45] D. S. Ly-Gagnon, K. Katoh, and K. Kikuchi, "Unrepeated 210-km transmission with coherent detection and digital signal processing of 20-Gb/s QPSK signal," in *Optical Fiber Communication Conference (OFC)*, 2005, p. OTuL4.

[46] S. Zhang, P. Y. Kam, C. Yu, and J. Chen, "Laser linewidth tolerance of decision-aided maximum likelihood phase estimation in coherent optical M-ary PSK and QAM systems," *Photonics Technology Letters,* vol. 21, pp. 1075-1077, 2009.

[47] H. G. Myung, L. Junsung, and D. J. Goodman, "Peak-to-average power ratio of single carrier FDMA signals with pulse shaping," in *IEEE 17th International Symposium on Personal, Indoor and Mobile Radio Communications*, 2006, pp. 1-5.

[48] W. Shieh, "OFDM for Flexible High-Speed Optical Networks," *Journal of Lightwave Technology,* vol. 29, pp. 1560-1577, May 15 2011.

[49] E. Ip and J. M. Kahn, "Compensation of Dispersion and Nonlinear Impairments Using Digital Backpropagation," *Journal of Lightwave Technology,* vol. 26, pp. 3416-3425, 2008.

[50] S. L. Jansen, D. van den Borne, B. Spinnler, S. Calabro, H. Suche, P. M. Krummrich, W. Sohler, G. D. Khoe, and H. de Waardt, "Optical phase conjugation for ultra long-haul phase-shift-keyed transmission," *Journal of Lightwave Technology,* vol. 24, pp. 54-64, 2006.

[51] A. Chowdhury, G. Raybon, R. J. Essiambre, and C. R. Doerr, "WDM CSRZ 40 Gbit/s pseudo-linear transmission over 4800 km using optical phase conjugation," *Electronics Letters,* vol. 41, pp. 151-152, Feb 3 2005.

[52] E. Mateo, X. Zhou, and G. Li, "Electronic phase conjugation for nonlinearity

compensation in fiber communication systems," in *Optical Fiber Communication Conference (OFC)*, 2011, p. JWA25.

[53] A. Chowdhury, G. Raybon, R. J. Essiambre, J. H. Sinsky, A. Adamiecki, J. Leuthold, C. R. Doerr, and S. Chandrasekhar, "Compensation of intrachannel nonlinearities in 40-Gb/s pseudolinear systems using optical-phase conjugation," *Journal of Lightwave Technology*, vol. 23, pp. 172-177, Jan 2005.

[54] X. Chen, X. Liu, S. Chandrasekhar, B. Zhu, and R. Tkach, "Experimental Demonstration of Fiber Nonlinearity Mitigation Using Digital Phase Conjugation," in *Optical Fiber Communication Conference (OFC)*, 2012, p. OTh3C.1.

[55] P. Poggiolini, A. Carena, V. Curri, and F. Forghieri, "Evaluation of the computational effort for chromatic dispersion compensation in coherent optical PM-OFDM and PM-QAM systems," *Optics Express*, vol. 17, pp. 1385-1403, Feb 2 2009.

[56] X. Liu, S. Chandrasekhar, P. J. Winzer, B. Zhu, D. W. Peckham, S. Draving, J. Evangelista, N. Hoffman, C. J. Youn, Y. H. Kwon, and E. S. Nam, "3x 485-Gb/s WDM transmission over 4800 km of ULAF and 12x 100-GHz WSSs using CO-OFDM and single coherent detection with 80-GS/s ADCs," in *Optical Fiber Communication Conference (OFC)*, 2011, p. JThA37.

[57] Y. Miyata, K. Sugihara, W. Matsumoto, K. Onohara, T. Sugihara, K. Kubo, H. Yoshida, and T. Mizuochi, "A triple-concatenated FEC using soft-decision decoding for 100 Gb/s optical transmission," *Conference on Optical Fiber Communication (OFC)*, p. OThL3, 2010.

[58] K. Kikuchi, "Effect of 1/f type FM noise on semiconductor-laser linewidth residual in high-power limit," *Journal of Quantum Electronics*, vol. 25, pp. 684-688, 1989.

[59] X. W. Yi, W. Shieh, and Y. R. Ma, "Phase noise effects on high spectral efficiency coherent optical OFDM transmission," *Journal of Lightwave Technology*, vol. 26, pp. 1309-1316, May-Jun 2008.

[60] W. Shieh, R. S. Tucker, W. Chen, X. W. Yi, and G. Pendock, "Optical performance monitoring in coherent optical OFDM systems," *Optics Express*, vol. 15, pp. 350-356, Jan 22 2007.

[61] F. N. Hauske, M. Kuschnerov, B. Spinnler, and B. Lankl, "Optical Performance Monitoring in Digital Coherent Receivers," *Journal of Lightwave Technology*, vol. 27, pp. 3623-3631, 2009.

[62] T. S. R. Shen, A. P. T. Lau, and C. Yu, "Simultaneous and independent multi-parameter monitoring with fault localization for DSP-based coherent communication systems," *Optics Express*, vol. 18, pp. 23608-23619, 2010.

[63] X. Chen, A. Al Amin, and W. Shieh, "Characterization and Monitoring of Laser Linewidths in Coherent Optical OFDM Systems," in *Optical Fiber Communication Conference (OFC)*, 2011, p. OWN4.

[64] X. Chen, A. Al Amin, and W. Shieh, "Characterization and Monitoring of Laser Linewidths in Coherent Systems," *Journal of Lightwave Technology*, vol. 29, pp. 2533-2537, 2011.

[65] K.-P. Ho, *Phase-modulated Optical Communication Systems*: Springer, 2005.
[66] D. S. Ly-Gagnon, S. Tsukamoto, K. Katoh, and K. Kikuchi, "Coherent detection of optical quadrature phase-shift keying signals with carrier phase estimation," *Journal of Lightwave Technology,* vol. 24, pp. 12-21, 2006.
[67] T. Duthel, G. Clarici, C. R. S. Fludger, J. C. Geyer, C. Schulien, and S. Wiese, "Laser Linewidth Estimation by Means of Coherent Detection," *Photonics Technology Letters,* vol. 21, pp. 1568-1570, 2009.
[68] K. Kikuchi and K. Igarashi, "Characterization of semiconductor-laser phase noise with digital coherent receivers," in *Optical Fiber Communication Conference (OFC)*, 2011, p. OML3.
[69] Y. Kokubun and M. Koshiba, "Novel multi-core fibers for mode division multiplexing: proposal and design principle," *IEICE Electronics Express,* vol. 6, p. 7, 2009.
[70] N. Hanzawa, K. Saitoh, T. Sakamoto, T. Matsui, S. Tomita, M. Koshiba, and A. Optical Society of, "Demonstration of mode-division multiplexing transmission over 10 km two-mode fiber with mode coupler," in *Optical Fiber Communication Conference (OFC)*, 2011, p. OWA4.
[71] M. Salsi, C. Koebele, D. Sperti, P. Tran, P. Brindel, H. Mardoyan, S. Bigo, A. Boutin, F. Verluise, P. Sillard, M. Bigot-Astruc, L. Provost, F. Cerou, and G. Charlet, "Transmission at 2x100Gb/s, over Two Modes of 40km-long Prototype Few-Mode Fiber, using LCOS based Mode Multiplexer and Demultiplexer," in *Optical Fiber Communication Conference (OFC)*, 2011, p. PDPB9.
[72] S. Randel, A. Sierra, S. Mumtaz, A. Tulino, R. Ryf, P. J. Winzer, C. Schmidt, and R. Essiambre, "Adaptive MIMO signal processing for mode-division multiplexing," in *Optical Fiber Communication Conference (OFC)*, 2012, p. OW3D.5.
[73] J. M. Kahn, H. Keang-Po, and M. B. Shemirani, "Mode coupling effects in multi-mode fibers," in *Optical Fiber Communication Conference (OFC)*, 2012, p. OW3D.3.
[74] R. Ryf, M. A. Mestre, A. Gnauck, S. Randel, C. Schmidt, R. Essiambre, P. Winzer, R. Delbue, P. Pupalaikis, A. Sureka, Y. Sun, X. Jiang, D. Peckham, A. H. McCurdy, and R. Lingle, "Low-Loss Mode Coupler for Mode-Multiplexed transmission in Few-Mode Fiber," in *Optical Fiber Communication Conference (OFC)*, 2012, p. PDP5B.5.
[75] C. Koebele, M. Salsi, D. Sperti, P. Tran, P. Brindel, H. Mardoyan, S. Bigo, A. Boutin, P. Sillard, F. Cerou, and G. Charlet, "Two-mode transmission with digital inter-modal cross-talk mitigation," in *37th European Conference and Exhibition on Optical Communication (ECOC)*, 2011, p. Tu.5.B.4.
[76] X. Chen, J. Ye, Y. Xiao, A. Li, J. He, Q. Hu, and W. Shieh, "Equalization of Two-mode Fiber Based MIMO Signals with Larger Receiver Sets," in *38th European Conference and Exhibition on Optical Communication (ECOC)*, 2012, p. Th.2.D.2.
[77] D. Gesbert, M. Shafi, D. S. Shiu, P. J. Smith, and A. Naguib, "From theory to practice: An overview of MIMO space-time coded wireless systems," *Journal*

on Selected Areas in Communications, vol. 21, pp. 281-302, Apr 2003.

[78] P. W. Wolniansky, G. J. Foschini, G. D. Golden, R. A. Valenzuela, Ieee, and Ieee, "V-BLAST: An architecture for realizing very high data rates over the rich-scattering wireless channel," in *1998 Ursi Symposium on Signals, Systems, and Electr Onics*, 1998, pp. 295-300.

[79] X. Liu and F. Buchali, "Intra-symbol frequency-domain averaging based channel estimation for coherent optical OFDM," *Optics Express,* vol. 16, pp. 21944-21957, Dec 2008.

[80] S. L. Jansen, I. Morita, N. Takeda, and H. Tanaka, "20-Gb/s OFDM Transmission over 4,160-km SSMF Enabled by RF-Pilot Tone Phase Noise Compensation," in *Optical Fiber Communication Conference (OFC)*, 2007, p. PDP15.

[81] R. Ryf, A. Sierra, R.-J. Essiambre, S. Randel, A. Gnauck, C. A. Bolle, M. Esmaeelpour, P. J. Winzer, R. Delbue, P. Pupalaikis, A. Sureka, D. Peckham, A. McCurdy, and R. Lingle, "Mode-Equalized Distributed Raman Amplification in 137-km Few-Mode Fiber," in *37th European Conference and Exhibition on Optical Communication (ECOC)*, 2011, p. Th.13.K.5.

[82] N. Bai, E. Ip, T. Wang, and G. F. Li, "Multimode fiber amplifier with tunable modal gain using a reconfigurable multimode pump," *Optics Express,* vol. 19, pp. 16601-16611, Aug 2011.

[83] X. Chen, A. Li, J. Ye, A. Al Amin, and W. Shieh, "Reception of Dual-LP11-Mode CO-OFDM Signals through Few-mode Compatible Optical Add/Drop Multiplexer," in *Optical Fiber Communication Conference (OFC)*, 2012, p. PDP5B.4.

[84] X. Chen, A. Li, J. Ye, A. Al Amin, and W. Shieh, "Reception of mode-division multiplexed superchannel via few-mode compatible optical add/drop multiplexer," *Optics Express,* vol. 20, pp. 14302-14307, 2012.

[85] Szapiel, "Method of assembling a multiplexer/demultiplexer apparatus to account for manufacturing variations in the thin-film optical filters," US Patent 7,072,540, 2006.

[86] Y. K. Chen, C. J. Hu, C. C. Lee, K. M. Feng, M. K. Lu, C. H. Chang, Y. K. Tu, and S. L. Tzeng, "Low-crosstalk and compact optical add-drop multiplexer using a multiport circulator and fiber Bragg gratings," *Photonics Technology Letters,* vol. 12, pp. 1394-1396, 2000.

[87] K. A. McGreer, "Arrayed waveguide gratings for wavelength routing," *IEEE Communications Magazine,* vol. 36, pp. 62-68, 1998.

[88] M. A. F. Roelens, S. Frisken, J. A. Bolger, D. Abakoumov, G. Baxter, S. Poole, and B. J. Eggleton, "Dispersion Trimming in a Reconfigurable Wavelength Selective Switch," *Journal of Lightwave Technology,* vol. 26, pp. 73-78, 2008.

[89] S. Tibuleac and M. Filer, "Transmission Impairments in DWDM Networks With Reconfigurable Optical Add-Drop Multiplexers," *Journal of Lightwave Technology,* vol. 28, pp. 557-598, 2010.